

University of Nottingham
UK | CHINA | MALAYSIA

Faculty of Engineering

Chemical and Environmental Engineering Department

On Bubble Rise Dynamics in a Continuum and Pairwise Interaction: An Experimental and Numerical Study

Mustapha Abbas Ethaib Al-Behadili (B.Sc., M.Sc.)

Thesis submitted to the University of Nottingham for the degree of

Doctor of Philosophy

July 2017

Abstract

The wide range of applications of bubbly flows in the industry makes its accurate modelling strongly demanded. The modelling of bubbly flow, however, is not straightforward because it consists of multi-scale structures in both time and space. Furthermore, the experimental verifications of the theoretical and the Direct Numerical Simulations, DNS, available are noticeably scarce especially for bubbles at high Reynolds numbers. Hence, this research aims to make its contribution to addressing the basic roots that make the modelling process difficult. These roots are represented, but not limited, by the bubble dynamics and bubble-bubble interaction.

Tracking of single and dual air bubbles in quiescent water is experimentally carried out using a high speed camera. For the numerical simulations, using ANSYS-FLUENT software with the VOF model, a structured adaptive mesh technique was developed here that is used to achieve a desirable level of refinement of the mesh around the rising bubbles.

It has been found that there is a relationship between the lateral migration of an ellipsoidal bubble and the shape oscillation. This relationship, however, has not been observed for the numerical approach. It also overestimated the experimental findings of bubble kinetics and shape oscillation by 30%.

Interestingly, this research contributes to awakening the small details in the underlying physics of the interaction between a pair of rising bubbles. It has been

found that a slight deviation in the size of a trailing bubble plays an important role in the state of the trailing bubble whether it approaches the leading bubble or separates from at large separation distances. This is considered due to the greater rise velocity that a smaller bubble has in the ellipsoidal regime compared to the larger bubble. Furthermore, when the separation distance between the rising bubbles is decreased, the appreciable acceleration that the trailing bubble owns has led it to approach the leading bubble and coalesce with it. This behaviour is supported by experiments and by the good agreement that the numerical approach showed. An empirical model that predicts the coalescence rate based on the deviation in the size ratio is presented. Finally, the spatial boundaries over which the coalescence of bubble pairs might occur has been numerically and experimentally presented.

Acknowledgements

I feel that the words alone are not enough to show the great gratitude and praise that I owe for the unlimited support of my supervisors Dr Buddhika N. Hewakandamby, Dr David M. Hargreaves and Prof. Barry J. Azzopardi. Throughout the whole period of the study, their continuous help and guidance were invaluable without which this research would not have come to light.

I feel very grateful for the Higher Committee for Education Development in Iraq (HCED) for funding me over the course of my study.

My thanks also go to the technician staff in L3 and L4, Phil, Paul, Reg, Alex, Karl and Mel, who are the hidden army that is behind the success in any experimental research.

I would also like to express my thanks and love to my great friends and colleagues Saad Raoof, Wisam Alani, Muayad Hasan, Wathiq Al-Hachami, Ramzi Al-Agele, Kamal Al-Hamadani, Hayder Mohammed, Rajab Omar, Yousuf AlAufi, Shara Mohammed, Abubakr Ibrahim, Escrig Josep, Vasques Joao, Ebiundu Komonibo and Katerina.

The special thanks should go for my lovely family Zahraa, Hasanain, Yasameen and Aymen, who lately jumped to our world during the writing period, without whom the life would be difficult in Nottingham. I acknowledge the overwhelmed love and support that they have given to me. I am also grateful for my Mum,

brothers and sisters who have never stopped wishing me the best in my study and life through their support and prayers.

Affirmation

With the exception of the following publication, this work presented in this Thesis has not been published elsewhere:

Conference Paper: M. Al-Behadili, D. Hargreaves, B. Hewakandamby, and B. Azzopardi. Numerical investigation of dual bubble system. *Proceedings of* 9^{th} *International Conference on Multiphase Flow* (ICMF), Firenze-Italy, 2016.

Contents

Contents v

List of Figures xi

List of Tables xix

Nomenclature xxi

1 INTRODUCTION 1

1.1 Context 1

1.2 Aims and objectives 4

1.3 Thesis outline 5

2 LITERATURE REVIEW 7

2.1 Bubble hydrodynamics 7

2.1.1 Dimensionless numbers 7

2.1.2 Forces acting on a rising bubble 10

2.2 Bubble dynamics 16

2.2.1 Path instabilities 16

2.2.2 Shape oscillation 20

2.3 Bubble-bubble interaction 23

2.4 Coalescence of bubbles 27

2.5 Summary 29

3 NUMERICAL AND EXPERIMENTAL METHODOLOGY 31

3.1 Introduction 31

3.2 Numerical Methodology 31

3.2.1 Governing equations 32

3.2.2 Adaptive mesh technique 34

3.2.2.1 Numerical description 35

3.2.3 Error and uncertainty 37

3.2.3.1 Spatial discretisation error 38

3.2.3.2 Temporal discretisation error 42

3.2.3.3 Iteration convergence error 43

3.2.4 Numerical testing and verification 45

3.2.4.1 Initial and boundary conditions 45

3.2.4.2 Bubbles rising side by side 46

3.2.4.3 Bubbles rising with vertical and horizontal offsets 52

3.3 Experimental setup and procedure 55

3.4 Image processing and analysing procedures 58

3.4.1 Camera calibration 59

3.4.2 Image and data processing system 63

3.4.2.1 Image acquisition 63

3.4.2.2 Image analysis from experiments 64

3.4.2.3 Parameters from CFD 66

3.5 Summary 67

4 OBSERVATIONS OF SINGLE BUBBLE DYNAMICS 69

4.1 Introduction 69

4.2 Experimental setup 69

4.3 Experimental path instability and shape oscillation 72

4.3.1 Path instability 72

4.3.2 Shape oscillation 77

4.4 Comparison of the experimental and the numerical observations . 82

4.5 FFT analysis of the bubble dynamics 88

4.6 Summary 91

5 INTERACTION OF BUBBLE PAIRS AT LARGE SEPARATION DISTANCES 93

5.1 Introduction 93

5.2 Experimental materials and procedure 93

5.3 Hydrodynamic interaction of rising of bubbles 96

5.3.1 A pair of bubbles rising with offset 97

5.3.2 Bubbles rising side by side 111

5.4 Numerical investigation of bubble-bubble interaction 117

5.5 Summary 125

6 INTERACTION OF BUBBLE PAIRS AT SMALL SEPARATION DISTANCES **127**

6.1 Introduction 127

6.2 Experimental procedure 128

6.3 Factors affecting coalescence of bubbles 129

6.3.1 Effect of separation distance 130

6.3.2 Effect of relative bubble size 133

6.4 Numerical observations 144

6.5 Characterisation of pairwise coalescence 151

6.5.1 Background 151

6.5.2 Model construction 152

6.6 Summary 157

7 CONCLUSIONS AND RECOMMENDATIONS **159**

7.1 Conclusions 159

7.2 Recommendations 163

BIBLIOGRAPHY **167**

Appendices **181**

A UNCERTAINTY ANALYSES **181**

B CFD MODELLING PROCESS **183**

B.1 Grid generation 184

B.1.0.1 Structured grid 184

B.1.1 Unstructured grid 185

B.2 Finite volume method 186

B.3 Temporal discretisation 187

B.4 Vortex identification 188

C UDF SOURCE CODE **191**

List of Figures

2.1 Shape regimes map for motion of bubbles and drops in liquids (Clift et al., 1978) 11

2.2 Flow fields generated for two bubbles rising in line (Kusuno and Sanada, 2015b) 24

2.3 Coalescence of two nearly spherical bubbles rising side by side (Duineveld, 1998). 28

3.1 Dynamic adaptive mesh region around the bubbles. 38

3.2 Time evolution of the adaptively marked grid. 39

3.3 The results of average rise velocities computed using the adaptive grid region with each cell spacing 0.093 mm, 0.125 mm and 0.156 mm along with the extrapolated range of rise velocity. . . . 42

3.4 The results of average rise velocities predicted by time step size 1×10^{-5} s, 2.5×10^{-5} s and 5×10^{-5} s along with the extrapolated range of rise velocity. 43

3.5 Residual example of single air bubble rise of 2 mm radius in water. The residual was recorded while the bubble travelled mid way through the height of the domain. 44

3.6 An example of the initial setup of a simulation run which shows the free surface boundary condition above the water and two spherical bubbles rising having an offset. 47

3.7 Time evolution of coalescence predicted by our adaptive grid methodology. 48

3.8 Encounter of bubbles at contour lines α_l=0.1 and 0.5. 49

3.9 Comparison between fixed mesh (left column) and 5 levels of dynamic adaptive mesh (middle and right columns). 50

3.10 General topology of coalesced bubble captured at (a) 4 levels (b) 5 levels of adaptive mesh refinement. 51

3.11 Total number of cells used for simulating two rising bubbles and for 5 adaptive mesh refinement levels. 52

3.12 Predicted coalescence and the marked region tracking the air phase. 54

3.13 Schematic of the experimental apparatus. 56

3.14 Photograph of the experimental setup. 57

3.15 Schematic top view of the test section. 58

3.16 Principle camera parameters (a) focal length (b) skew coefficient (c) principal point (Mathworks, 2014). 60

3.17 Extraction of corners from calibration image. 61

3.18 Reprojection of errors due lens distortion. 62

3.19 Applying camera parameters to undistort images (a) distorted image (b) undistorted image. 63

3.20 Detection and binerisation two views of single bubble (a) raw image, (b) global background, (c) background subtraction (d) binarised image. 65

3.21 Parameters that are measured as a result to an ellipse fit inside a bubble. 66

3.22 Bubble data exported from Ansys-Fluent showing an air bubble represented by a cloud of points. 67

4.1 Schematic diagram of the test section (a) top view (b) coordinate system and the bubble principal axes of the two planes. 71

4.2 Superimposition of bubbles (Δt= 20) ms for the mirror (left) and the direct (right) images. 73

4.3 Lateral positions of single bubble (a) r=1.605 mm (b) r=2.025 mm (c) r=2.57 mm 75

4.4 Three dimensional behaviour of a single bubble of r=1.605 mm (a) top view of the bubble with its lateral positions (b) 3D bubble behaviour showing the a helical motion near the top surface of the water. 76

4.5 Experimental bubble-centroids and velocity for the 1.605 mm bubble (a) transverse migration in x and y positions (b) the three components of bubble velocity u, v and w. 78

4.6 Principal axes of bubble with time for an experimental run of r=1.605 mm. a_1 bubble major length captured directly from the camera, b_1 minor axis measured from the camera, a_2 bubble major axis measured from the mirror, b_2 minor axis measured from the mirror. 79

4.7 Experimental time evolution of bubble major axes ratio for r=1.605 mm. 80

4.8 Comparison for the experimental results of the 1.605 bubble against the 2.57 mm bubble (a) position of centroids (b) tilt angle (c) aspect ratio. 81

4.9 Trajectories predicted by the numerical simulation for the 1.605 mm bubble (a) trajectories in 2D planes (b) 3D trajectory of the bubble. 84

4.10 Comparison between the experimental and the numerical methods for r=1.605 mm in the x-plane (a) lateral positions (b) orientation of the bubble along the path (c) aspect ratio of the major and the minor axes. 86

4.11 Comparison for the results of the VOF method with the experiments in the y-plane (a) positions of centroid (b) tilt angle (c) aspect ratio. 87

4.12 Comparison of the FFT analysis for the experiments with the VOF method. 90

5.1 Relative configurations and coordinate system of bubble pair rising (a) bubbles rising at an offset, (b) bubbles rising side by side. . . 95

5.2 Detection and binarisation of pair of bubbles (a) raw image, (b) global background, (c) binarised image. 97

5.3 Typical motion of a pair of bubbles with offset axes. 98

5.4 Bubble-bubble interaction effects on the vertical rise velocities of pair of bubbles (s=6.6, r_1=1.96 mm, r_2=1.92 mm). 99

5.5 The rise velocities of a pair of bubbles at large separation distance (s=8, r_1=1.94 mm, r_2=1.97 mm). 100

5.6 Pairs of bubbles rising having offset in their axes at different centre to centre distances. Bubble pairs do not coalesce while they rise. . 101

5.7 The Rise velocity of air bubbles in water (Clift et al., 1978). . . . 103

5.8 The effect of the bubbles size deviation on the interaction of bubbles. 104

5.9 Three dimensional trajectory and bubble velocity for a pair of bubble: (a) separating (b) approaching. 105

5.10 A sketch showing the 3D centre to centre equilibrium distance, l. . 108

5.11 The 3D centre to centre equilibrium distance, l, between the bubbles (a) the trailing bubble is either equal or larger than the leading bubble, (b) the trailing bubble is smaller than the leading bubble. 109

5.12 Hydrodynamic interaction effect on bubbles trajectories. 112

5.13 Scattering degree of bubble-bubble interaction. 113

5.14 Pairs of air bubbles rising side by side. 114

5.15 The final separation distance related to the initial relative size of bubbles rising side by side, the red symbols represent the data points in Table 5.1. 116

5.16 Distribution of velocity around two rising bubbles at their mid way through the computational domain (a) contours of velocity magnitude (b) velocity vectors. 118

5.17 Distribution of vorticity for a pair of equally sized bubbles bubbles rising at s =4.5 ($\triangle t$= 0.08 s) viewed using (a) 2D plane (b) Q-criterion. 120

5.18 Instantaneous behaviour of the 3D centre to centre equilibrium distance, l, between the bubbles from the simulations. 122

5.19 Comparison of the numerical simulations for differently sized bubble pairs to the equally sized pair of bubbles (a) equally sized bubbles ($\triangle t$= 0.12 s)(b) trailing bubble, right bubble, smaller than the leading bubble (left bubble) by 5 % (c) trailing bubble (right bubble) smaller by 10 %. 124

6.1 Relative configurations and coordinate system of bubble pair rising (a) bubbles rising at an offset, (b) bubbles rising side by side. . . 129

6.2 Coalescence probability from set of the three nozzles used in this study, the error bars represent the standard error which relates the standard deviation to the sample size. 131

6.3 Sketch showing the expected scenarios that a trailing bubble could experience when it travels nearby the wake of a leading bubble. . 132

6.4 Effect of relative bubble size on the coalescence of bubbles when the trailing bubble is smaller than the leading bubble, there is a higher probability of coalescence. 134

6.5 Relative motion of two coalescing bubbles, the trailing bubble is smaller than the leading bubble by 5 % (a) superimposition of frames in xz and yz planes showing the approach of the trailing bubble, (b) 3D trajectory of both bubbles, (c) rise velocity of both bubbles. 136

6.6 Initial and final interaction between the bubbles represented by the initial relative angle, θ_i, and the coalescence (equilibrium) angle, θ_c. 138

6.7 Time evolution of two different sized bubbles. 140

6.8 The nondimensionalised time delay before the coalescence of a pair of bubbles related to the initial bubble size ratio. 143

6.9 Bubbles configuration and adaptive mesh region. 146

6.10 Tested three cases of deviation in rising bubble sizes (a) equal-sized bubbles, (b) the trailing bubble is smaller by 5 % (c) the trailing bubble is smaller by 10 %. 147

6.11 A map for the spatial boundaries of coalescence from the numerical simulations and the experiments. This map also shows the disparity between both results based on the change in the trailing bubble size. 150

6.12 Schematic of the horizontal separation distance between the bubbles. 152

6.13 Comparison between the suggested model and the experimental data. 155

6.14 Dimensionless rate of coalescence based on Eq. (6.4) and the model of Davies (1984). 156

7.1 An example showing bubbles rising side by side modelled using Species model in Ansys-Fluent. 166

B.1 Structured grid for flow over a cylinder (Versteeg and Malalasekera, 2007). 185

B.2 Mixed cells with unstructured grid (Versteeg and Malalasekera, 2007). 186

List of Tables

2.1 Summary of previous work on the onset of path instability and the observed regimes (de Vries, 2001). 18

3.1 Grid size of the highest level of refinement of the adaptive mesh and the number of the cells in the computational domain. 41

4.1 Summary of the motion types for the studied bubble sizes. 74

4.2 Summary of the average results for the bubble sizes studied here. 89

5.1 Experimental parameters of the investigated cases in Figure 5.14. 115

5.2 Summary of the simulation parameters for the investigated cases. 122

6.1 Summary of coalescence parameters of additional experiments to test the effect of further deviation in bubble size ratio on the coalescence. 141

6.2 Summary of the important parameters of experimental results obtained. 142

6.3 Summary of the simulation parameters for the investigated cases. 145

6.4 Comparison of the parameters obtained from the numerical simulations with the experiments. 148

Nomenclature

List of Abbreviations

CFL Courant-Friedrich-Lewy number

CFD Computational Fluid Dynamics

CSF Continuum Surface Force

DNS Direct Numerical Simulation

FFT Fast Fourier Transform

GCI Grid Convergence Index

PIV Particle Image Velocimetry

SIMPLE Semi Implicit Method for Pressure Linked Equations

UDF User Defined Function

UDM User Defined Memory

UDS User Defined Scalar

VOF Volume of Fluid

Dimensionless Groups

Eo	Eotvos number	$\frac{4r^2\rho_l g}{\sigma}$
Fr	Froude number	$\frac{U_T}{\sqrt{2rg}}$
M	Morton number	$\frac{g\nu_l^4\rho_l^3}{\sigma^3}$
NPS	Normalised Power Spectrum	$\frac{FFT[f(t)]\overline{\mathrm{FFT}[f(t)]}}{\langle \mathrm{FFT}[f(t)]\overline{\mathrm{FFT}[f(t)]}\rangle}$
Re	Reynolds number	$\frac{2rU_T}{\nu_l}$
We	Weber number	$\frac{2r\rho_l {U_T}^2}{\sigma}$

Nomenclature

α_g	Volume fraction of gas	
α_l	Volume fraction of liquid	
β	Skewness angle	$\circ$
Δl	Deviation from vertical line	mm
δx, δy	Instantaneous axial distance in the x and y directions	mm
δ	Dirac delta function	
Γ	Diffusion coefficient	$\mathrm{m^2 s^{-1}}$

γ	Standard deviation of Δl	mm
μ_g	gas viscosity	Pa.s ($\mathrm{kgm^{-1}s^{-1}}$)
μ_l	Liquid viscosity	Pa.s ($\mathrm{kgm^{-1}s^{-1}}$)
ν_l	Kinematic viscosity	$\mathrm{m^2s^{-1}}$
Ω_{ij}	Vorticity tensor	mm
ϕ	An arbitrary scalar or fluid property	
ρ_g	Gas density	$\mathrm{kgm^{-3}}$
ρ_l	Liquid density	$\mathrm{kgm^{-3}}$
σ	Surface tension	$\mathrm{Nm^{-1}}$
θ	Contact angle	$\circ$
θ_c	Coalescence angle	$\circ$
θ_i	Initial contact angle	$\circ$
$\triangle t$	Time interval	s
$\triangle x$	Dimensionless relative distance of bubbles (x-direction)	
$\triangle y$	Dimensionless relative distance of bubbles (y-direction)	
$\triangle z$	Dimensionless relative distance of bubbles (z-direction)	
A	Bubble area	$\mathrm{mm^2}$
a	Bubble major axis	mm

AR	Bubble aspect ratio	
b	Bubble minor axis	mm
B_1	Leading bubble	
B_2	Trailing bubble	
C_D	Drag coefficient	
d_i	Nozzle internal diameter	mm
D_{ij}	Velocity gradient tensor	mm
F	Mass flux	Kg m^{-2}
F_B	Buoyancy force	N
F_D	Drag force	N
F_G	Gravity force	N
F_H	History force	N
F_L	Lift force	N
F_σ	Surface tension force	N
F_{AM}	Added mass force	N
g	Gravitational acceleration	ms^{-2}
J_{12}	Rate of coalescence	mm^3s^{-1}
k	Radius of curvature	m

l	Dimensionless 3D centre-to-centre equilibrium distance between bubbles	
M_w	Molecular weight	kgmol^{-1}
n_1, n_2	Number of bubbles for equivalent radii	
N_r	Number of mesh cell per radius	
P	Pressure	Pa ($\mathrm{kgm}^{-1}\mathrm{s}^{-2}$)
P_o	Operating pressure	Pa ($\mathrm{kgm}^{-1}\mathrm{s}^{-2}$)
q, k	Equation coefficients	
R	Universal gas constant	8.314 J mol^{-1} K^{-1}
r	Bubble radius	mm
r_1	Leading bubble radius	mm
r_2	Trailing bubble radius	mm
R_i	Initial relative bubble size ratio	
r_{ave}	Average radius of bubbles	mm
s	Dimensionless centre to centre separation distance	
S_ϕ	Source term	
S_{ij}	Strain rate tensor	mm
T	Temperature	K
t_c	Coalescence time	ms

u	Bubble velocity in x direction	mms^{-1}
U_s	Slip velocity	mms^{-1}
U_T	Bubble terminal velocity	mms^{-1}
v	Bubble velocity in y direction	mms^{-1}
w	Bubble velocity in z direction	mms^{-1}
x_c	Interaction capture radius	mm
z_f	Dimensionless final distance between bubbles	
z_l	Liquid height	mm
$\mathbf{n}$	Normal vector	
$\mathbf{U}$	Velocity vector	mms^{-1}
t	Time	s

1 INTRODUCTION

1.1 Context

Two-phase flow in which gas bubbles are driven by buoyancy to disperse in liquid continuum is widespread in industrial applications. These applications, for instance, are alkylation, oxidation, Fischer-Tropsch, hydrogenation, halogenation, fermentation, waste water treatment and coal liquefaction (Pan et al., 2000; Joshi, 2001). The reasons for that are many such as simplicity of the design, operation and the high interfacial area per unit volume as well as the higher liquid holdup makes it attractive to the industry. The hydrodynamics of two-phase flow, however, have not yet been understood as the nature of the is complex due to the interaction between the phases. These hydrodynamics are gas holdup or void fraction, bubble size and bubble size distribution, bubble rise velocity, liquid turbulence, bubble-bubble interactions.

The rapid development in computer power over the last few decades has motivated the use of computational fluid dynamics (CFD) in two-phase flow research. This is due to its relatively low cost compared to the costs of experiments. Many approaches have been developed to simulate the simultaneous flow of two-phases.

These inculde Eulerian-Eulrian and Eulerian-Lagrangian methods. Joshi (2001) and Jakobsen et al. (2005) reviewed the chronological development in the numerical simulation which is classified from very simple cases (inviscid flow, one dimensional and averaged values) to highly complicated cases (liquid turbulence, three dimensional and bubble-bubble interaction). Substantial agreement between the experimental and numerical techniques in certain cases has proposed the CFD simulations as a promising tool for the design of two-phase flow systems. However, the optimal design of multiphase flow using CFD is still far. This can be attributed to the limited knowledge and understanding of many factors contributing to this phenomena. The lack of understanding on boundary condition, kernels for turbulence effects, bubble coalescence and breakup and the interfacial momentum exchange impede the formulation of CFD models for two-phase flows (Levy, 1999; Joshi, 2001; Jakobsen et al., 2005). Modelling of these factors in the case of swarm bubbles is not straightforward. Thus, single bubble models and dual bubble models are used as alternatives.

Many studies were done on single bubbles and dual bubbles in pure and contaminated water to understand the rise behaviour and dominant physics (Biesheuvel and Van Wijngaarden, 1982; Van Wijngaarden, 1993; Duineveld, 1994, 1995b; Kok, 1989, 1993a,b; de Vries et al., 2002b; Veldhuis et al., 2008; Tripathi et al., 2015). In those studies, several parameters such as path instability, bubble oscillation, bubble-bubble interaction and coalescence of bubbles have not been well explained and sometimes they contradict each other. For instance, the main cause for path instability is still controversial. In addition, the experimental measure-

ment of shape oscillation using video camera is not quite accurate because the bubble orients vertically and axially as it rises. Hence, the numerical simulation, having access to flow fields and structures, emerges as another option to model the physics of bubble deformation although the feasibility of numerical analyses in capturing such behaviour is challenging. In the literature, detailed three dimensional information on bubble dynamics and the effect of bubble oscillation on the path that a bubble would follow are not established. Furthermore, for dual bubble system, the behaviour is further complicated as the bubbles will affect each other and becomes even more complicated when coalescence of bubbles occurs. This is because the coalescence will result in unpredictable behaviour in bubbly flow.

The studies on bubble-bubble interaction have been mostly theoretical and experiments or numerical simulations are lacking. These gaps of knowledge in many of multiphase flow problems provide the motivation for this research. Thus, this research aims to experimentally and numerically introduce a detailed study about the bubble shape oscillation and its effects on the motion of the bubbles and to validate the numerical simulations against the experiments. Furthermore, the bubble shape oscillation could cause bubble bouncing. This will be addressed when discussing the bubble-bubble interaction later on in this research. The bubble-bubble interaction is investigated in its simplest form when two bubbles freely rising upward and the effect they might bring to each other in case of one approaches the other. As a result to the approaching of bubbles, coalescence of bubbles might occur. Hence, the coalescence of bubbles and the parameters

influencing it will also be highlighted.

1.2 Aims and objectives

The aim of this research is to investigate the behaviour of a single bubble and the interaction between multiple bubbles (diameters larger than capillary length scale) in order to generate better understanding in predicting bubble column flow development. This study is expected to explicitly address the various factors affecting these phenomena and the effect of the initial separation distance (vertically or horizontally) between the bubbles has on the system. The steps to tackle these aims can be summarised as follows:

1. Designing controlled experiments to collect data that measure the complex behaviour of single bubble rising.

2. Validating the single bubble CFD simulations against the experimental measurements.

3. Designing multiple bubbles experimental system to have extensive data.

4. Predictability of numerical approaches against experimental work of multiple bubbles system to be addressed.

5. Constructing empirical correlations that account for the bubble-bubble interaction and the probability of incorporating them into these codes to increase their predictability.

1.3 Thesis outline

Chapter 1 - Introduction This chapter is mainly focused on introducing of the motivation for doing this research and outlining the aims and the objectives of this research and the thesis structure.

Chapter 2 - Literature review The second chapter provides a literature review that constitutes the basis to understand the research topic and the fundamentals related to it for both numerically and experimentally, and critically reviewing previous work of others that is describing the progress so far on the problem studied.

Chapter 3 - Numerical and experimental methodology It is to describe the proposed new adaptive mesh technique with a brief background to other techniques used and then with more detail the developed technique will be presented. This technique will be used in performing the required numerical part for single and dual bubble system. The experimental setup and procedure are also covered in this chapter.

Chapter 4 - Observations of single bubble dynamics This chapter presents the observations of the experimental and numerical single bubble dynamics such as path instabilities and shape oscillation. This chapter considers as a validation material for the Volume of Fluid model, VOF.

Chapter 5 - Interaction of bubble pairs at large separation distances The effect that each bubble brings to its counterpart when they rise together at different configurations at large separation distances is discussed in this chapter.

Experimental and numerical campaigns were conducted to study the interaction between the bubbles that affect the hydrodynamics such the rise velocity.

Chapter 6 - Interaction of bubble pairs at small separation distances This chapter details the coalescence of the bubbles as a result of the interaction between the bubbles at small separation distances. An insight to understanding the coalescence of bubbles is presented in this chapter. A deficiency between the numerical analysis and the experiments is also shown. Then, this chapter contributes to characterise a model for the coalescence between the bubbles.

Chapter 7 - Conclusions and recommendations for future work The main conclusion drawn from this research is presented, along with any rooms for developing the experiments or the numerical techniques in future that have not been covered.

The next chapter will provide a background and relevant critical review on the bubble rise behaviour and bubble-bubble interaction and their related physics. The CFD modelling attempts for these topics of multiphase flow problems are also presented.

2 LITERATURE REVIEW

2.1 Bubble hydrodynamics

The fundamental property of a fluid is that it can not stand shear stress whereas the fluid is no longer in equilibrium. This property essentially makes the fluid different from a solid and it is considered as the basis of Hydrostatics. Now, when a fluid is in motion and there are forces acting on or exerted by the fluid, the study of these effects on the fluid is known as Hydrodynamics (Lamb, 1932; Wu et al., 2007). Bubbles, as an instance, are susceptible to any forces acting on them, therefore, it is more likely that their shape and motion will be influenced. Here, the parameters that affect the motion of bubbles such as fluid properties and forces acting on the bubble will be described.

2.1.1 Dimensionless numbers

In addition to the forces acting on bubbles, other factors such as the properties of surrounding liquid are taken into account using dimensionless analysis. There are seven variables that govern the motion of a bubble. The dimensional analysis of bubble motion was performed by Haberman and Morton (1954) based on five

of them ignoring both the density, ρ_g, and viscosity of the gas, μ_g for simplicity. Therefore, the terminal rise velocity, U_T, can be correlated to those variables as follows

$$U_T = U_T(r, g, \rho_l, \nu_l, \sigma) \tag{2.1}$$

where r denotes the equivalent radius of the bubble, g the gravitational acceleration, ρ_l the density of the surrounding liquid, ν_l the kinematic viscosity of the liquid and σ the surface tension. Many of non dimensional groups were produced considering the inertial force, viscous force, buoyancy and surface tension force, which are the important forces acting on bubble motion. These forces are represented by at least three dimensionless numbers for studying of bubble motion. Here, we introduce four dimensionless groups, which can be described as two dependent (Reynolds number, Re and Weber number, We,) and two independent numbers (Morton number, M and Eotvos number, Eo).

$$\mathrm{Re} = \frac{2rU_T}{\nu_l} \tag{2.2}$$

$$\mathrm{We} = \frac{2r\rho_l U_T^2}{\sigma} \tag{2.3}$$

$$\mathrm{Eo} = \frac{4r^2\rho_l g}{\sigma} \tag{2.4}$$

$$\mathrm{M} = \frac{g\nu_l^4\rho_l^3}{\sigma^3} \tag{2.5}$$

The first two numbers correlate the inertia to viscous force and to surface tension force, respectively. Whereas Eotvos number is the ratio of bouyancy force to surface tension force. Morton number, on the other hand, is a measure of fluid properties. Morton number value of water is about 1.1×10^{-11}, which is considered of low Morton number group. The use of specific non dimensional numbers is subjected to the nature of the physical process and the conditions of intereset whereas sometimes a combination of them could be used. For example, in order to allow for explicit driving of rise velocity, Schmidt (1934) rearranged Equations 2.2 and 2.3 with another dimensionless number Froude number, Fr, (Equation 2.6). Froude number is defined as the ratio of inertia to gravity.

$$\mathrm{Fr} = \frac{U_T}{\sqrt{2rg}} \tag{2.6}$$

Consequently, the other two combined terms were

$$\frac{\mathrm{We}}{\mathrm{Fr}^2} = \frac{4r^2\rho_l g}{\sigma} \tag{2.7}$$

$$\frac{\sqrt[3]{\mathrm{Fr}^2\mathrm{Re}^4}}{\mathrm{We}} = \frac{\sigma}{\rho_l \sqrt[3]{g\nu_l^4}} \tag{2.8}$$

Hence, explicit expression for the rise velocity can be introduced in terms of the dimensionless combinations

$$\frac{2U_T r}{\nu_l} = f\left[\frac{4r^2\rho_l g}{\sigma}, \frac{\sigma}{\rho_l \sqrt[3]{g\nu_l^4}}\right] \tag{2.9}$$

Overall, the dimensionless groups are not only useful for expressing the bubble motion but even the state of the bubble such as shape deformation. The deformation of the bubble is better expressed by the map shown in Figure 2.1 suggested by Grace (Clift et al., 1978).

2.1.2 Forces acting on a rising bubble

The proper modelling of bubbly flow requires the consideration of the various forces acting on bubbles. These forces are contributed in momentum exchange or interaction between the phases. The balance of the forces on a bubble is given by

$$\rho_g \frac{dU}{dt} = F_B + F_D + F_{AM} + F_H + F_G + F_L \tag{2.10}$$

where F_B is the buoyancy force, F_D is the drag force, F_{AM} is the added mass force, F_H is the history force, F_G is the gravity force, and F_L is the lift (transversal) force (Crowe et al., 1996; Delnoij et al., 1997a,b; Chen et al., 2004). The most important forces acting on the bubble are the drag force, the lift force, the history force and the added mass force which will be discussed here.

When a bubble travels steadily through a surrounding liquid, its movement will be hindered by a force called drag force which arises due to form and friction (viscous) drags (Drew and Passman, 1999; Delnoij et al., 1997a). The first type of drag is a result of irregular distribution of pressure around a moving bubble which will cause a net force that opposes the motion (Pang and Wei, 2011). The form drag is linked with shape and size of moving bubbles. The second type is associated with viscosity of liquids which cause a viscous shear inside

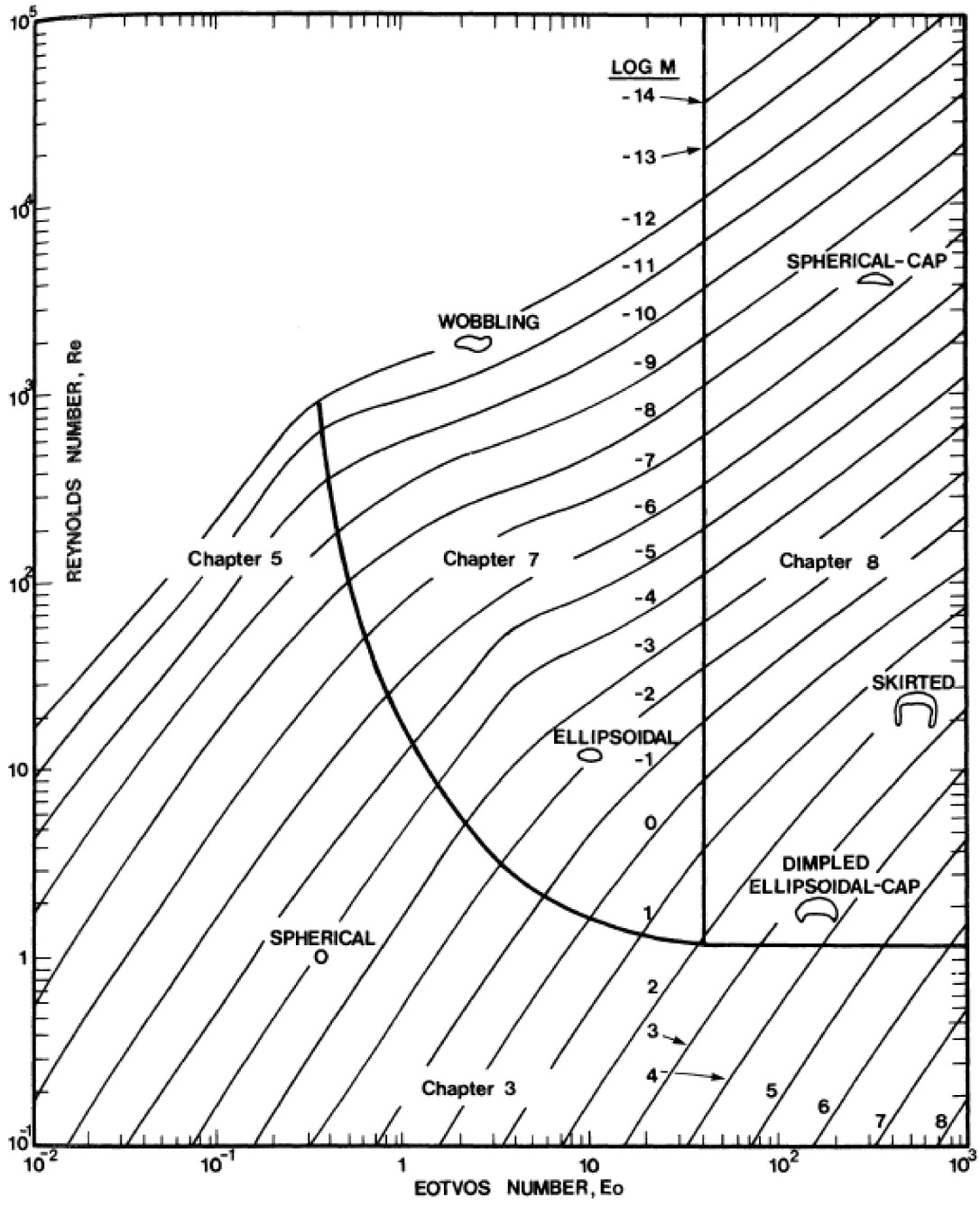


Figure 2.1: Shape regimes map for motion of bubbles and drops in liquids (Clift et al., 1978)

the boundary layer. Both types of forces are affected by Reynolds number of bubbles. As Reynolds number is increased, wakes are formed behind the bubbles, therefore; the magnitude of form drag would increase. At higher Reynolds number of bubbles, $\mathrm{Re} > 100$, viscous force is too small and can be disregarded. The impact of drag force on a sphere moves rectilinearly studied by Odar and Hamilton (1964). A general correlation for the drag force on a bubble can be written as

$$F_D = -\frac{1}{2} C_D \rho_l \pi r^2 U_s^2 \tag{2.11}$$

where r is the bubble radius, U is the bubble velocity and C_D is the drag coefficient. Much of the current focus is on the drag coefficient rather than the drag force model itself. Many factors have a direct influence on C_D. These factors are the Reynolds number of bubbles, the Eotvos number and the Mach number (Crowe et al., 1996; Pang and Wei, 2011). Most of the proposed correlations given C_D in the literature are based on Reynolds number. For example, if Reynolds number, Re, is less than one (Stoke's regime), the drag coefficient can be formulated by Hadamard-Rybczynski equation:

$$C_D = \frac{16}{\mathrm{Re}} \tag{2.12}$$

For higher Reynolds number, C_D can be written as (Clift et al., 1978):

$$C_D = \begin{cases} \mathrm{Re} < 1000 & \frac{24}{\mathrm{Re}}(1 + 0.15\mathrm{Re}^{0.687}) \\ \mathrm{Re} \geq 1000 & 0.44 \end{cases} \tag{2.13}$$

The above correlations are widely used in CFD codes as drag coefficients which were proposed by Schiller and Naumann (1935). Levich et al. (1962) derived the drag coefficient by considering the flow outside the boundary layer, potential flow

$$C_D = \frac{48}{\mathrm{Re}} \tag{2.14}$$

Similarly, Moore (1963) extended Levich's drag coefficient by evaluating the momentum deficit between the boundary layer and the wake. Moore (1965) also derived an expression for distorted bubble by acknowledging the aspect ratio, AR, of the bubble. Equations 2.15 to 2.18 below give the expressions for C_D derived by Moore (1963). The drag coefficient of Moore (1965) showed a good agreement with the experimental work of Duineveld (1995b) and Takagi et al. (2003) on bubble rising in pure water.

$$C_D = \frac{48}{\mathrm{Re}}\left[1 - \frac{2.2}{\sqrt{\mathrm{Re}}}\right] \tag{2.15}$$

$$C_D = \frac{48}{Re}G(AR)\left[1 + \frac{H(AR)}{\sqrt{Re}}\right] \tag{2.16}$$

where

$$G(Ar) = \frac{AR^{\frac{4}{3}}(AR^2-1)\{\sqrt{AR^2-1} - (2-AR^2)\}\mathrm{arcsec}AR}{3(AR^2\mathrm{arcsec}AR - \sqrt{AR^2-1})^2} \tag{2.17}$$

$$H(AR) = 0.0108AR^4 - 0.157AR^3 + 1.5725AR^2 - 2.0195AR - 1.617 \tag{2.18}$$

Few researcher have related drag coefficient to Eotvos number, Eo (Grace, 1973; Ishii and Chawla, 1979; Tomiyama et al., 1998; Tomiyama, 2004). For example, Tomiyama (2004) has defined C_D in terms of Eo as follows:

$$C_D = \frac{8}{3}\frac{\mathrm{Eo}(1-E^2)}{E^{2/3}\mathrm{Eo} + 16(1-E^2)E^{4/3}}F(E)^{-2} \tag{2.19}$$

where

$$F(E) = \frac{\sin^{-1}\sqrt{1-E^2} - E\sqrt{1-E^2}}{1-E^2}$$

$$E = \frac{1}{0.163 + \mathrm{Eo}^{0.757}}$$

However, the drag force estimation in bubbly flows would be more complicated to be estimated because the numerical value of the drag coefficient could be altered by different parameters such as deformable shape of bubbles and bubble-bubble interaction. Based on this, one should consider these effects in any simulation of multiple bubbles rising in a continuum to increase the validity of the applied model.

A bubble moving in sheared liquid encounters a transverse force (normal to the flow direction) called lift force which is responsible for the lateral motion of bubbles. This influence could be attributed to the generated vorticity, which would advect the fluid away or toward the bubble, or shear rate of the surrounding liquid flow field (Pourtousi et al., 2014; Tomiyama et al., 2002a; de Vries et al., 2002a; Kulkarni, 2008). However, the complete mechanism of the lift force has not yet completely understood. The lift force F_L can generally be expressed as

(Kulkarni, 2008):

$$F_L = \frac{1}{2}\pi C_L \rho_l r^2 U_s^2 \tag{2.20}$$

where U_s is the axial slip velocity and C_L is the lift coefficient. It has been reported that the value of C_L is equal to 0.5 if the bubbles are spherical and the liquid is not viscous. Similarly, Zun (1980) and Lance and de Bertodano (1994) have pointed out that this value can be ranging from 0.25 to 0.3 in air-water system.

In general, there are three types of lift forces. The Magnus force which was developed by Magnus (1853) is related to the rotational motion of bubbles affected by transversal force. While, for non-rotating particles, Saffman (1965) found a force acting on small spherical particles in sheared liquids. Finally, when a distorted bubble at low Re number moves in sheared flow, it experiences a velocity distribution around it formed by circulation of liquid. The bubble is affected, in addition, by a wall force if it is close to a wall. This force was pointed out by (Tomiyama et al., 1995). There is a vast body of studies on the lift force and some models have been suggested or extended (Saffman, 1965; Zun, 1980; Auton, 1987; Legendre and Magnaudet, 1998; Bagchi and Balachandar, 2002; Tomiyama et al., 2002b). It is necessary to acknowledge the contribution of the lift force to the lateral migration of deformable bubbles whereas the bubble of deformable shape are more likely to have vortex shedding. Furthermore, the lift force is also important in the case of dual bubble rising. This will be discussed in Section 2.3.

Now, history force or Basset force effect on a bubble is questionable. There is no Basset force acting on a bubble as reported by Yang and Leal (1991). However,

Mei et al. (1994) suggested that a spherical bubble is influenced by Basset force and it is a function of Re. Takagi and Matsumoto (1996) showed numerically the former that effect is valid in the case of Re<50.

Finally, the added mass coefficient is reviewed in detail in Magnaudet and Eames (2000). It is important to state that the added mass evaluation is crucial in case of expanding and oscillating bubble (Ohl et al., 2003; de Vries et al., 2002b). The value of the coefficient of the added mass force was found approaching one-half, analytically derived for high and low Re, and also reasonably valid for an intermediate value of Re (Takagi and Matsumoto, 1996).

2.2 Bubble dynamics

This Thesis focuses on bubbles rising in water at high Reynolds number, Re$\simeq$ 950. At that range of Re, the bubble is no longer spherical; therefore the bubble dynamics are different from small spherical bubbles. Bubbles at large Re show shape oscillation and path instabilities leading to complexities in behaviour compared to spherical bubbles.

2.2.1 Path instabilities

Different types of motions are noticeable for different sizes of bubbles. The spherical, low Re number, bubble rises in rectilinear path. While, at higher Re number, ellipsoidal bubble, follows zigzag and spiral. It is worth here to highlight that there is no unanimous agreement on the conditions that control the mode of path oscillation whether it is zigzag or spiral. The early studies were focused on the

effect of Reynolds and Weber numbers and mainly on the critical values of these dimensionless numbers that led to specify the onset of path instability. (Haberman and Morton, 1954; Saffman, 1956; Hartunian and Sears, 1957; Tsuge and Hibino, 1977). Table 2.1 summarises some of the previous work on critical values for dimensionless numbers that belong to the onset of path instability and the observed regimes.

It is generally argued that there are almost three factors controlling the path of the rising bubble (Fan and Tsuchiya, 1990). First, it is the level of impurities in the liquid, usually water. It is claimed that presence of impurities may result in zigzag path while helical path is observed in pure systems if the equivalent radius of the bubble is less than 2.5 mm and it would exhibit zigzag path when the radius becomes larger (Garner and Hammerton, 1954; Kubota et al., 1967; Tsuge and Hibino, 1971). On the contrary to above, Duineveld (1995b) and Ellingsen and Risso (2001) found no such effect of surfactants on the motion path.

Another factor was triggered by Saffman (1956) when he attributed the spiral motion to the disturbances to the bubble at the injector when it is released or the sudden disturbance afterwards during their path. This has been lately defined as the initial shape oscillation at the release of the bubble from the nozzle and experimentally studied by Wu and Gharib (2002) and Tomiyama et al. (2002a). They reported that a bubble rose with zigzag path if the initial shape oscillations are small. However, when the initial shape oscillations are large, a bubble rose with spiral motion. The mechanism for this effect is not yet clear and controversial as a numerical simulation later done by Yang et al. (2003) failed to reproduce

Table 2.1: Summary of previous work on the onset of path instability and the observed regimes (de Vries, 2001).

	The observed path and critical criteria			Remarks
	rectilinear	**spiral**	**zigzag**	
Haberman and Morton (1954)	Re < 300	300 < Re < 3000	Re > 3000	
Hartunian and Sears (1957)	Re < 202 We < 3.17	Re > 202 We > 3.17	Re > 202 We > 3.17	contaminated pure M < 10^{-4}
Saffman (1956)	r < 0.7 mm Re < 400	r > 1.0 mm -	r > 0.7 mm Re > 400	
Aybers and Tapucu (1969)	r < 0.67 mm Re < 565	0.67 < r < 1.0 mm 565 < Re < 880	r = 1.0 mm 880 < Re < 1350	
Duineveld (1994, 1995b)	r < 0.91 mm We < 3.3 Re < 662	- - -	r > 0.91 mm We > 3.3 Re > 662	

similar result.

Finally, the bubble wake is reported to affect the path instability. The generation of the wake behind the bubble is extensively explained in Fan and Tsuchiya (1990) and Wu et al. (2007). The presence of the wake results in the bubble experiencing a higher form drag. This can be explained, as the bubble rises up, the liquid at the stagnation point losses appreciable amount of its momentum whereas it flows back and towards the sides of the bubble. Due to the presence of the wake behind the bubble, the pressure cannot restore the global value, below the hydrostatic value, and hence a pressure gradient is formed with the pressure higher at the front of the bubble than that at the rear. It has been shown that the structure of the wake consists of double-threaded wake which is inversely signed. Some studies showed that the zigzag motion led to vortex shedding (Lunde and Perkins, 1998; Ellingsen and Risso, 1998; Brücker, 1999). These studies used fine particles or a dye injected into the liquid. Using a different technique of imaging, Schielern technique, de Vries et al. (2002a) found similar results. Solid spheres (Johnson and Patel, 1999) and a bubble with fixed shape (Mougin and Magnaudet, 2001) also showed the same results. We should emphasise that more than one factor could be affecting the path instability and they might be overlapping. For instance, the vortex shedding which is ascribed to the shape oscillation is affecting the path instability. The effect of the overlap between these factors will be discussed in the next section.

2.2.2 Shape oscillation

The study of bubble oscillation emerged from the early work of Savart (1833) and Plateau (1873) who reported the pulsating motions caused by liquids breakup (cited in Tsamopoulos and Brown (1983)). The role of interfacial tension on small-amplitude oscillations of inviscid sphere was identified by Rayleigh (1879) and Lamb (1932) who extended Rayleighs work about different modes of oscillations for spherical bubbles.

The instability of the bubbles was experimentally studied by Hartunian and Sears (1957). They concluded that at very low Morton number the onset of instability was a result of the interplay between the surface tension and the hydrostatic pressure inside the system. They also proposed that the interaction between the shape wobbling (shape oscillation) and the rising of the bubble might have resulted in the transverse migration of the single bubble. Meiron (1989), however, for highly deformed bubbles with an aspect ratio of up to 7, reported that there was no such behaviour in his numerical studies. Fan and Tsuchiya (1990) analysed the periodic behaviour of the bubble wake and observed that the frequencies of shape oscillation and lateral migration for large bubbles were nearly matched.

Until recent years, numerous authors have tried finding out a link between the shape oscillation and the transverse migration of the rising bubble. Lunde and Perkins (1998), for instance, experimentally and theoretically correlated the transient deformable surface of the bubble by means of the variations in the major and minor axes of the bubble in 2D with its velocity. They also theoretically

investigated another hydrodynamic effect of the shape deformation on the isolated bubble behaviour that was vortex shedding. Similar work on the relationship between the surface oscillation and the vortex shedding was done by Veldhuis et al. (2008). Legendre et al. (2012) has experimentally shown that the deformation of bubbles can be described by the Weber and Morton numbers.

Mikaelian et al. (2013) studied the effect of the bubble shape oscillation on the trajectory of bubbles. For single ellipsoidal bubble, they reported a relationship relating the trajectory motion type (zigzag or helical) with the interface wobbling. Also, surface oscillation was correlated against Eotvos and Morton numbers. Both Mikaelian et al. (2013) and Ellingsen and Risso (2001) showed that, for a bubble experiencing a shape oscillation, nearly a plane zigzag was the onset of its path oscillation while it terminated at almost a helix. Their findings agreed well with the studies of Saffman (1956).

Meanwhile, the prominent feature in most of the past theoretical explanations for the non-linearity of bubble behaviour due to the bubble deformation was to linearize and approximate the equations of motion. Hartunian and Sears (1957) approximated the equation of flow to an inviscid flow and considered that the bubble did not deviate largely from its stable shape and linearized the equation depending on that. Their theoretical analyses were in agreement with experiments about the existence of critical Weber number contributing to the mechanism of deformation (oscillation). Two years later, Moore (1959) stated that the bubble shape is quantified depending on various geometric parameters such as the aspect ratio, eccentricity, orientation angle and many others. In his study,

he ignored the viscous stress around the bubble surface and hence he obtained a relationship that related the aspect ratio of the bubble to Weber number. This relationship has reasonably succeeded in correlating the experimental data with the theoretical data of Hartunian and Sears (1957). However, Moore (1959) found that his relationship deviated significantly when the aspect ratio of the bubble was higher than 2. Thus, for highly deformed bubbles, it can be concluded that the theoretical correlations are not the right choice (Fan and Tsuchiya, 1990). On contrary, Meiron (1989) studied the stability and steady rise of inviscid bubbles and reported his disagreement with the findings of Hartunian and Sears regarding the existence of the inviscid instability.

For the numerical computations side, few calculations were carried out to support what the experimentalist have achieved so far. Ryskin and Leal (1984) performed a numerical solution at Reynolds numbers up to 1000 to show that the bubble is enclosed by definite region which is referred as wake structure. The only simulation that shed some light on the direct analysis of the transient shape oscillation was done by Keshavarzi et al. (2014). The experimental behaviour of the single bubble interface was compared against the results of the VOF and CLSVOF methods. It should be noted that their analysis was performed in 2D computational system as that is cheaper in terms of the computational resources. However, the transitional behaviour of the shape deformation of the bubble is complex in nature, adding to that the effect of the wall. Hence, three dimensional study is necessary to address the numerical approaches limitations in capturing such kind of behaviours to that of the experiments. This thesis addresses this

issue and a detailed study is presented in Chapter 4.

2.3 Bubble-bubble interaction

Accurate modelling of bubbly flow requires an approach that accounts for bubble-bubble interaction globally. Single bubble models do not cater for bubble-bubble interaction. Hence, pairwise interaction must be considered for better and more complete modelling because it assumes bubbles in motion affect each other (Magnaudet and Eames, 2000). The interaction of a pair of bubbles rising has been the subject of many investigations, (Harper, 1970; Biesheuvel and Van Wijngaarden, 1982; Kumaran and Koch, 1993a,b; Van Wijngaarden, 1993; Ruzicka, 2000), the majority have been numerical or analytical. Spherical bubbles having the same radius, r, less than 1 mm are assumed to rise at low or moderate Reynolds numbers. For this range of Reynolds number, Re$\approx$500, Kok (1993a) solved the viscous drag force for a pair of spherical bubbles using potential flow theory. For bubbles rising with an initial relative angle, θ_i, the angle between the bubbles centerline and the horizontal axis, he pointed out that the bubbles attract each other when θ_i is between 35° and 54.7°. His solution of the inviscid theory predicted that the trailing bubble had higher drag than the leading one. A similar result was also reported by Harper (1970). The Direct Numerical Simulations (DNS) of Yuan and Prosperetti (1994), however, for spherical bubbles rising in-line showed the opposite situation where the trailing bubble experienced less drag. That was due to the flow field generated by the upward passage of the leading bubble. The flow fields generated for each bubble is shown in Figure 2.2.

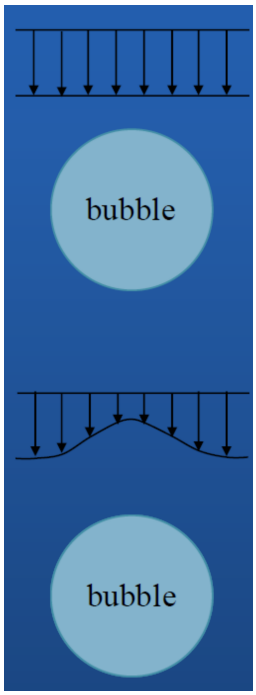


Figure 2.2: Flow fields generated for two bubbles rising in line (Kusuno and Sanada, 2015b)

They also pointed out that the balance between the repulsive and the attractive forces in the wake led the bubbles to maintain an equilibrium distance between them. Their pioneering work established a solid ground for further progress in bubble-bubble interaction studies. Their finding about the equilibrium distance was supported experimentally by Watanabe and Sanada (2006) for intermediate Reynolds number, $5 < \mathrm{Re} < 150$, albeit large differences were observed between the theory and the experiments.

However, for low Reynolds number, that equilibrium distance was not observed in the experiments of Katz and Meneveau (1996). The existence of the equilibrium distance was, however, confirmed by the DNS work of Legendre et al. (2003) for two bubbles rising side by side. It has been recently shown that the case in which the bubbles rising in line is not stable and difficult to be achieved in real situation after the numerical simulations of Hallez and Legendre (2011). This is

because they found that the lift force induced by the vorticity of the leading bubble wake causes the lateral migration of the trailing bubble away from the path of the leading bubble. The magnitude of fluctuations in velocity that the vorticity produce when the bubbles rise side by side was studied by Van Wijngaarden (2005).

For bubbles rising at infinite configuration, bubbles having offset, few studies have been carried out. Hallez and Legendre (2011) derived the drag and lift coefficients for each bubble. Moreover, they described the interaction between the bubbles in terms of three factors. These are: potential effects; viscous correction or Moore (1963) correction; and the influence of the wake when one bubble is located in the wake of another. Baz-Rodríguez et al. (2014) proposed relating the trailing bubble with the flow structure of wake of the leading bubble for bubbles rising in-line by analytical approximation model based on the axial velocity in the wake.

From the experimental perspective, the boundaries between coalescence and bouncing of two bubbles were experimentally studied by many researchers. Duineveld studied the behaviour of two bubbles of different sizes as they encounter each other (Duineveld, 1995a, 1998). In the 1998 paper, for instance, he investigated dual bubbles with radii up to 2 mm, released at different positions (side by side or in-line configurations). He observed that there is a critical Weber number that controls bouncing or coalescing of bubbles. In his work, the horizontal velocity was suggested as the characteristic velocity for the criteria of defining the Weber and Reynolds numbers. Similarly, Lehr et al. (2002) found that large and

small relative velocities as the bubble approached each other resulted in bubble bouncing and coalescence, respectively. On the other hand, Sanada et al. (2009) studied the conditions at which the bubbles coalesce or bounce in terms of dimensionless numbers Reynolds and Weber for bubbles rising side by side. They suggested that the vertical rise velocity of the bubble is better than the horizontal velocity in defining Re and We.

Recently, Kusuno and Sanada (2015a) investigated the rise of clean spherical air bubbles, $0.274 < r < 0.563$ mm, in line motion. Their results showed that the growing lift force of the wake results in the trailing bubble deviating from the vertical position causing a relative motion between the bubbles. Based on that, the pair of bubbles showed four types of motions: approaching, separating, coalescing and overtaking. It was concluded that those types were a function of their initial radius ratio (trailing bubble radius to leading bubble radius) even though they were at an appreciable small deviation (1%) since the larger bubble has generally the higher rise velocity. They reported that the bubbles attracted and collided to each other only when the trailing bubble approached the leading bubble from the side. For contaminated water, the bubbles collided at 90° (Kusuno and Sanada, 2015b). It is noticeable here that the experimental evidence covers only a very small part of the parameter space studying the motion of bubbles at high Reynolds numbers, for example, Re$\simeq$950.

2.4 Coalescence of bubbles

Understanding coalescence of bubbles is very important since it affects bubble size and the bubble size distribution in bubbly flows. Because of this, it is difficult to determine the interfacial area which is needed for mass, momentum and energy balance in bubble columns (Lau et al., 2014). When two bubbles rising side by side, the occurrence of coalescence has to follow three steps in order to be achieved. These steps are: collision of bubbles, liquid film trapped and film rupture. After the collision of bubbles, a small amount of liquid is trapped between colliding bubbles. Then, a critical thickness of the liquid film will be reached because of the draining of liquid that separates the bubbles. Finally, the rupture of this film will occur and lead to coalescence. This will take place only if two bubbles dwell in contact for enough time for the film to reach the critical value which is necessarily required for rupture (Prince and Blanch, 1990; Luo, 1993). However, the bubbles bounce when they have large approaching velocities. This could be due to a considerable increase in the pressure of the liquid film between the bubbles (Chesters and Hofman, 1982; Kok, 1989; Duineveld, 1994; Tsao and Koch, 1994).

Coalescence of bubbles is also influenced by the existence of some contaminations such as surfactants which could prevent the coalescence (Drogaris and Weiland, 1983; Prince and Blanch, 1990; Duineveld, 1994). Figure 2.3 Shows an example of coalescence of bubbles rising side by side. It is noticeable from the literature that the study of coalescence of bubbles has been devoted to bubbles rising side by side whilst the bubbles at different configurations have been rarely

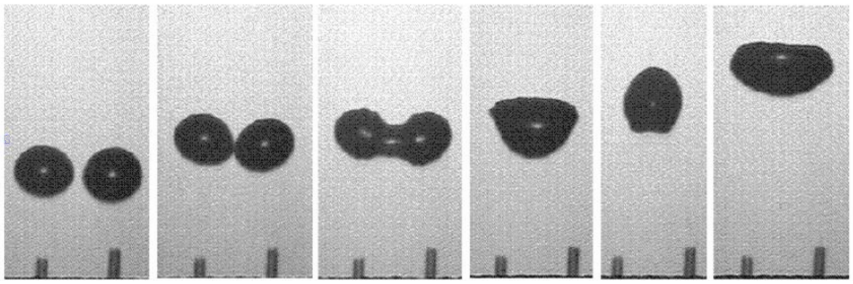


Figure 2.3: Coalescence of two nearly spherical bubbles rising side by side (Duineveld, 1998).

studied. Furthermore, the numerical simulations have been limited to some single cases to validate the models whereas the study of coalescence requires very fine mesh and it is quite difficult to contrive for fixed meshes. The coalescence of bubbles will be discussed in detail when presenting a new adaptive mesh in Chapter 3 and when discussing the interaction of bubbles at small separation distances in Chapter 6.

2.5 Summary

The work presented in this chapter introduces background a critical review on the single bubble dynamics and bubble-bubble interaction. The reviewed literature have shown that the behaviour of rising large bubble is complex and result in the bubble develops shape and path instabilities. This is true when the Reynolds number of the bubble is high, Re>500. Hence, the numerical modelling of deformable bubble dynamics is lacking as it presents a difficulty, particularly in three dimensional simulations. An analysis to the previous investigations showed that detailed information about the numerical simulations efficiency in tracing highly deformed bubbles is not considered.

For the dual bubble system, the review showed that there are number of avenues upon which the scarcity of both the experiments and the numerical simulations is noticeable. The study of spherical bubbles covers the largest part in the experiments of the previous investigations, whereas the non-spherical bubbles interaction is limited. Similarly, the numerical studies on the interaction of deformable bubbles are not available. Much of the research has been analytical or theoretical on small spherical bubbles including approximations to solve the equations of motion. Furthermore, the understanding about the coalescence is not complete particularly the boundaries at which the coalescence could occur. There was no published work that test the validity of the numerical simulations against the experiments in capturing such complex process.

Therefore, the interaction and the coalescence of pairs of deformable bubbles

will be investigated quantitatively at different initial axial separations in an air-water system. To achieve that, an experimental work was designed to produce two bubbles using set of nozzles of 2 mm internal diameter. High speed video camera capable of taking 500 frames/s is used to measure the bubble diameters and the initial separation distance between the bubbles. The predictability of the numerical methods against the experiments will be tested using a new dynamic mesh technique to reduce the computational resources required for such kind of complex processes. The observations reported in Chapter 5 and 6 should result in a better understanding of the mechanisms of bubble-bubble interaction and coalescence. Furthermore, the rise dynamics of single bubble of different sizes released from single nozzles will be also studied and compared with the appropriate Volume of Fluid (VOF) methodology.

3 NUMERICAL AND EXPERIMENTAL METHODOLOGY

3.1 Introduction

This chapter describes the numerical and experimental methodologies used to achieve the goals of this study. The experiments are conducted for the sake of the better understanding of bubble dynamics and bubbles interaction physics. It is also to be used for validating the numerical simulations which will be used to explore many scenarios of bubble dynamics.

3.2 Numerical Methodology

Multiphase flow presents a difficult challenge for numerical analysis. When tracking individual bubbles of air in water, there are a number of difficulties. The phases are separated by an interface across which large jump in viscosity and density is encountered, not to mention the effects of surface tension (Sussman et al., 1999). When the coalescence of two or more bubbles is considered, the problem becomes more complex. Geometrical interface capturing models such as Volume of Fluid (VOF) are widely used in many multiphase flow problems because of its inherent features regarding conserving of mass, efficiency and ease

of implementation. In the literature, there are many studies that were carried out using fixed grid simulations where they used the VOF method (Tomiyama et al., 1993; Hasan and binti Zakaria, 2011). The VOF technique, however, requires fine mesh in and around each bubble to resolve the unsteady behaviour of the interface and in the case of coalescence, the mesh size needed is even finer because the distance between the bubbles at which the coalescence occurs might be smaller than individual cell size. Based on this, using fixed meshes of uniform cell size have an inherently high computational cost. Thus, a new dynamic adaptive mesh has been developed that will be described in detail below.

3.2.1 Governing equations

All the computations implemented in this Thesis were done by solving the governing equations for compressible Newtonian flow. These equations are the continuity and the momentum conservations (Keshavarzi et al., 2014; Xie et al., 2014):

$$\frac{\partial \rho}{\partial t} + \nabla . \left(\rho \mathbf{U}\right) = 0, \tag{3.1}$$

$$\frac{\partial \rho \mathbf{U}}{\partial t} + \left(\mathbf{U} . \nabla\right) \rho \mathbf{U} = -\nabla P + \mu \nabla^2 \mathbf{U} + \rho g + F_\sigma \tag{3.2}$$

where $\mathbf{U}$, P, ρ, μ and F_σ are velocity vector, pressure, bulk density, dynamic viscosity and surface tension force, respectively. Since the VOF approach is used here, the volume fraction advection is carried out using the following scalar equa-

tion:

$$\frac{\partial \alpha_l}{\partial t} + \nabla . (\alpha_l \mathbf{U}) = 0, \tag{3.3}$$

where α_l is an indicator function. If $\alpha_l = 1$, this defines that cell is filled with the liquid phase and if $\alpha_l = 0$, this indicates that the cell has only gas phase inside. A value somewhere between 0 and 1 defines that the cell will have both phases. The source term F_σ in Equation 3.2 is calculated using Continuum Surface Force model (CSF) (Brackbill et al., 1992):

$$F_\sigma = \sigma k \delta \mathbf{n} \tag{3.4}$$

where σ is the surface tension, $\mathbf{n}$ is the normal vector that is given by $\mathbf{n} = \nabla \alpha_l / \mid \nabla \alpha_l \mid$, δ is Dirac delta function which is given by $\mid \nabla \alpha_l \mid$ and k is the surface curvature which can be calculated by:

$$k = \frac{1}{\mathbf{n}} \left[\frac{\mathbf{n}}{\mid \mathbf{n} \mid} \nabla \mid \mathbf{n} \mid - \nabla \mathbf{n} \right] \tag{3.5}$$

We believe that the consideration of the compressibility effects is necessary. That is because the bubble is rising through a hydrostatic pressure gradient and will expand as it rises and this condition is also more realistic at the interface between the phases and the nearby regions. This requires an appropriate equation of state to be used, which is here the ideal gas equation

$$\rho_g = \frac{P_o + P}{\frac{R}{M_w} T} \tag{3.6}$$

where P_o is the operating pressure, P is the local pressure, R is universal gas constant, M_w is the molecular weight and T is the temperature. The temperature is constant as isothermal system was assumed in our computations. Thus, there is no need to solve the energy equation.

3.2.2 Adaptive mesh technique

The use of adaptive meshing, in which only those areas of interest are meshed with very small cells, can overcome the problem of conducting simulations using fixed mesh mixed with VOF method (Almgren et al., 1998). Far from the area of interest, the domain is meshed with coarse cells (the background mesh). Numerous techniques were suggested for the use of adaptively refined mesh for structured and unstructured meshes especially with systems involving indefinite number of spatial scales (Sussman et al., 1999; Sussman, 2005; Theodorakakos and Bergeles, 2004; Zheng et al., 2005; Sochnikov and Efrima, 2003; Popinet, 2009; Losasso et al., 2006; Kohno and Tanahashi, 2004; Greaves, 2004; Dai and Schmidt, 2005; Almgren et al., 1998). Popinet (2009), for example, used an adaptive mesh refinement for structured grid mixed with the VOF method.

Here a method was presented that could cater for surface tension depending on the combination of quad/octree (tree data structure), Continuum Surface Force (CSF) surface tension and a height function that allowed for adaptively refining of grids near the interface only. It should be noted that most of the techniques proposed in the literature are designed to capture the interface during its development and as a result, a small region of flow of the domain is refined. Hence,



they might lose important information in near-field and at the rear of bubble where a wake structure is located. The wake is quite important in understanding coalescence process and hence must be considered when modelling it.

In this Chapter, however, a new dynamic adaptive mesh technique is presented here which is proposed to make capturing of detailed information in such regions very easily though a small increase in the number of cells in the mesh. Another advantage of this technique is that it is not limited by the number of bubbles.

3.2.2.1 Numerical description

The computational cost of solving dual bubble rising is too high particularly in the case of encountering coalescence. In order to overcome this challenge, a new adaptive technique has been developed here that utilises the adaptive mesh refinement and coarsening/refining algorithm in Ansys-Fluent v150. The approach is basically used to reach a desirable level of gridding around the bubbles while they are instantaneously allowed to move together. This technique that will be described here is quite simple and does not contain any complex mathematics. Basically, a Lagrangian equation is solved and to facilitate that use is made of a User Defined Scalar (UDS) transport equation (Fluent, 2014)

$$\frac{\partial \phi}{\partial t} + \frac{\partial}{\partial x_i}\left(F_i \phi - \Gamma \frac{\partial \phi}{\partial x_i}\right) = S_\phi \tag{3.7}$$

where ϕ is an arbitrary scalar or fluid property, F is the mass flux, Γ is the diffusion coefficient and S_ϕ is the source term. The terms on the left hand side are unsteady term, convective term and diffusive term or Laplacian operator

respectively. If the convective flux and unsteady function are not considered, therefore Equation 3.7 will be reduced to:

$$-\frac{\partial}{\partial x_i}\left(\Gamma\frac{\partial\phi}{\partial x_i}\right) = S_\phi \tag{3.8}$$

The solution of the Laplacian is the part of this method which helps to specify the region around the bubbles while they move. A source term of scalar, actually set to +1, is then applied wherever the air volume fraction is greater than a half and a Dirichlet boundary condition, with ϕ set equal to 0, is applied at the walls of the domain. Now, once Fluent has solved the UDS equation, when the value of the UDS in the domain is greater than one quarter of its maximum value, the value of a User Defined Memory (UDM) in that cell is set equal to 1, everywhere else is set to zero. In order to refine the mesh around the region of interest and as the bubbles travel, the solution of the scalar is repeated and the refinement around the bubble is dynamically updated for every certain specified time steps. The refined region appreciably increases to a very small level which is controlled by the coarsening/refining technique. Coarsening and refining of the region utilise the value of the property that has been stored into the predefined UDM. Figure 3.1 shows the dynamic region around the bubble that has been previously recorded into the UDM. An underlying principle associated with this methodology is that the user is not required to set up the important steps such as boundary conditions, grid coarsening and refining, etc. as they are processed internally. The whole procedure described above is introduced into Ansys-Fluent

by an external User Defined Function (UDF).

Numerical methods for an initial adaptive grid have to be provided. As a result, an elliptical region is marked, which becomes more spherical as the bubbles come closer or merge. This is considered another advantage for this technique in dealing with coalescence events because when the marked region is becoming more spherical, a significant decrease in the computational efforts will be gained due to the decrease in the number of the cells in that adaptive region. Figure 3.2 shows the evolution of the marked region for two bubbles rising side by side. The initial region of the grid is chosen depending on the size of the bubble that should be placed into it, for instance, twice the bubble diameter, and regardless of the whole size of the domain, which is left coarse throughout the solution. In summary, the method presented here has an adaptive mesh that responds well to the state of the bubbles whether they deform or shrink to maximise computational efficiency.

3.2.3 Error and uncertainty

The difference between the error and the uncertainty is that the error is the deficiency in any process or activity that is ascribed to lack of knowledge, whereas uncertainty is not attributed to the lack of knowledge (AIAA, 1998). The error associated with a numerical solution may be categorised into many types. These types are spatial dicretisation error, temporal dicretisation error, iteration convergence error, computer programming error and computer round off error. The last two types are incurred by the error in the commercial CFD code and the

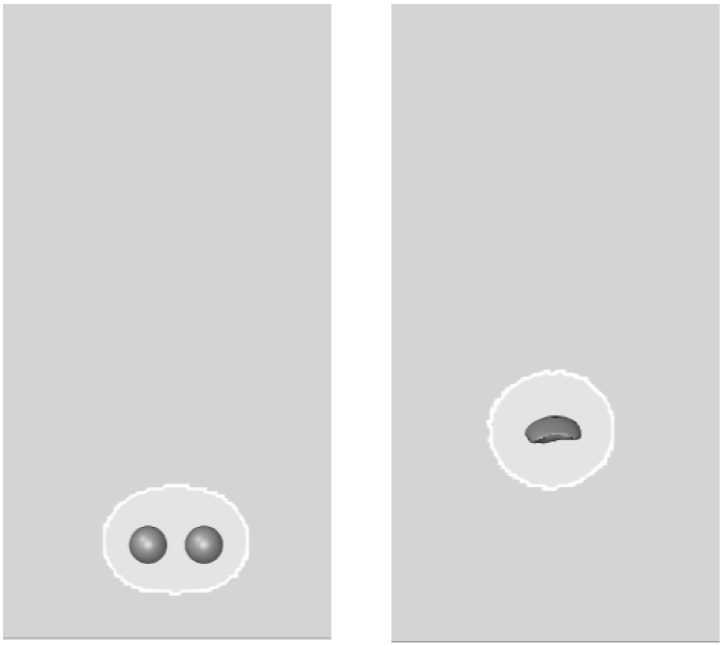


Figure 3.1: Dynamic adaptive mesh region around the bubbles.

digit precision of the computer respectively. These types of error are not covered here. However, the first three error types are quantified with relevant examples.

3.2.3.1 Spatial discretisation error

Spatial discretisation error should be addressed because it provides an indication of how the solution is independent of the grid size. Three increasingly refined background grid sizes were conducted coarse, intermediate and fine. Those grids were 3 mm, 2.5 mm and 2 mm respectively. As a result, the highest level of refinement grid size will be 0.156 mm, 0.125 mm and 0.093 mm. They were defined depending on the refinement factor recommended by Celik et al. (2008) which relates the coarse to the fine grid and this value should be a maximum of 1.3. The spatial descretisation error can then be estimated using a procedure suggested by

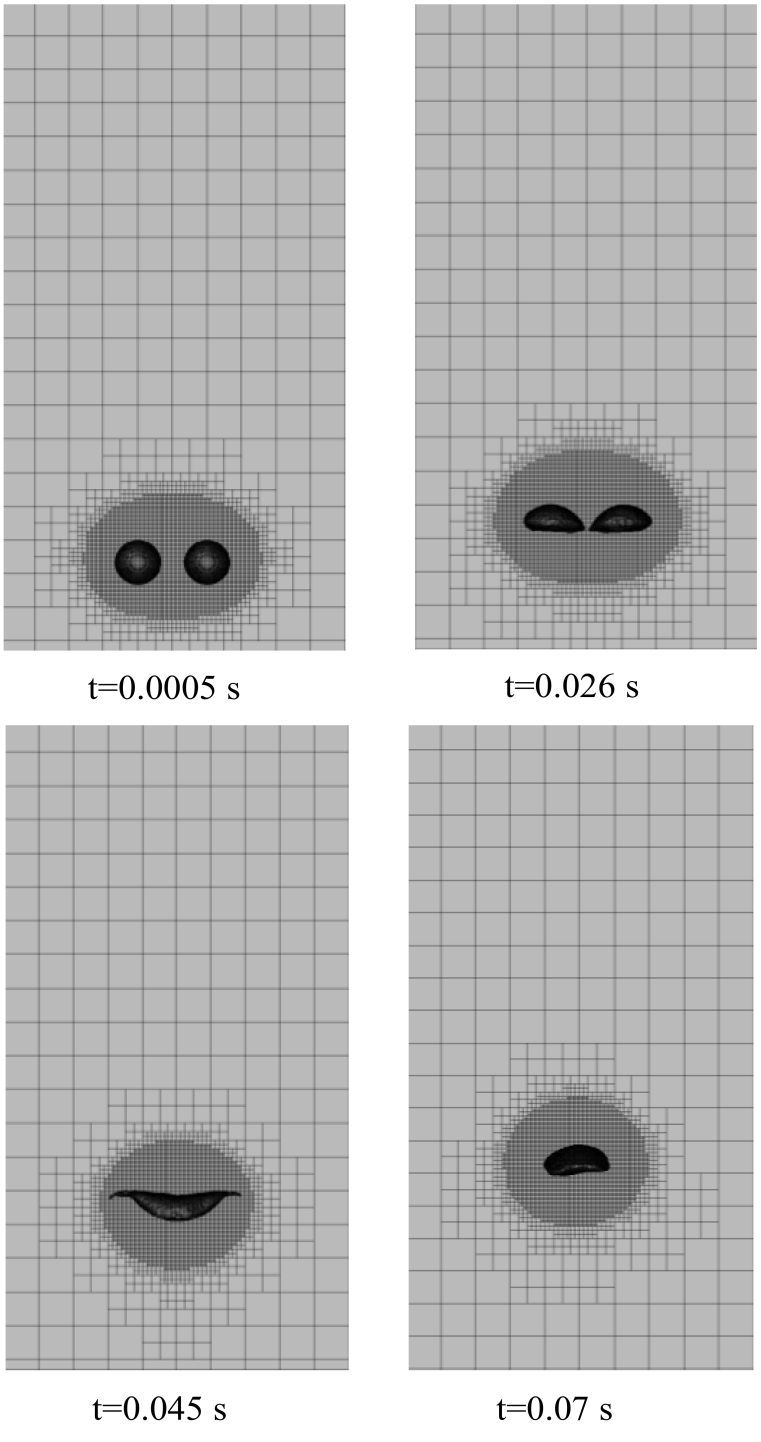


Figure 3.2: Time evolution of the adaptively marked grid.

the same authors and based on the early work of Roache (1998). The procedure is five steps and summarised here.

1. Single grid size, h, is defined.

2. Three increasing cell sizes are defined based on the determination of a certain variable, ϕ, that is performed through a series of simulations. A refinement factor, $H{=}h_2/h_1$, is defined depending on the ratio between each consecutive grid sizes.

3. Now let $h_1 < h_2 < h_3$ and $H_{21}{=}h_2/h_1$, $H_{32} = h_3/h_2$, the apparent order,p, of the method will be calculated using the following relation

$$p = \frac{1}{\ln(H_{21})} \mid \ln \mid \epsilon_{32}/\epsilon_{21} \mid + q(p) \mid \tag{3.9}$$

$$q(p) = \ln\left(\frac{H_{21}^p - s}{H_{32}^p - s}\right) \tag{3.10}$$

$$s = 1.\mathrm{sgn}(\epsilon_{32}/\epsilon_{21}) \tag{3.11}$$

where $\mathrm{sgn}(x)$ is the sign of a real number x and $\epsilon_{32}{=}\phi_3 - \phi_2$, $\epsilon_{21}{=}\phi_2 - \phi_1$.

4. The extrapolated value is then calculated from

$$\phi_{\mathrm{ext}}^{21} = (H_{21}^p \phi_1 - \phi_2)/(H_{21}^p - 1) \tag{3.12}$$

5. The different types of error are finally estimated. Approximate relative error,

$$e_a^{21} = |\frac{\phi_1 - \phi_2}{\phi_1}| \tag{3.13}$$

Extrapolated relative error,

$$e_{\text{ext}}^{21} = |\frac{\phi_{\text{ext}}^{12} - \phi_1}{\phi_{\text{ext}}^{12}}| \tag{3.14}$$

Fine-grid convergence index,

$$\text{GCI}_{\text{fine}}^{21} = \frac{1.25 e_a^{21}}{H_{21}^p - 1} \tag{3.15}$$

The rise velocity of a single air bubble of r= 2 mm was simulated in each case. Table 3.1 lists the size of the grid spacing and the number of the cells required for the computational domain in each case. The results are graphed in Figure 3.3. The error was minimised using the fine and the medium grids compared to the coarse grid. The error predicted by the GCI procedure was 2.23% and 5.74% for the fine and the intermediate mesh, respectively. It is concluded that the finer mesh should be used in simulations that require high resolution such as the transient behaviour of single bubble and coalescence of bubbles. The intermediate mesh can also be in some cases with acceptable accuracy.

Table 3.1: Grid size of the highest level of refinement of the adaptive mesh and the number of the cells in the computational domain.

Case	Highest level grid size [mm]	No. of cells in the domain
1	0.156	773277
2	0.125	1300776
3	0.093	2408660

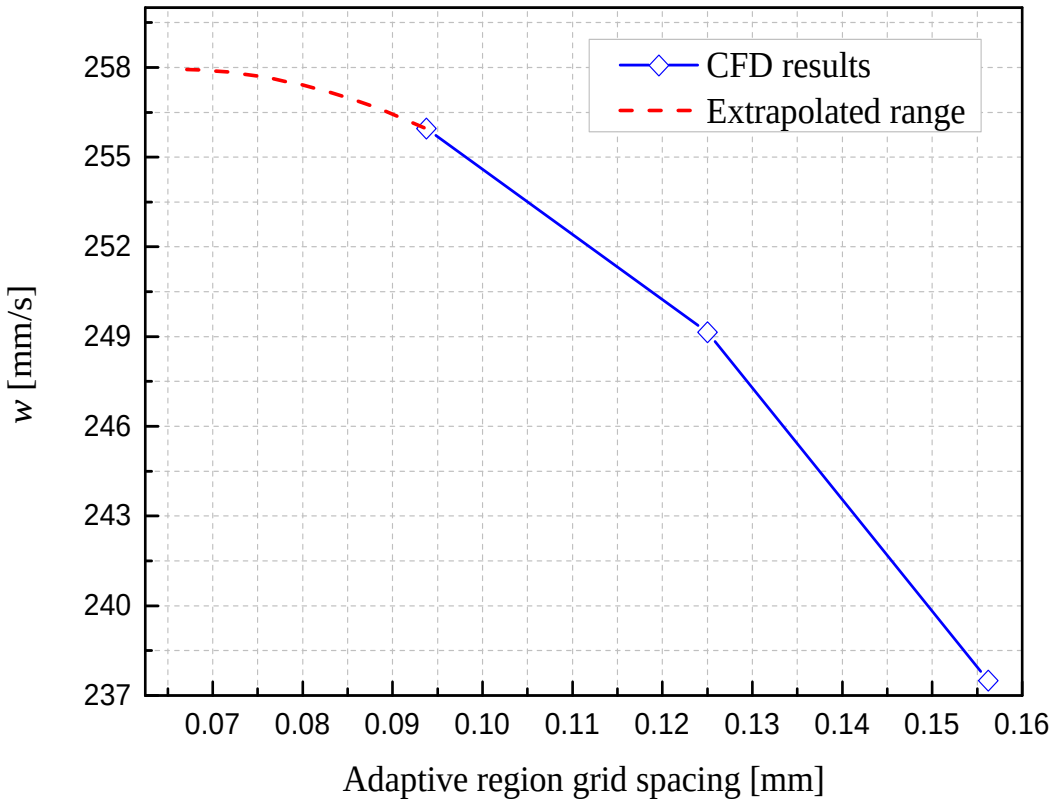


Figure 3.3: The results of average rise velocities computed using the adaptive grid region with each cell spacing 0.093 mm, 0.125 mm and 0.156 mm along with the extrapolated range of rise velocity.

3.2.3.2 Temporal discretisation error

The same procedure for the spatial discretisation error was followed to estimate the error introduced by the size of the time step. Three simulation of three different time steps (5×10^{-5} s, 2.5×10^{-5} s, 1×10^{-5} s) were conducted to achieve that. The comparison was also done on the average velocity of rise of single bubble of 2 mm radius. As shown in Figure 3.4, the GCI error was significantly small, 0.12%, using the smallest time 1×10^{-5}. The error predicted by the intermediate time step, 2.5×10^{-5}, was 0.508%. This indicates that there is no significant difference in the error when using the smallest time step. Therefore, we consider

that the computational cost and the error are well balanced if the intermediate time step, 2.5×10^{-5} s, is used.

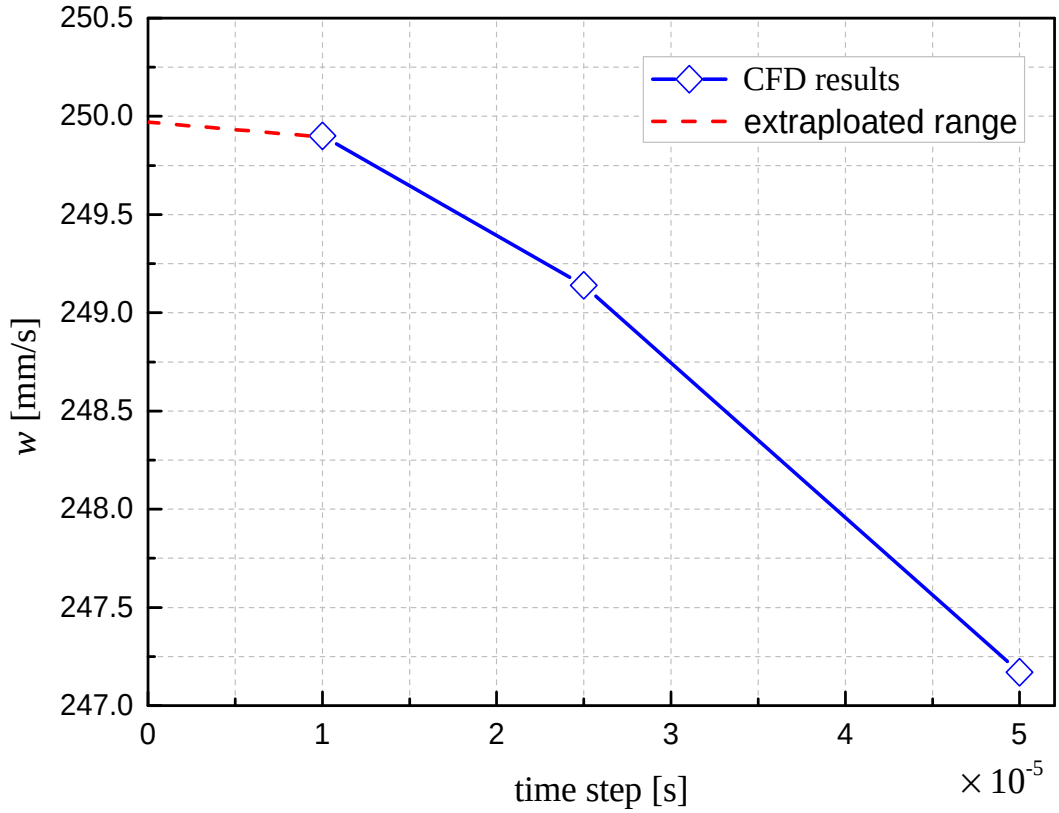


Figure 3.4: The results of average rise velocities predicted by time step size 1×10^{-5} s, 2.5×10^{-5} s and 5×10^{-5} s along with the extrapolated range of rise velocity.

3.2.3.3 Iteration convergence error

The numerical solution of the finite volume method is solved iteratively. The error over the iteration process is investigated by calculating the difference between the guessed values of any variable and the computed values of that variable. This difference is known as residual. It is done by the summation of that difference over all of the computational domain cells to produce an unscaled residual. The unscaled residual is then averaged to get what is called as a global residual. The

solution has to reach a convergence criterion value which is predetermined for each variable being computed. The convergence value was specified as 1×10^{-5} for all the simulations in this Thesis. It is worth mentioning here that the inner iterations required to reach the convergence criterion value were as much as 10 iterations for each time step. Figure 3.5 shows an example of the residual behaviour for single bubble rise of 2 mm radius. This residual was taken while the bubble rose half of the distance through the computational domain. The residual shows that the UDS converges very quickly since it is uncoupled from the other flow equations.

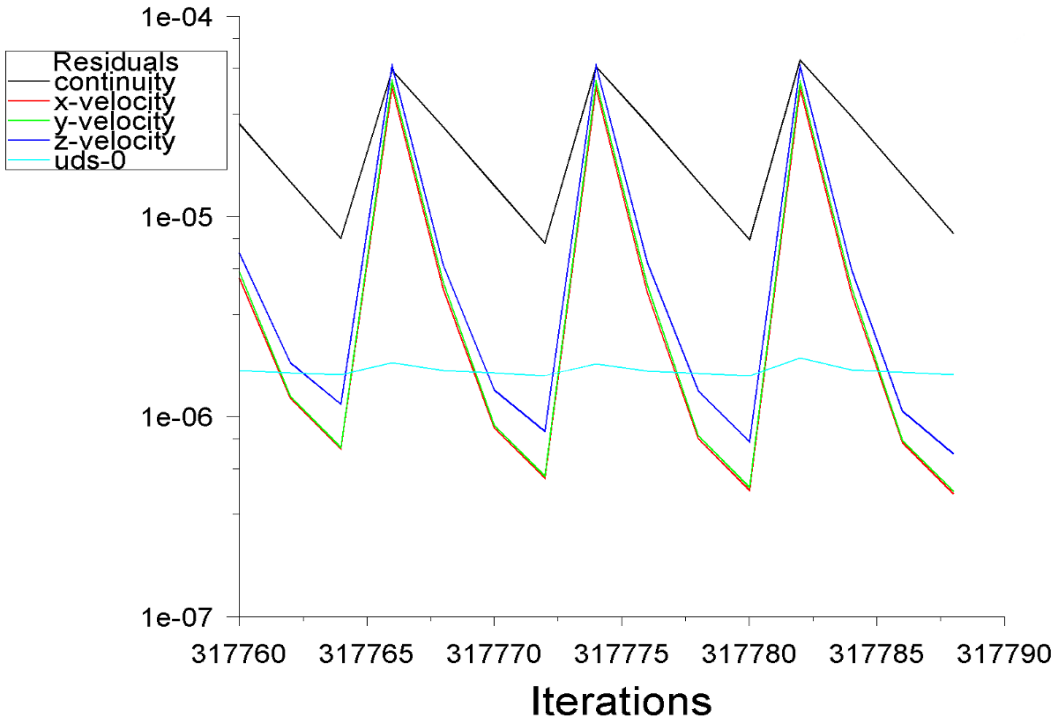


Figure 3.5: Residual example of single air bubble rise of 2 mm radius in water. The residual was recorded while the bubble travelled mid way through the height of the domain.

3.2.4 Numerical testing and verification

3.2.4.1 Initial and boundary conditions

The features of using the proposed adaptive mesh technique will be demonstrated in this section. Verifying that the present method is carried out against different dual bubble system configurations. All the numerical analyses are performed in a 3D domain. The Navier-Stokes equations are discretised using the Finite Volume Method (FVM). The SIMPLE algorithm is used to couple the pressure with the velocity. Geo-Reconstruct is used as the volume fraction capturing scheme, which gives a sharp interface, not smeared like many other interface reconstruction techniques give. The Geo-Reconstruct method is explicit and so the Courant number is kept, for all the cases, to be less than 1 necessitating the very small time steps we saw in Section 3.2.3.2. Some initial and boundary conditions were made to simplify the calculations. A rectangular box is filled with still water, by setting the value of α_l to 1 throughout the domain. Two spherical bubbles of equal sizes at rest are placed at different horizontal and vertical distances from each other. This is done by marking those cells inside the bubble and setting α_l to zero there. The velocity gradient at the walls is included by setting up no-slip boundary condition. A free surface boundary condition was used at the top of the domain. That was achieved by patching a small region of air above the water as can be seen in Figure 3.6. The material properties for the air (subscript g) and water (subscript l) phases were: ρ_l=998 kg/m^3, ρ_g=1.225 kg/m^3, μ_l=0.001 N.s/m^2, μ_g=1.8$\times$10^{-5} N.s/m^2 and σ=0.073 N/m, which give us equivalent Reynold num-

ber ($2\rho_l wr/\mu_l$) of Re=958 and equivalent Eotvos number ($4\rho_l gr^2/\sigma$) of Eo=2.15.

3.2.4.2 Bubbles rising side by side

In this example, two identical spherical air bubbles with radii of 2 mm were located near the bottom of the domain, either side of the centre of the xy plane. The bubbles were set to rise freely. The separation distance between the bubbles was set to be $3\,r$ from centre to centre. The computational domain dimensions were carefully constructed to firstly eliminate the wall effects on the bubbles to a lesser extent by making its cross-section 60×60 mm, and secondly to ensure that the terminal velocity can be reached for the coalesced bubble by making the height of the domain large enough.

Figure 3.7 depicts the predicted coalescence from the numerical setup of bubbles lined up horizontally. Here, isosurfaces of $\alpha_l = 0.5$ are shown depicting the surface of the bubble. It can be seen from Figure 3.7 that as the bubbles rose due to the buoyancy force, they experienced a good deal of deformation. The more the bubbles rose, the more deformation they experienced. Thus, they approached each other and gradually the distance between them became smaller until then a bridge was formed connecting both bubbles. This predicted coalescence appeared unrealistic as the images showed that the bubbles were touching but were being attracted to each other. Therefore, two contour lines of volume fraction function at 0.1 and 0.5 are presented in Figure 3.8. These contour lines show that the bubbles were very close and touching each other particularly at the contour volume

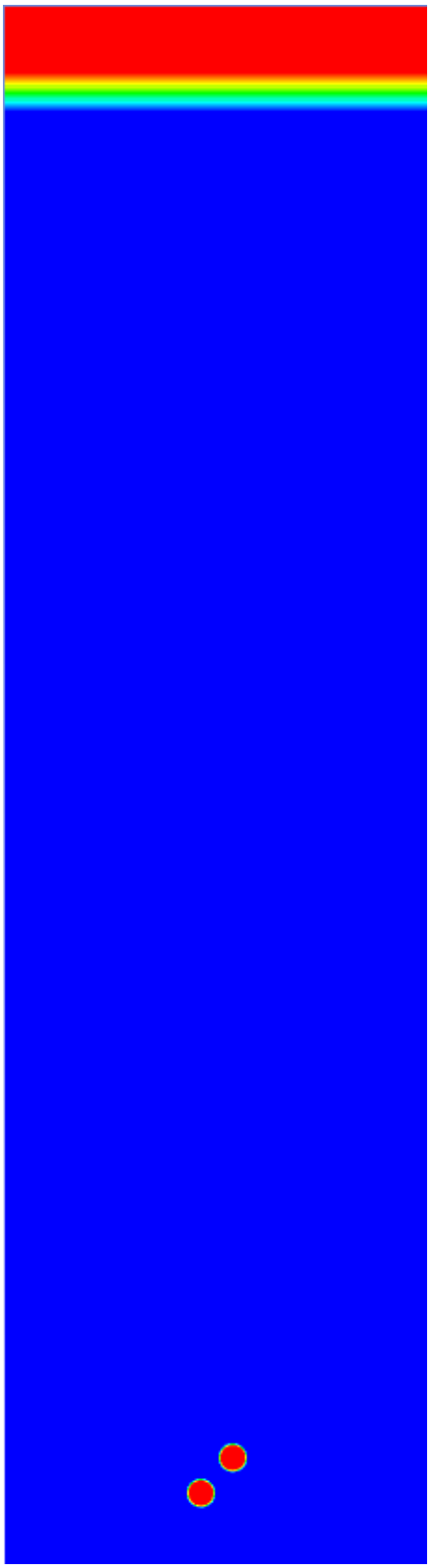


Figure 3.6: An example of the initial setup of a simulation run which shows the free surface boundary condition above the water and two spherical bubbles rising having an offset.

fraction 0.1 and so the choice of α_l when defining what is meant by the surface of the bubble is a key issue when bubbles coalesce. Rapid coalescence can be attributed to the formation of those air bridges as they have large surface tension force. Finally, the bubbles coalesced into a larger one which experienced volume and surface oscillations. The magnitude and rate of decay of these oscillations is something that could be pursued.

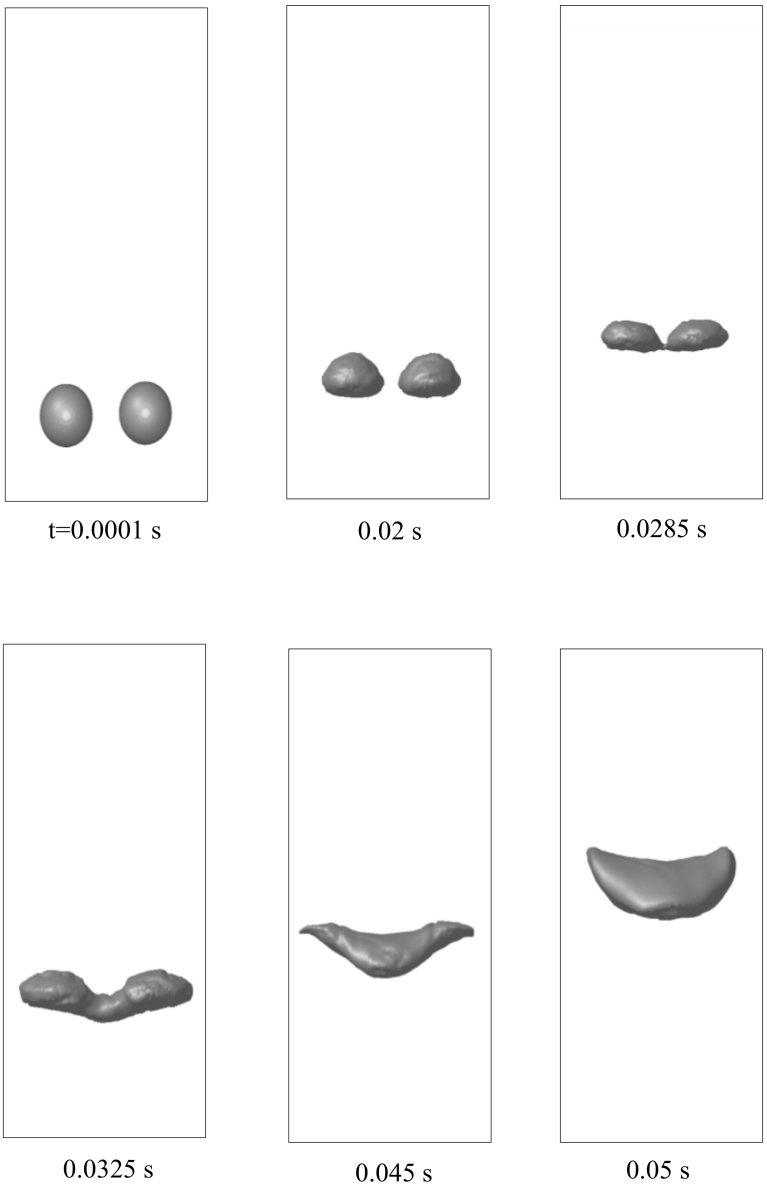


Figure 3.7: Time evolution of coalescence predicted by our adaptive grid methodology.

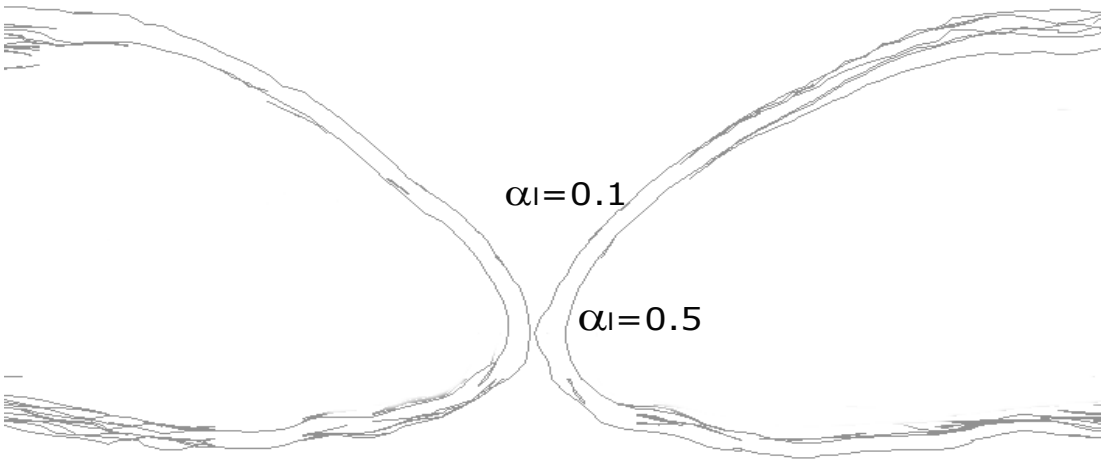


Figure 3.8: Encounter of bubbles at contour lines α_l=0.1 and 0.5.

Next, a comparison between the adaptive mesh technique and a fixed mesh has been made to show how accurate the adaptation technique is in capturing general features such as shape before and after coalescence, as can be seen in Figure 3.9. A simple comparison can also be made over the total number of the cells needed in both cases (fixed and adaptive meshes) though creating a very fine fixed grid for the whole domain would be impossible. For fixed mesh simulation ($10 \times 10 \times 180\,\text{mm}$), a huge number of cells is required which is around 57 million cell to achieve similar resolution for the adaptive mesh case that needed only 630000 cells as initial gridding. That means that the new method utilises only 1.1% of the total number of cells required for fixed mesh simulation. Therefore, a smaller rectangular region ($10 \times 10 \times 25\,\text{mm}$) was refined to make such comparison practicable. It is also worth mentioning that although the total number of cells for the adaptive simulation is increasing as the bubbles rise, it decreases

again when they get closer. However, for the fixed mesh simulation is always kept constant during the whole simulation. An independent grid analysis was also carried out to check the optimum level of gridding for better capturing of all the related hydrodynamics in coalescence processes.

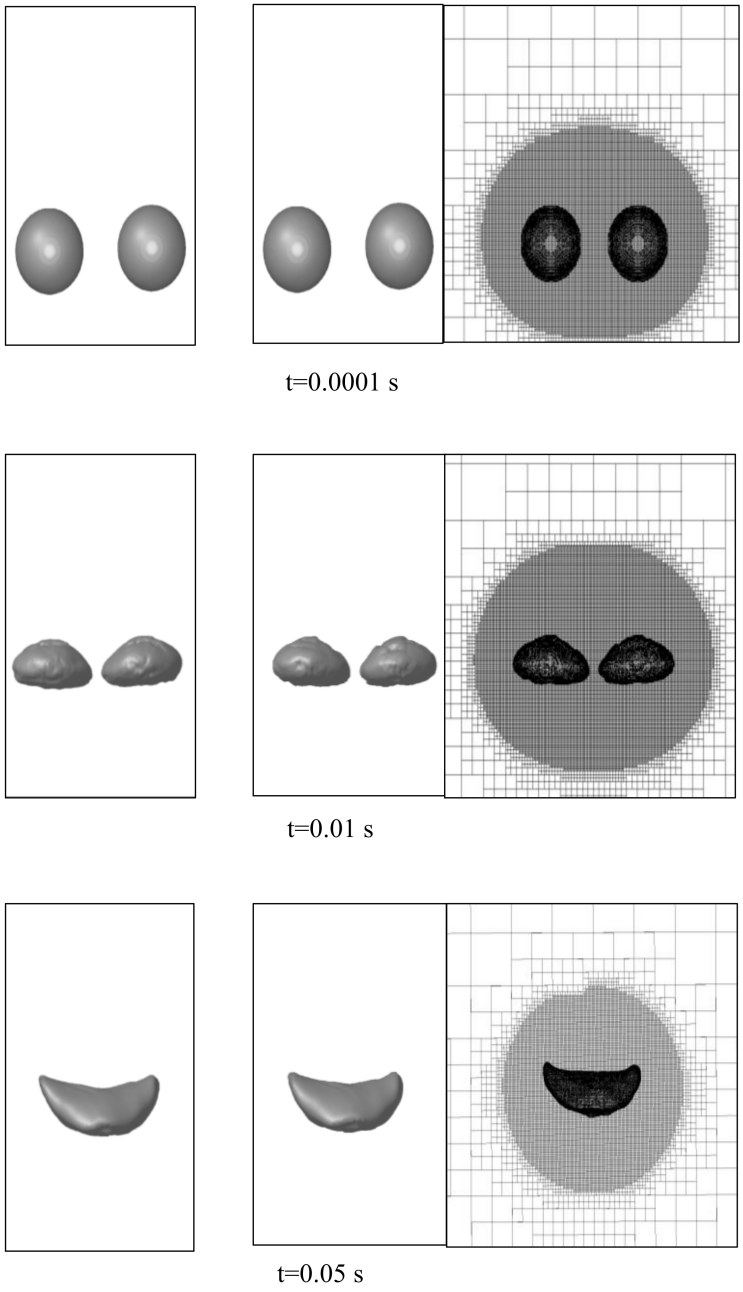


Figure 3.9: Comparison between fixed mesh (left column) and 5 levels of dynamic adaptive mesh (middle and right columns).

Figure 3.10 exhibits a comparison between the topological changes over a

coalesced bubble that was obtained by a coarse mesh using 4 levels of refinements (0.186 mm) and by a fine mesh using 5 levels of refinements (0.093 mm). Although there is a slight change with respect to the shape of the merged bubble, the coarser mesh seems that it can be used with reasonable accuracy. However, if the topology of the bubble is incorporated in some calculations such as surface area, then the finer mesh should be used.

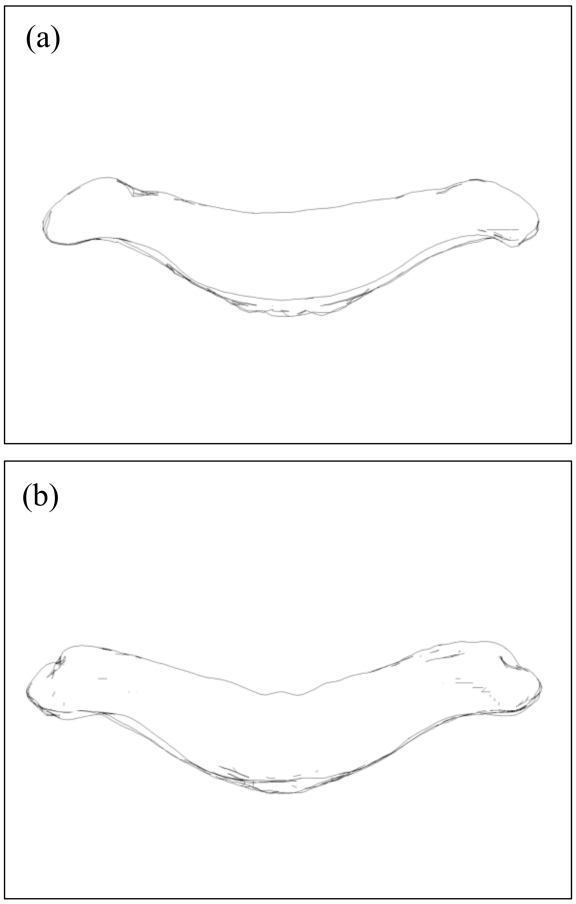


Figure 3.10: General topology of coalesced bubble captured at (a) 4 levels (b) 5 levels of adaptive mesh refinement.

The computational efficiency of the new adaptive methodology was demonstrated in terms of the computational efforts. The time history of reduction, during simulation, in the total number of cells required to keep the bubbles enclosed by our marked region is shown in Figure 3.11. An increase can be seen at

the initial grid adapting as the initial region was appreciably large and it kept increasing while the bubbles were getting more deformed. Then, as the bubbles come closer to each other, the cell count decreases significantly. A further decrease is noticeable after the coalescence of bubbles and the subsequent formation of a larger, single bubble. The total number of elements has decreased to around 1.37 million, which is relatively computationally cheap when compared to other simulations in literature which needed around 2 million cells in a two-dimensional domain to capture single bubble rising, for example Keshavarzi et al. (2014).

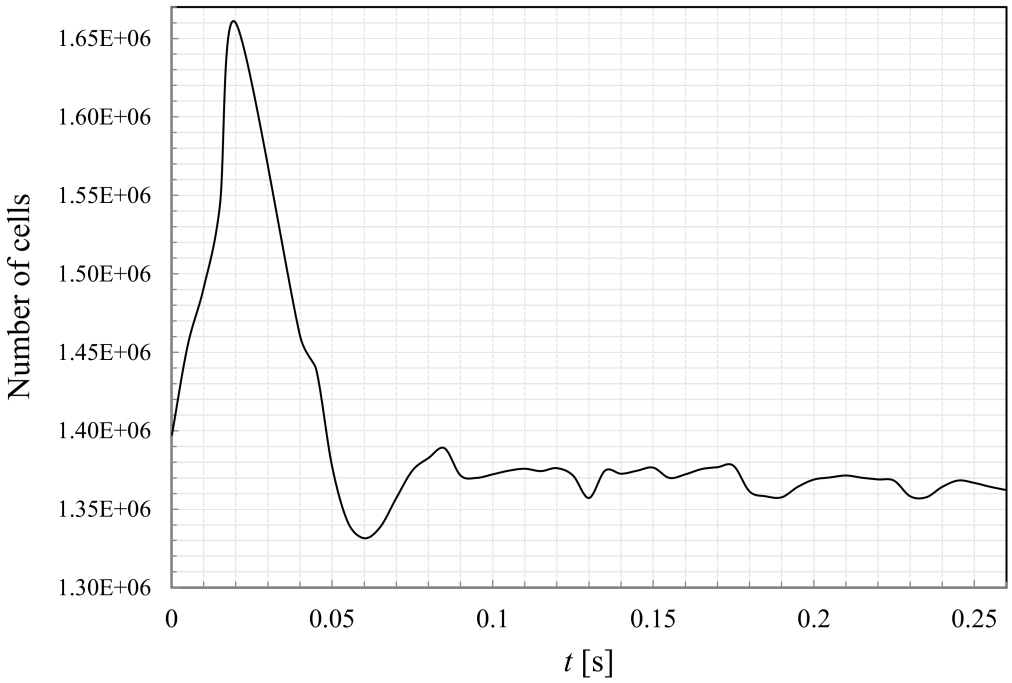


Figure 3.11: Total number of cells used for simulating two rising bubbles and for 5 adaptive mesh refinement levels.

3.2.4.3 Bubbles rising with vertical and horizontal offsets

A pair of spherical bubbles of 2 mm radius was placed in a way that there was an offset in both horizontal and vertical directions (an angle between their lines of centres and the vertical direction) at initial separation equals to $2r$ in both

the vertical and horizontal directions. The setup and the physical properties are the same as in Section 3.2.1. This arrangement of bubbles was selected because we wanted to test the automatic response of the marked region to adapt itself in an economic way that takes into account different configurations of bubbles. The coalescence predicted and the marked region response to the position of the bubbles one to another are exhibited in Figure 3.12. In this coalescence configuration, the bubbles are still affecting each other due to small initial separation. Both bubbles rose from their initial state and deformed due to the relatively high Reynolds number of the bubbles. It seemed that initially they travelled apart from each other. Then, they came closer and started to affect each other. As a result, the leading one attracted the following one due to the wake formed behind it and before coalescence, it is noted that the shape of the trailing bubble changed when it entered the wake region. The trailing bubble, therefore, was accelerated until it reached the leading one and consequently they coalesced. Similar to the behaviour experienced in side by side bubbles rising, there was a bridge that was formed between the bubbles prior to their merging. It should be noted from Figure 3.12 that the initially marked region around the bubbles is still ellipsoidal but it is clear how it does detect and rearrange itself in a position that matches the new configuration of the bubbles. This confirms that the adaptive region is capable of dealing with any configuration of bubbles that it is presented with.

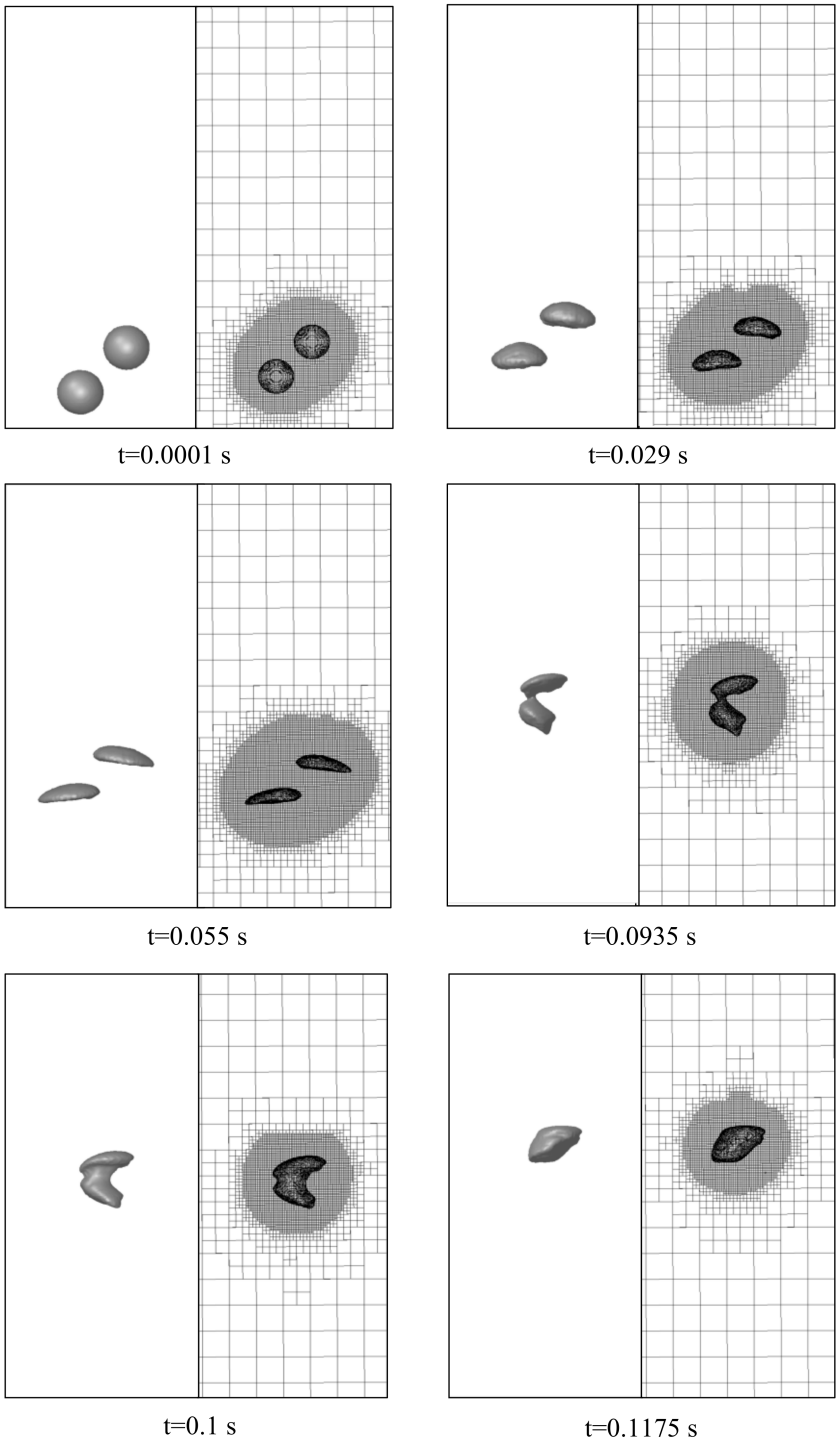


Figure 3.12: Predicted coalescence and the marked region tracking the air phase.

3.3 Experimental setup and procedure

An experimental rig was built to investigate the rise of single bubble and pairwise interaction of bubbles. A rectangular box was fabricated with a cross section of 100 × 100 mm which was large enough to eliminate wall effects on the bubbles. The height of the box was 500 mm. The generation of single or dual bubbles was accomplished by using sets of nozzles with various internal diameters placed at the centre of the box. They were fixed into a brass base that was designed so that the nozzles can be fitted and then removed as many of them had to be used to represent different separation of nozzles and therefore different sizes of single bubbles or different configurations of dual bubbles under investigation. The air is pumped into each nozzle through a syringe pump with relatively low flowrate to reduce background perturbations induced by the wakes of a rising series of bubbles. Two syringe pumps of the same model were used to release a pair of bubbles. Still tap water was used here as a liquid phase. The experiments were carried out at room temperature (≈21 °C) and atmospheric pressure. Figure 3.13 shows a schematic diagram of the experimental apparatus. Figure 3.14 depicts a photograph of the experimental setup. In order to get two 2D perpendicular projections of the same bubble simultaneously, a mirror (220 mm× 60 mm), as was suggested by Lunde and Perkins (1998), was positioned at an angle of 45° to the centreline of the camera outside the rig. Therefore, two planes (views) were projected on the lens of the camera that were xz-plane, which was directly from the box to the lens of the camera and yz-plane, which was the reflection of the

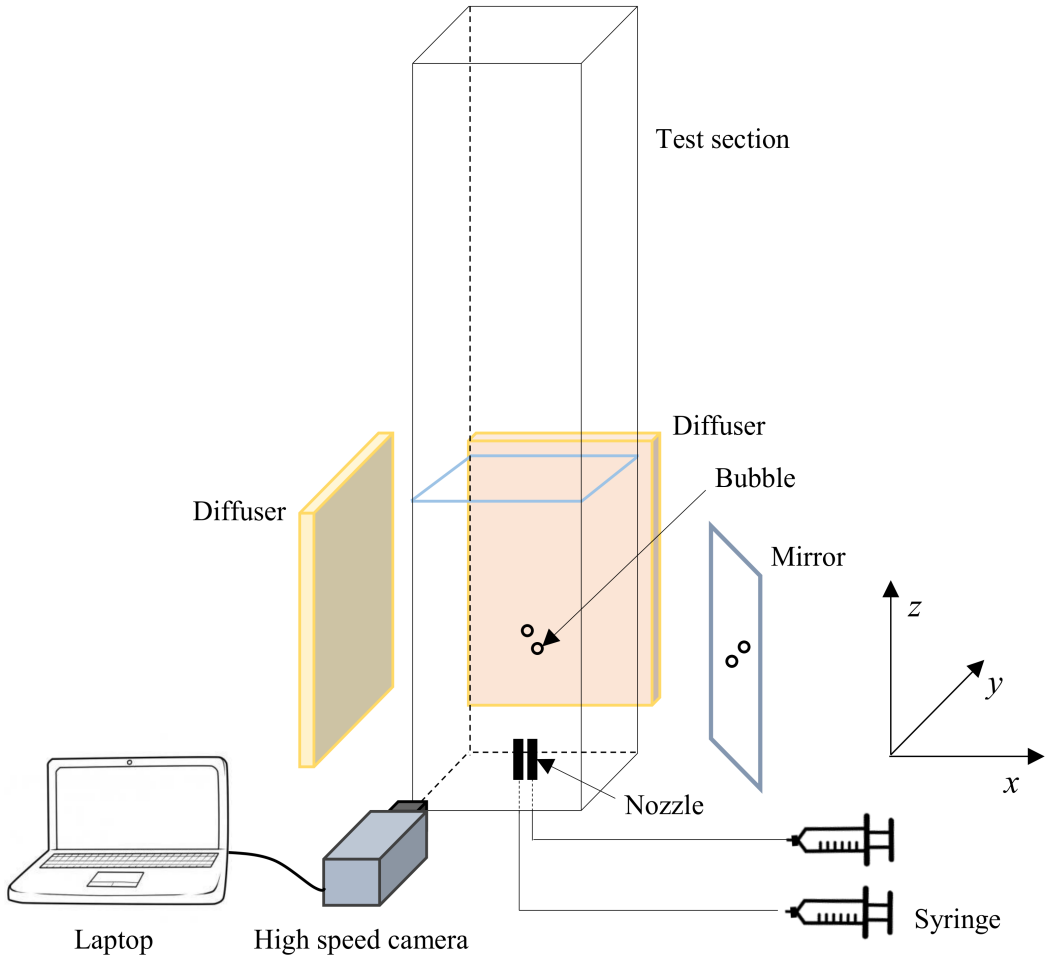


Figure 3.13: Schematic of the experimental apparatus.

bubble into the mirror. A schematic diagram of the top view of the test section is shown in Figure 3.15.

Because of the use of the mirror, two light sources were used to illuminate the area of recording for both the camera and the mirror. A light diffuser was also placed between each light source and the box to ensure the even distribution of the light inside the box and the mirror views. It is important in the experiment to balance the light sources for the bubble in the column and the mirror because sometimes the light is scattered from the bubble surface while it is wobbling

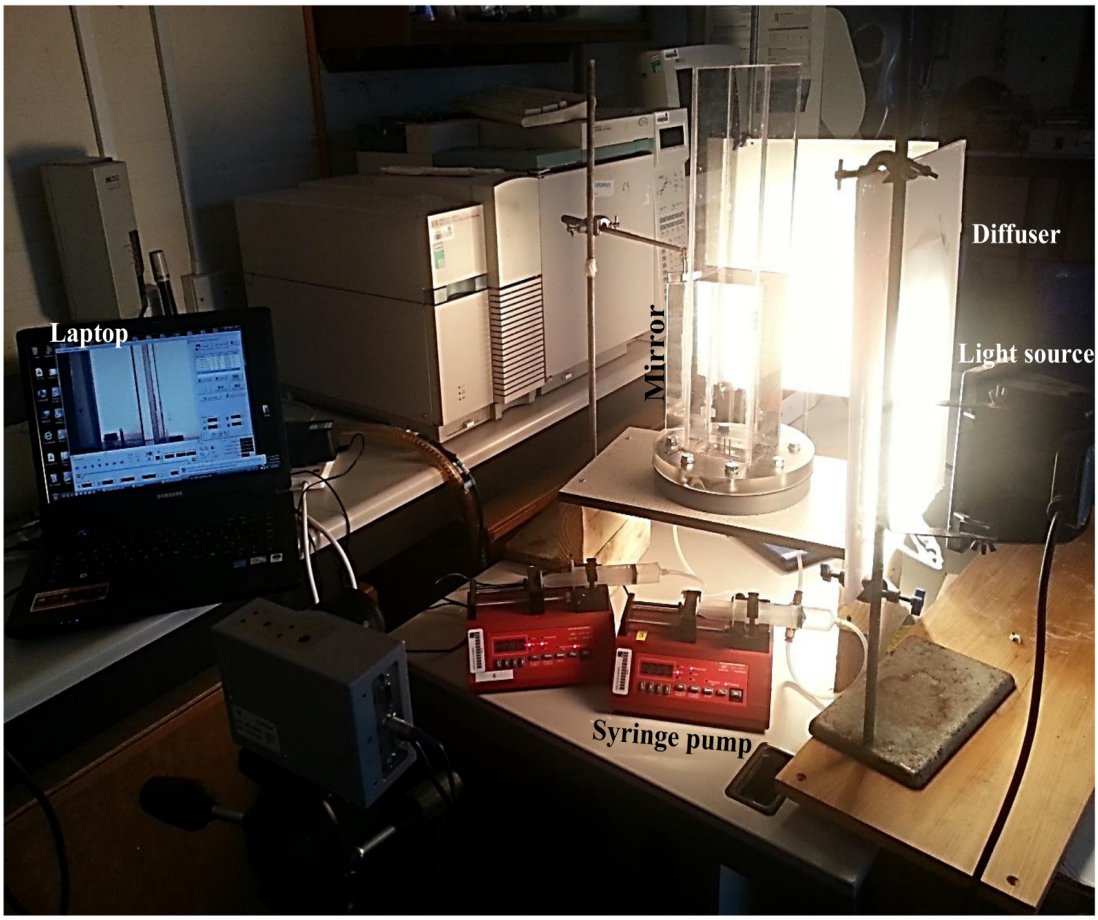


Figure 3.14: Photograph of the experimental setup.

particularly for the projection of the bubble in the direct view. More detail about the experimental setup of the study of single bubbles or dual bubble rising will be available in their relevant chapters.

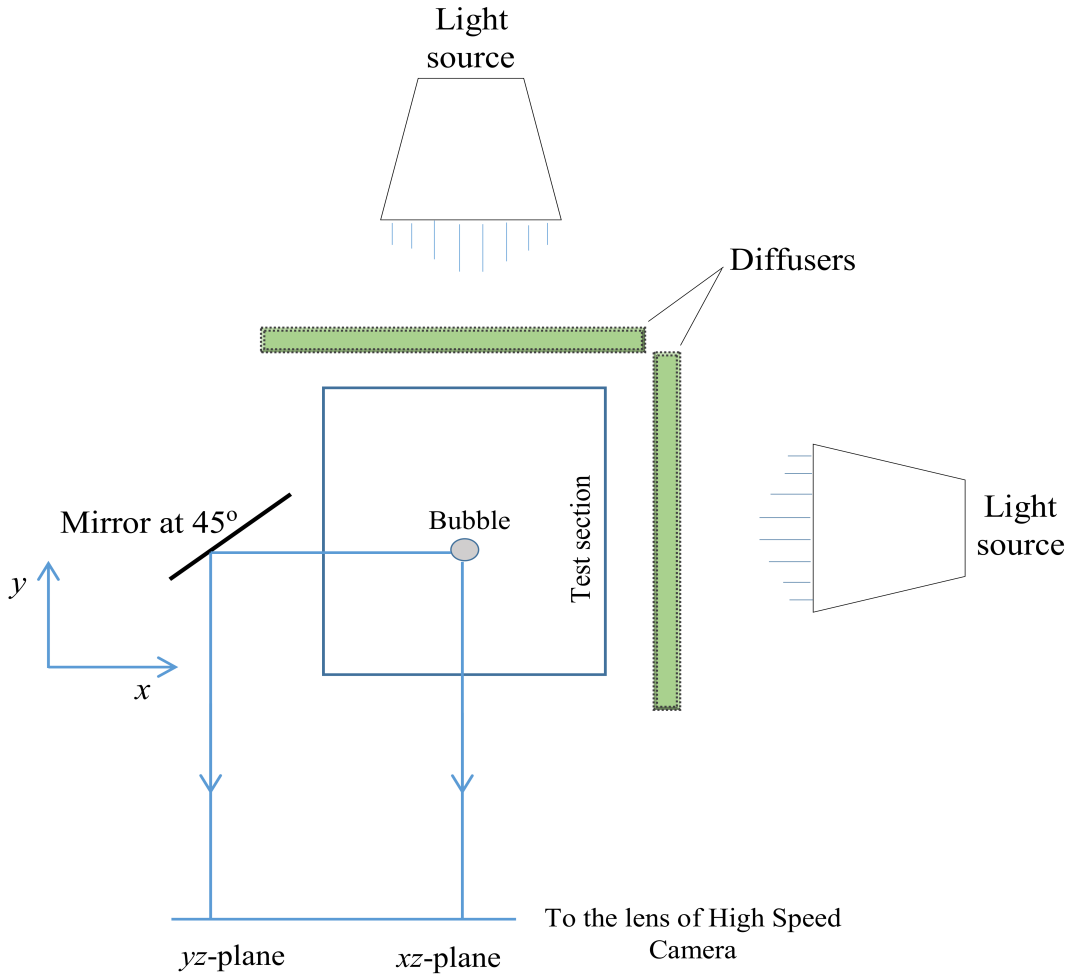


Figure 3.15: Schematic top view of the test section.

3.4 Image processing and analysing procedures

Various image processing techniques have been used here while tracking the progress of the bubbles. These measurements involve bubble information such as dimensional measurements, motion and instantaneous shape oscillation. The bubble parameters are measured by detecting and identifying the bubble as an individual object in each frame. The rise velocity of the bubble, for instance, is calculated by knowing the frame rate and tracking the displacement field of

the centre of mass in pixels which is calibrated to a spatial field. However, image processing is not straightforward as many techniques and many steps are required before accurate measurements can be obtained from the images.

3.4.1 Camera calibration

The use of lenses/cameras in an application such as this requires a calibration process. Points from the real world are projected onto flat images using the lenses. However, due to the distortion of the lenses or flaws in the design of the camera, those points are not precisely represented and depend on many intrinsic values that are found by the calibration process (Weng et al., 1992). Once the intrinsic values are obtained, the original image will then be undistorted so that the pixels in the image can correspond to the real points. The intrinsic values are described below (Mathworks, 2014; Zhang, 2000)

Focal length: The distance between the focal point and the image plane (Figure 3.16a).

Principal points: A point where the optical axis and image plane intersect (Figure 3.16b).

Skew coefficient: Indicates whether the x and z pixel axes are perpendicular or not (Figure 3.16c).

Radial distortion: The alteration of the original shape in the image plane.

Tangential distortion: Indicates the parallelism between the image plane and the lens.

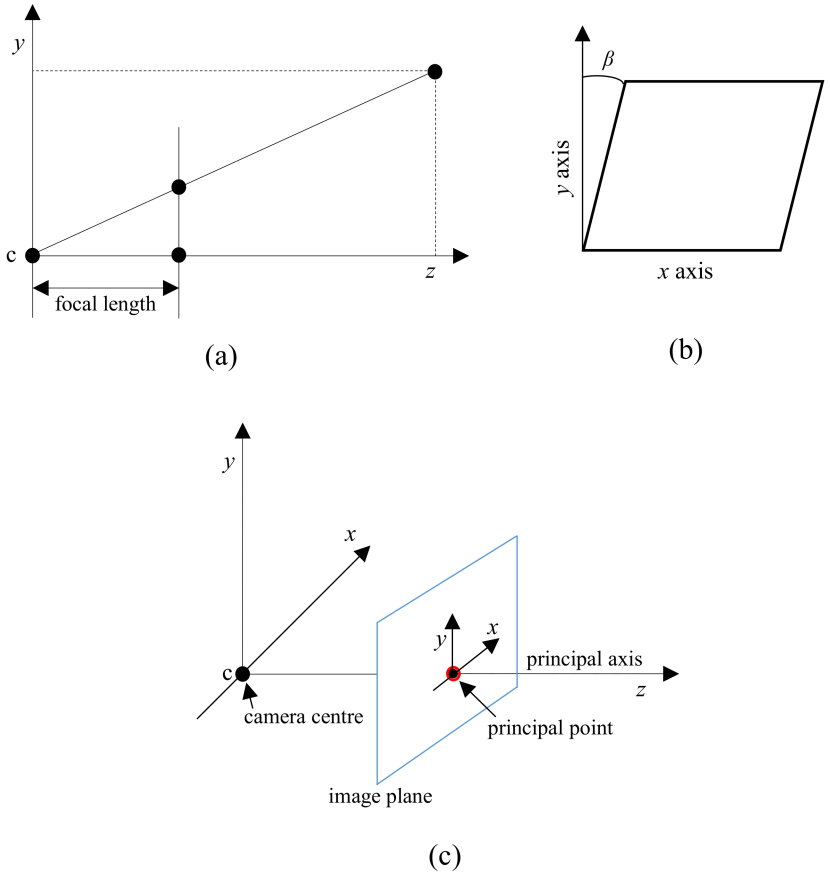


Figure 3.16: Principle camera parameters (a) focal length (b) skew coefficient (c) principal point (Mathworks, 2014).

A flat checkerboard plate was used as a calibrating object because it has many points which are collinear in the real view. It is recommended to have ten to twenty of the checkerboard photographs for better accuracy. Here, thirteen of them were utilised. The deviation in the intersections of the calibrated images was extracted which was at an excess of 0.53 pixels as shown in Figure 3.17. The errors embedded in lens distortion are now directly re-projected depending on the calibrated images. Figure 3.18 shows the re-projected errors due to lens distortion.

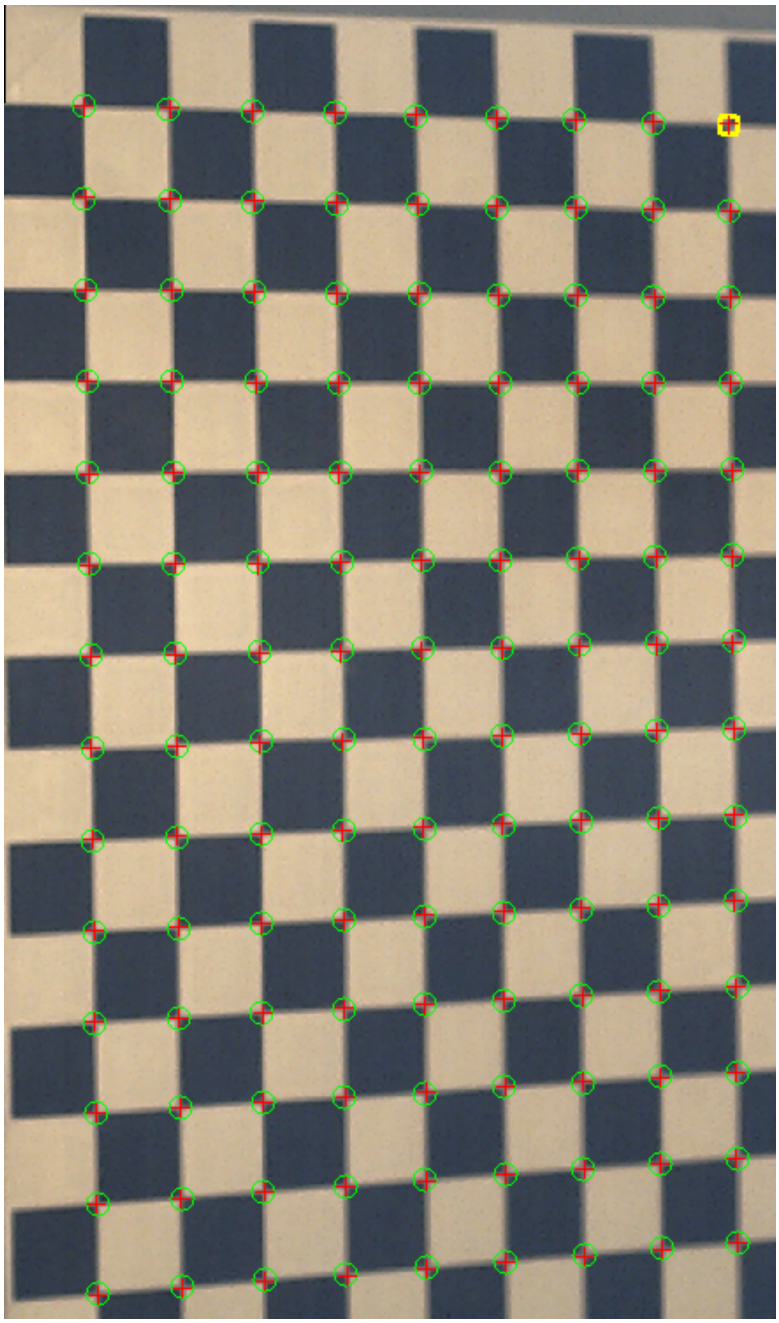


Figure 3.17: Extraction of corners from calibration image.

Next, in order to decide on the degree of distortion, it is important to visit the intrinsic parameters which are easily extracted. They are described with uncertainties below:

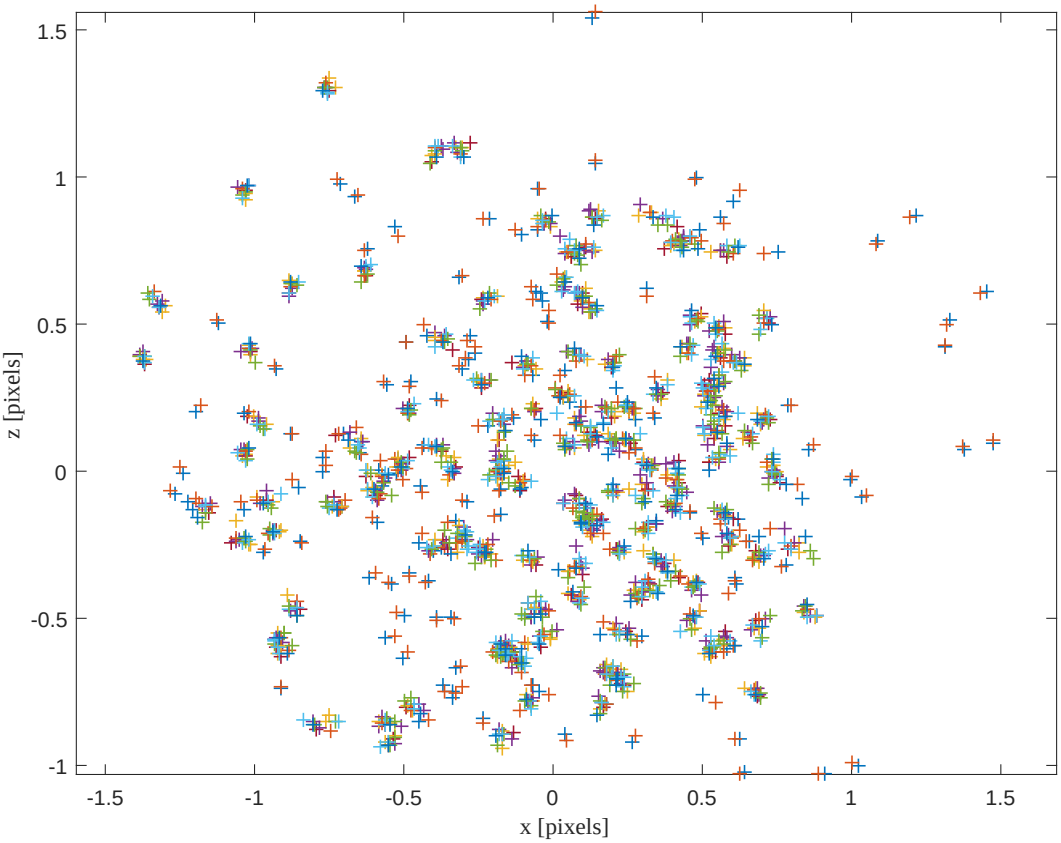


Figure 3.18: Reprojection of errors due lens distortion.

Focal length: [1075.04± 21.14 1228.95± 19.05].

Principal points: [624.34±16.37 468.31± 14.44].

Skew coefficient: [0.00039±0.00018] pixels axes angle, $\beta = 89.976°$.

Radial distortion: [-0.00044±0.000392 -0.00122± 0.00091 0.0001± 0.00006].

Tangential distortion:[0.0001±0.000065 0.0000± 0.0000].

It is seen from the camera parameters that the distortion effects are very small. However, those parameters were used to undistort the video frames in this study so that straight lines in reality correspond to straight lines in the image plane. Figure 3.19 shows an example of raw (distorted) image and undistorted image using the camera parameters. There is very little bow in the distorted image compared to the undistorted image.

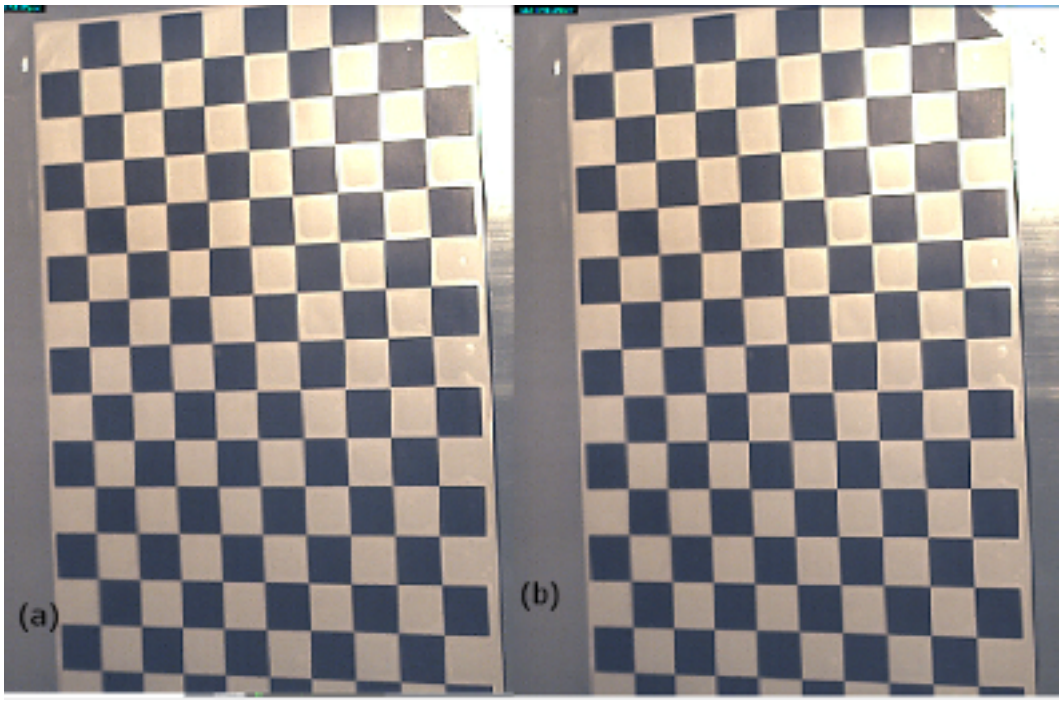


Figure 3.19: Applying camera parameters to undistort images (a) distorted image (b) undistorted image.

3.4.2 Image and data processing system

3.4.2.1 Image acquisition

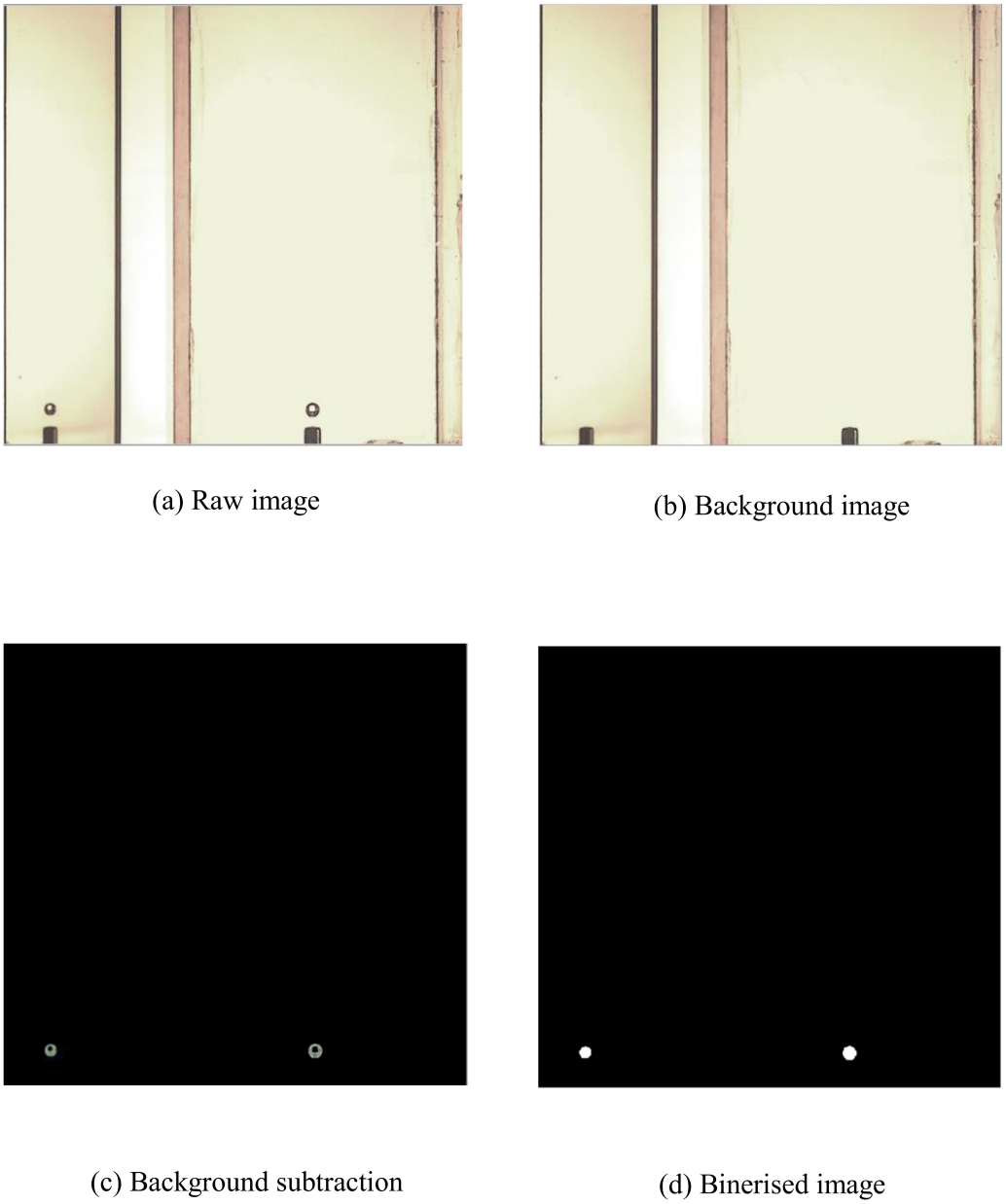
High speed video camera (NAC Hotshot) capable of taking 500 frames per second was used throughout to get bubble information. A Nikon 28-80 mm of the model (f 3.5-5.6 D) was used as a camera lens. The image acquisition system is connected

to a computer by Hotshot link software.

3.4.2.2 Image analysis from experiments

Detailed information of such parameters was analysed by the image processing technique using several routines developed in MATLAB. Detection of the bubbles is carried out by subtracting each frame from a background frame which is selected when the bubble is completely outside the field of view. RGB images are converted into grey-scale images. In order to distinguish the bubbles from the illumination background, a global threshold is then applied automatically based on the method developed by Otsu (1979). The application of the global threshold results in converting the greyscale images to black and white. The threshold level separates the pixels that belong to the bubble from those that belong to the background. It is necessary to have a global threshold for the accuracy of the calculation of bubble parameters such as bubble radius.

Since there are two bubbles (objects) in each frame, they are localised by calling the connectivity parameter of each object as MATLAB labels each object in the image with a unique value (integer value). Figure 3.20a-d summarises the steps that were used to binarise a raw image. Figure 3.20b shows the background image that was subtracted from the raw image in Figure 3.20a, the resulted image is shown in Figure 3.20c. Finally, Figure 3.20d shows the binarised image after the application of the threshold value. Various important parameters can be now retrieved from each object. Those parameters are, for example, the centre of mass and the area of the bubble. Some of the measured parameters using MATLAB



(a) Raw image

(b) Background image

(c) Background subtraction

(d) Binerised image

Figure 3.20: Detection and binerisation two views of single bubble (a) raw image, (b) global background, (c) background subtraction (d) binarised image.

are listed below

Centre of Mass (x_m,y_m): Centre of gravity of x and y coordinates in mm.

Area (A): Area of the bubble in mm^2.

Major and minor axes (a,b): The major and minor axes of the best fitted ellipse in the bubble (Figure 3.21).

Tilt angle (θ): The angle that the major axis creates with the x axis (Figure 3.21).

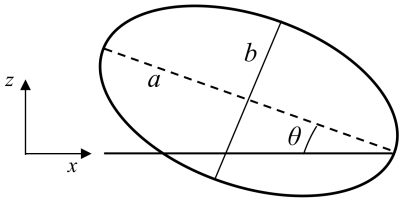


Figure 3.21: Parameters that are measured as a result to an ellipse fit inside a bubble.

It should be noted here that size of the bubble in the mirror view was smaller than that in the direct view. Hence, the deviation in the size of the nozzle in the mirror was continuously calibrated against the nozzle size inside the test section.

3.4.2.3 Parameters from CFD

It is known that the use of the camera has a margin of uncertainty which might be embedded in the unavoidable shadows, inaccurate calibration of pixels to metric ratio, and the spatial resolution associated with the size of the lenses used. Therefore, a novel coupling between CFD codes (Ansys-Fluent) and MATLAB has been adopted here. The basic idea is to export the transient bubble surface directly from Ansys-Fluent as a cloud of points. In the numerical frame, the data is collected from all over the nodes in the computational domain. Then, using MATLAB, to isolate the bubble and configure it from those nodes in the domain, the data is filtered by separating the readable nodes from empty nodes and far away air surface is also excluded using few lines a written MATLAB code.

This exported data is in SI units, thus there is no need to apply any calibration measurements. Then, similar to image analysis, another written MATLAB code (available online) was used to get detailed information in 3D or in 2D by fitting the best ellipse that encloses the non-uniform shape of the bubble. Therefore, the major axis, minor axis and the tilt of the bubble can be easily calculated. Figure 3.22 shows an example of raw data of the air phase exported.

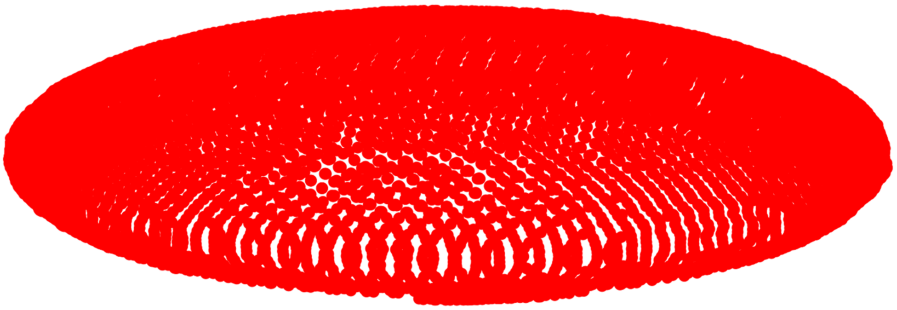


Figure 3.22: Bubble data exported from Ansys-Fluent showing an air bubble represented by a cloud of points.

3.5 Summary

With emphasis on dual bubbles systems, a new dynamic adaptive methodology has been presented here for capturing of bubbles. The computational efforts have been shown to decrease using this approach compared to a fixed grid. An initial ellipsoidal refined region will be constructed to surround the air phase. This region will eventually become more spherical when the bubbles get closer or coalesce and as a result higher computational efficiency is gained. Unlike other techniques, this method has the ability to capture important information from far

field region such as the wake behind the bubbles though an appreciable increase in the total number of elements is experienced. It was demonstrated here that the proposed adaptive region worked well with capturing coalescence events and at different configurations of dual bubble system. A comparison against fixed grid simulation was also made to show the accuracy and the reduction in the total number of cells in using our adaptive modelling method. The marked region responded well to different configurations of bubbles in a way that kept the total size of the mesh significantly low. A tempting conclusion is that this method can be applied with high accuracy to an arbitrary number of bubbles. The new method was also verified by the comparison against the rise of single air bubble in water.

The experimental setup and the procedure in which single and dual bubbles are released were shown. The bubbles were generated using different nozzles fixed in the centre of the rectangular box. The bubbles were released at low frequency in order to reduce the effect of the wake between two consecutive rising bubbles. The data acquisition system using a high speed camera was described. The analysing techniques using MATLAB codes were also discussed in this chapter. In order to increase the accuracy of the measurements, calibration process was done on the high speed camera used.

4

OBSERVATIONS OF SINGLE BUBBLE DYNAMICS

4.1 Introduction

The controversy on single bubble dynamics such as path instability and shape oscillation is still continuous in spite of the huge number of studies that have been done so far. However, the scarcity of numerical analysis on these physical processes is observed. Thus, the current experimental campaign and the previous studies will be considered as the basis to validate the 3D numerical analysis models. By first describing the experimental facility, the next sections will be highlighting the experimental findings of the path and shape instability and the comparison that was carried out between the experiments and the numerical method (VOF method).

4.2 Experimental setup

A rectangular box which was fabricated from Plexiglas was used to investigate single bubble rising in quiescent liquid. The cross-section of the box was 100 $\times$ 100 mm and the height was 500 mm. The release of air bubbles from a set of nozzles located at the centre of the box was accomplished by injecting the

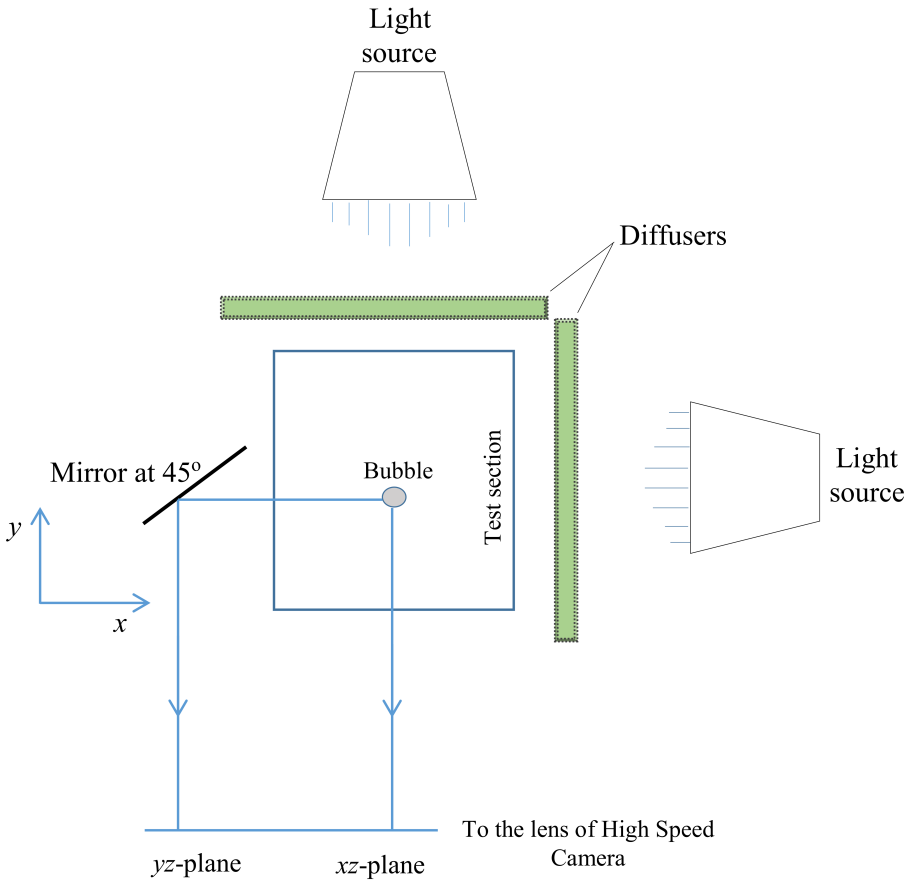


air from the bottom of the column using a syringe pump. The rectangular box was filled with tap water up to 200 mm above the tip of the nozzle. The ambient temperature and the pressure were 21 C° and atmospheric, respectively. Different nozzles were used to generate different sizes of single bubbles. For the smallest size of the bubble released, a glass nozzle with 1.1 mm internal diameter, d_i, was centrally placed. For the medium and the larger bubbles, 2 mm d_i and 5.25 mm d_i were used, respectively.

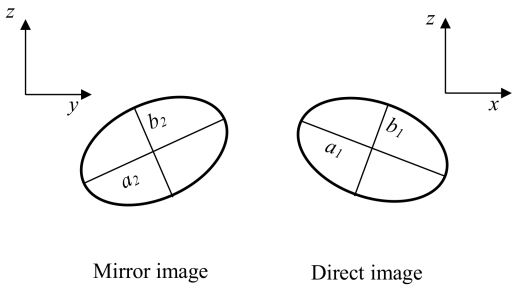
A High Speed Camera (NAC HotShot) capable of taking 500 frames per second was used to capture the bubbles behaviour. In order to get two 2D perpendicular projections of the same bubble simultaneously, a mirror (220 mm× 60 mm), as was suggested by Lunde and Perkins (1998), was positioned at an angle of 45° to the centreline of the camera outside the rig. Therefore, two planes (views) were projected on the lens of the camera that were xz-plane, which was directly from the box to the lens of the camera and yz-plane, which was the reflection of the bubble into the mirror. A schematic diagram of the top view of the test section is depicted in Figure 4.1a.

Because of the use of the mirror, two light sources were used to illuminate the area of recording for both the camera and the mirror. A light diffuser was also placed between each light source and the box to ensure the even distribution of the light inside the box and the mirror views. It is important in the experiment to balance the light sources for the bubble in the column and the mirror because sometimes the light is scattered from the bubble surface while it is wobbling particularly the projection of the bubble in the direct view. Figure 4.1b depicts

the coordinate system and the bubble major, a, and minor, b, axes of the two planes. The size of the nozzle inside the column was used as a reference length to allow for the calibration of the spatial resolution which was in the range of 0.157 mm/pixel.



(a)



(b)

Figure 4.1: Schematic diagram of the test section (a) top view (b) coordinate system and the bubble principal axes of the two planes.

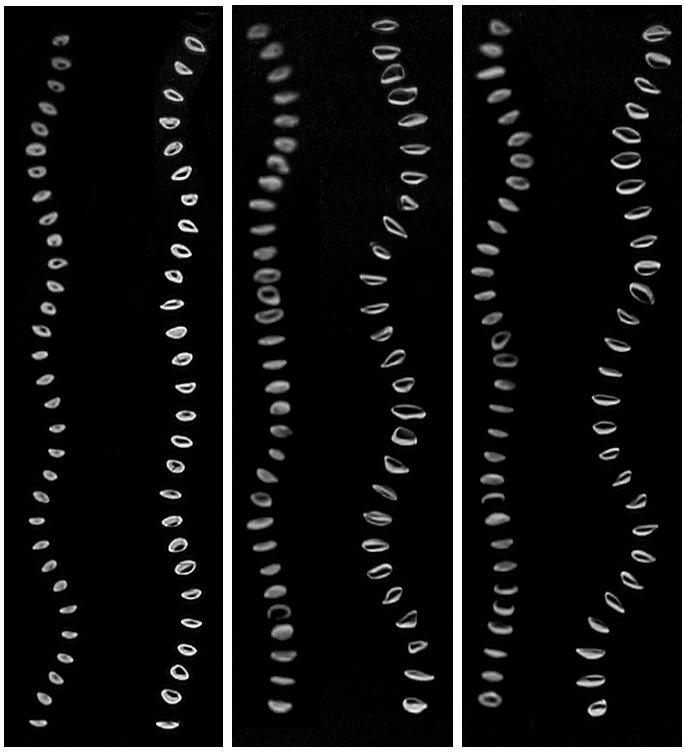
4.3 Experimental path instability and shape oscillation

4.3.1 Path instability

Since the validation of the numerical techniques is one of the goals of this chapter, experiments were carried out to generate bubbles of different sizes. The syringe pump was set at very low flowrate to ensuring releasing the bubbles at low frequency where one bubble would not be affected by the wakes of a leading one when they consecutively travel upward. Three different sizes of bubbles were generated, all clustered around a mean equivalent radius because no two bubbles were exactly the same size. Because of the complex behaviour of each bubble, the experiments were repeated a minimum of 10 times for each bubble size. The average equivalent radius of the collected bubbles, r_{ave}, were 1.6 mm, 2.0 mm and 2.55 mm based on the equivalent volume of a spherical bubble. The maximum deviation of the bubble size was within 10%. Hence, each single run is treated as unique in terms of its own trajectory and shape oscillation.

Figure 4.2 shows the superimposed binary images of three single runs of three classes of bubbles studied. All the bubbles showed in Figure 4.1 had two viewing planes xz and yz. These planes were constructed from the direct and the mirror images.

In depth analysis of the single bubble behaviour, although conducting 10 runs for each bubble size is not statistically large, the time evolution of the behaviour is shown in Figure 4.3a-c. In this figure, three single runs of each bubble class are plotted. It is clear from the figure that each single bubble (run)



(a) (1.605 mm) (b) (2.025 mm) (c) (2.57 mm)

Figure 4.2: Superimposition of bubbles (Δt= 20) ms for the mirror (left) and the direct (right) images.

has its own unique trajectory, i.e., we cannot get bubbles having exactly the same path. This can be attributed to the different boundary conditions, any residual disturbance in the flow due to the previous bubble, and the deviation in the released bubble size even though it is a slight deviation. Also, in Figure 4.3a-c, the bubbles oscillated at different maximum amplitude for each size of the bubbles where it was measured to be 10 mm, 13 mm and 7 mm for r=1.605 mm, 2.025 mm and 2.57 mm respectively. Hence, it should be noted that the smallest bubbles travelled more towards the walls of the box compared to the the larger bubble. Figure 4.3a-c shows also some of the main features for a single bubble travelling upward. For example, all the bubbles started having periods of oscillation of 0.2 s at the first cycle. Thereafter, the periods changed, with the smaller bubbles



seeing a reduction in the period of oscillation. It is more likely that the smaller bubbles are more susceptible to the forces acting on them and therefore responsed (accelerate) more quickly.

Figures 4.4a-b, however, describes the three dimensional behaviour of a single bubble with 1.605 mm equivalent radius. There is a considerable dominance of the zigzag motion in the type of the path oscillation. This zigzag path is sometimes followed by a single short spiral cycle as shown in Figure 4.4b where it is argued that the transition from the zigzag to the helix is possible but not the opposite. Table 4.1 summarises the observed types of motion of the several bubbles studied. This table shows the transition of the motion type from zigzag to helical or vice versa. The results agree with what was previously reported by Ellingsen and Risso (2001) and Saffman (1956) that the zigzag motion can be almost dominant for all classes of bubbles that were investigated here.

Table 4.1: Summary of the motion types for the studied bubble sizes.

	Bubble radius r_{ave} [mm]		
	1.6	2.0	2.55
Number of sampled bubbles	10	10	10
Zigzag to Zigzag	9	9	10
Helical to Helical	0	1	0
Zigzag to Helical	1	0	0
Helical to Zigzag	0	0	0

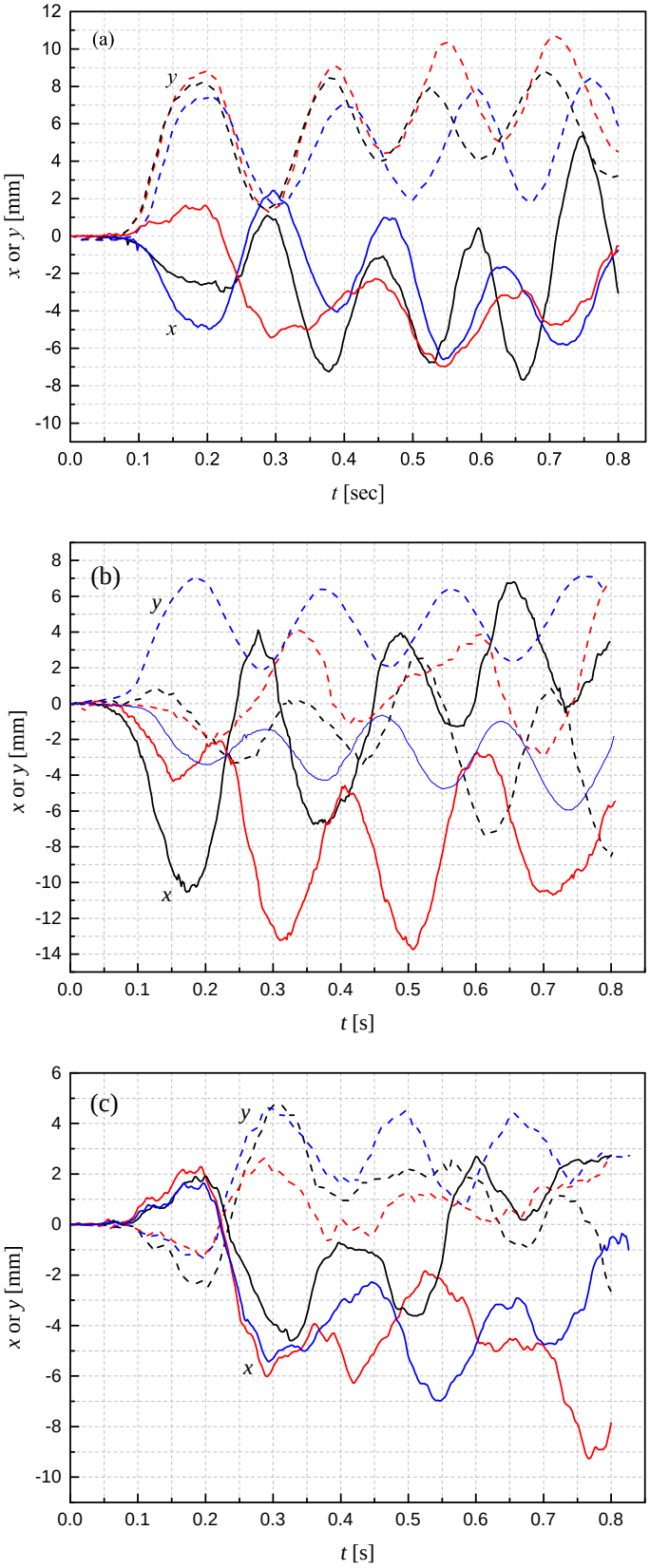


Figure 4.3: Lateral positions of single bubble (a) r=1.605 mm (b) r=2.025 mm (c) r=2.57 mm

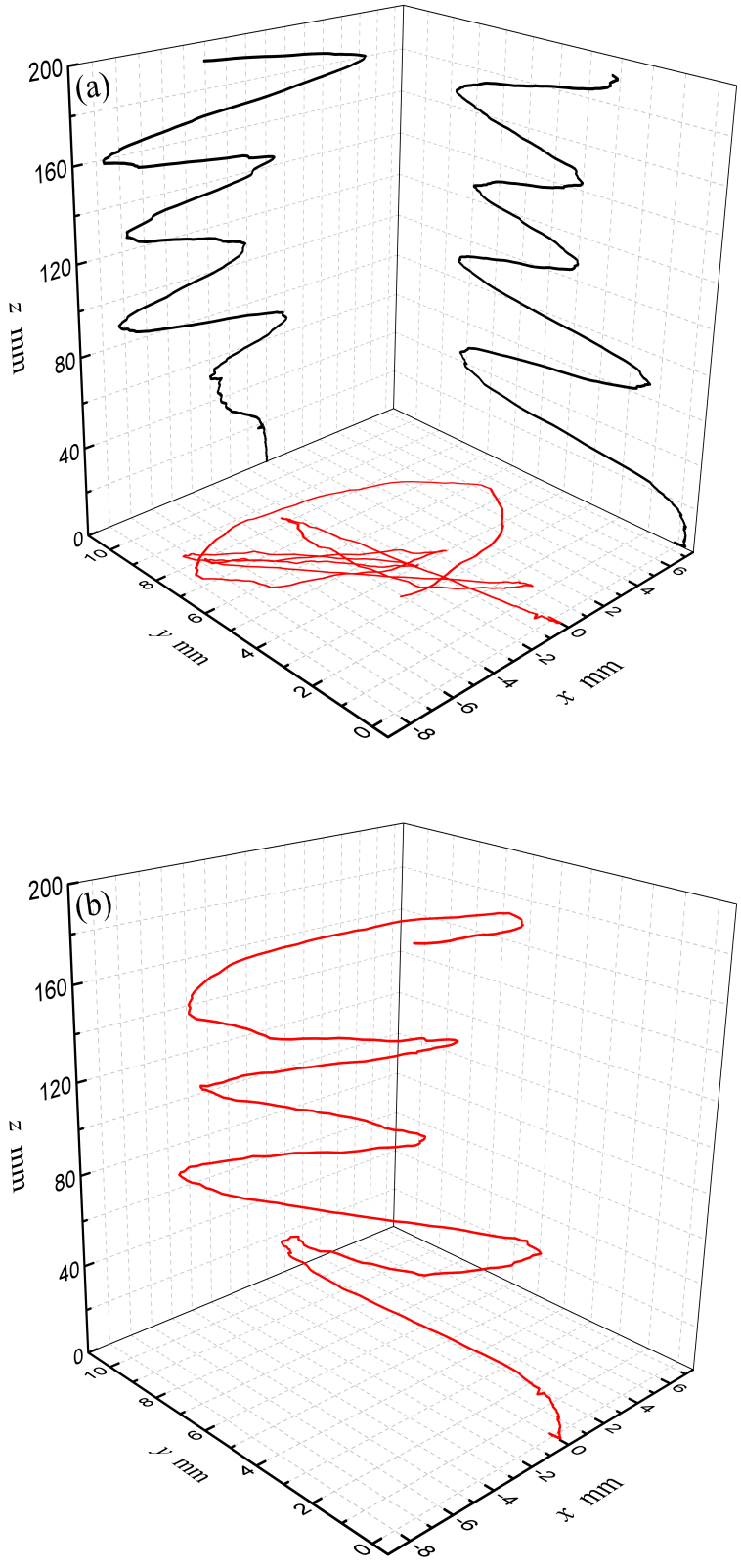


Figure 4.4: Three dimensional behaviour of a single bubble of r=1.605 mm (a) top view of the bubble with its lateral positions (b) 3D bubble behaviour showing the a helical motion near the top surface of the water.

The lateral positions of the x and y directions are shown in Figure 4.5a. The corresponding three components of the bubble velocity u, v and w are illustrated in Figure 4.5b. The three components of the velocity are compatible with the lateral positions. The average rise velocity of the bubble, 254.8 mm/s, is in good agreement with that reported in Clift et al. (1978) for pure water.

4.3.2 Shape oscillation

The transient behaviour of the bubble deformation is presented in Figure 4.6. The features presented in this figure are for a bubble with r of 1.605 mm. It was chosen as it shows the required details with moderate amplitude and frequency compared to a larger bubble. It is clear from the four principal axes how the bubble oscillates and the axes from both the direct and mirror view are consistent so that if one axis increases the other decreases. For the major axes, it is highlighted that they exhibit different behaviour compared to the minor axes. There are small to medium amplitudes and high frequency oscillations. However, for minor axes, these transitions illustrated larger enough amplitude and low frequency compared to that of the major axes. The ratio of major to major and minor to minor axes were calculated in Figure 4.7. The time series of these ratios showed nearly a distinct frequency of oscillation for the major axes ratios. While irregular oscillations were noticeable for the minor axes ratios. This could be due to the argument that the bubble is oriented by its minor axis around which the ellipsoidal bubble is rotating.

Another important factor describing the kinematics of the bubble is the orien-

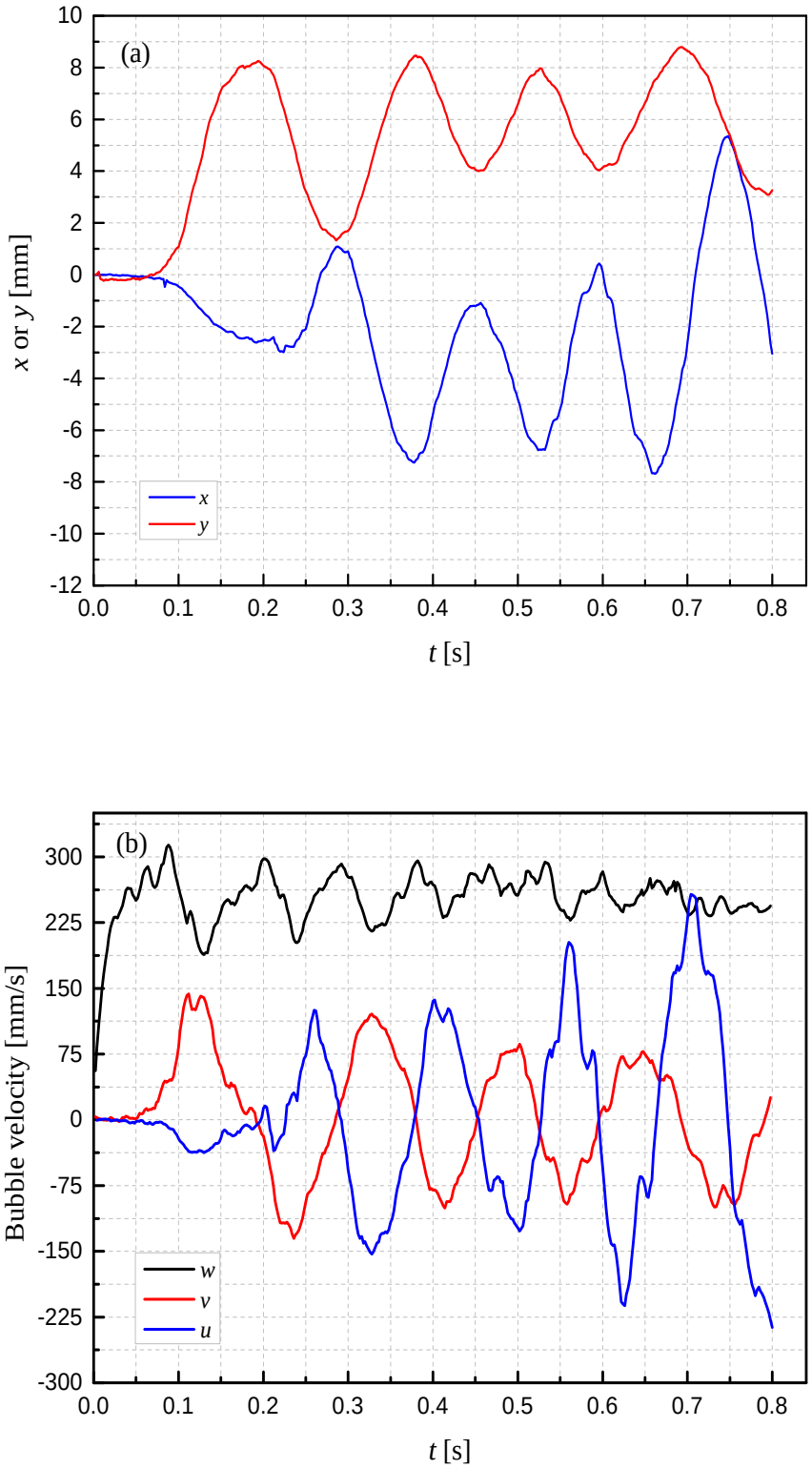


Figure 4.5: Experimental bubble-centroids and velocity for the 1.605 mm bubble (a) transverse migration in x and y positions (b) the three components of bubble velocity u, v and w.

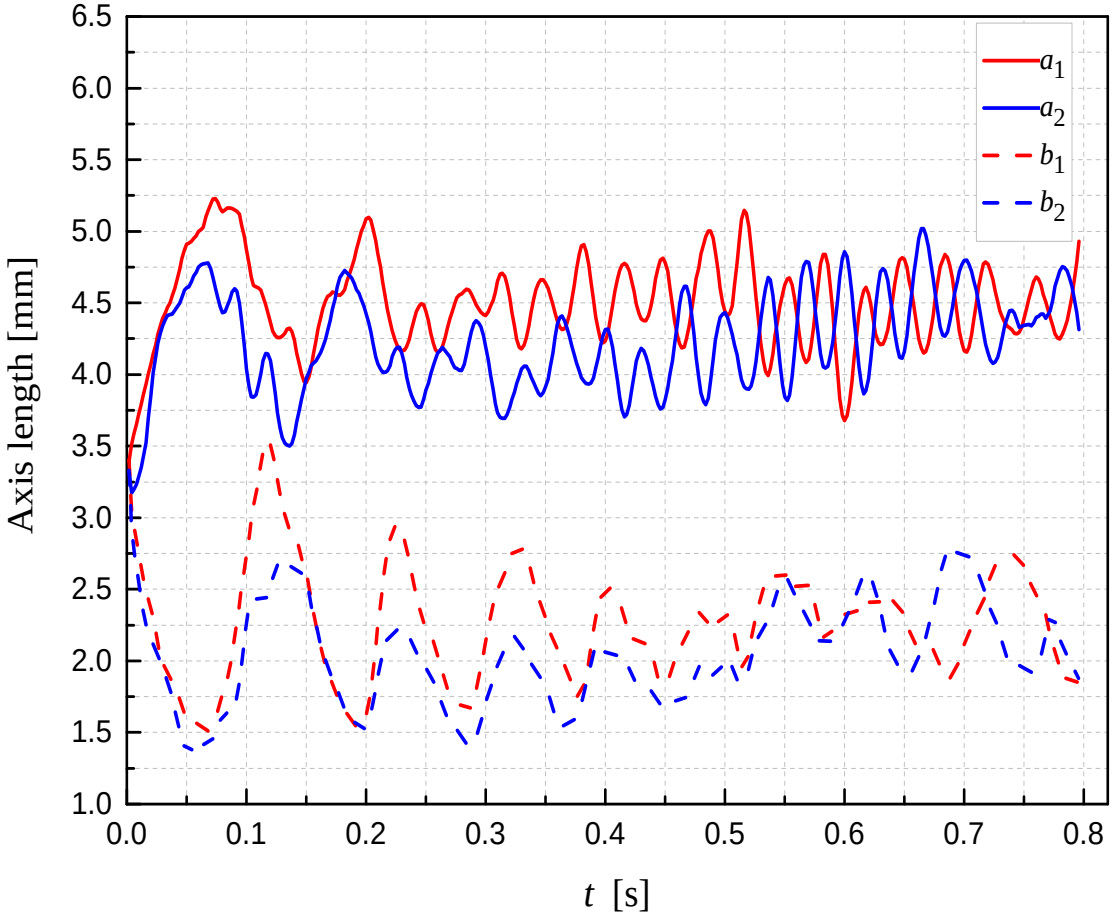


Figure 4.6: Principal axes of bubble with time for an experimental run of r=1.605 mm. a_1 bubble major length captured directly from the camera, b_1 minor axis measured from the camera, a_2 bubble major axis measured from the mirror, b_2 minor axis measured from the mirror.

tation of the bubble as the bubble is not just wobbling in the x or the y direction but tilting as well. As the bubble rises, it is clear from Figure 4.8b that both bubbles (1.605 mm and 2.57 mm) travelled for direct short distance and then they tilted nearly at the same magnitude which was between 30° and -30°.

Bubbles of intermediate sizes can be described by an ellipsoidal shape (spheroid) on average. For the accuracy reasons, the transitional shape of the bubble, however, has not been characterised by a certain shape. Therefore, aspect ratio, AR, contraction/expansion of the major/minor axes, is a good way to describe the

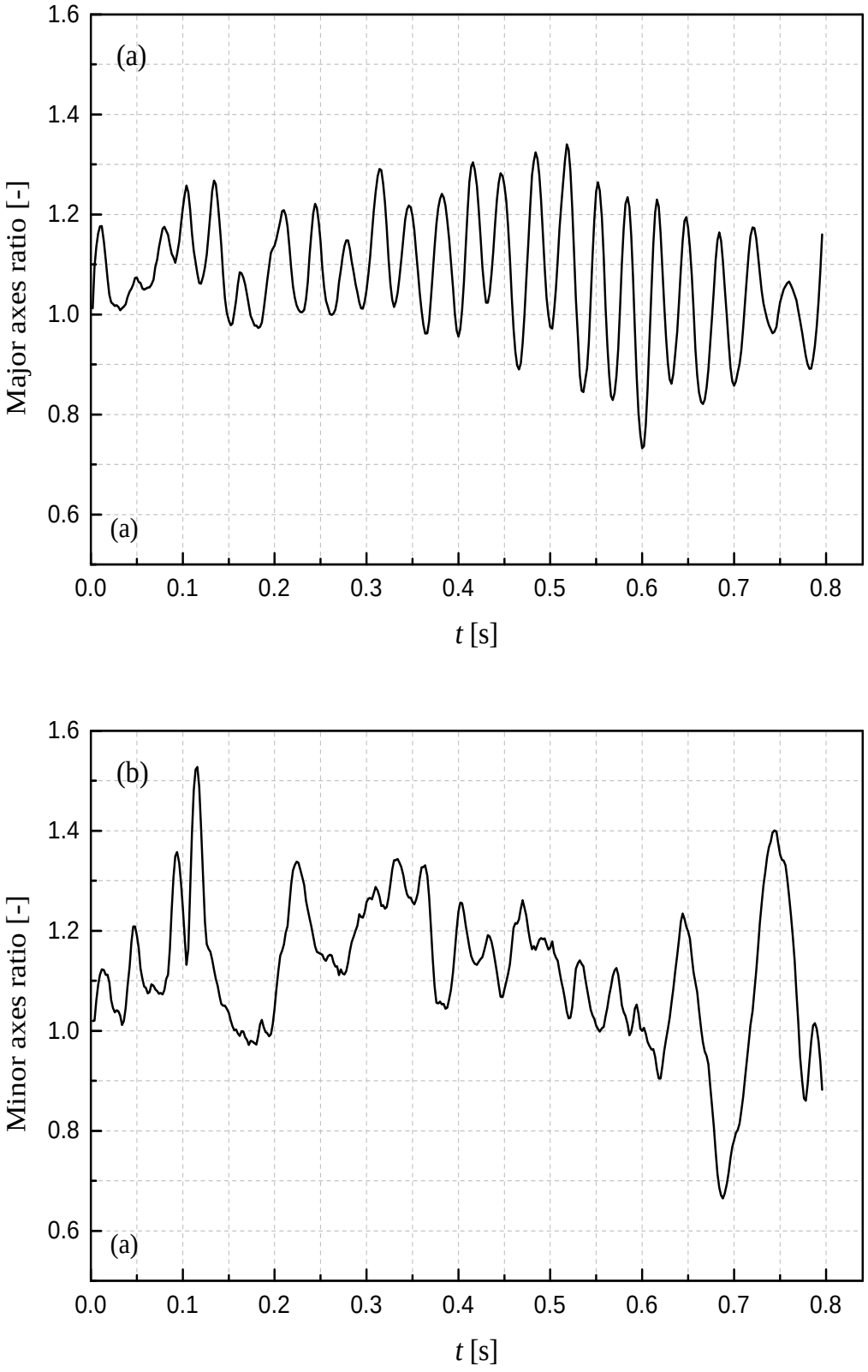


Figure 4.7: Experimental time evolution of bubble major axes ratio for r=1.605 mm.

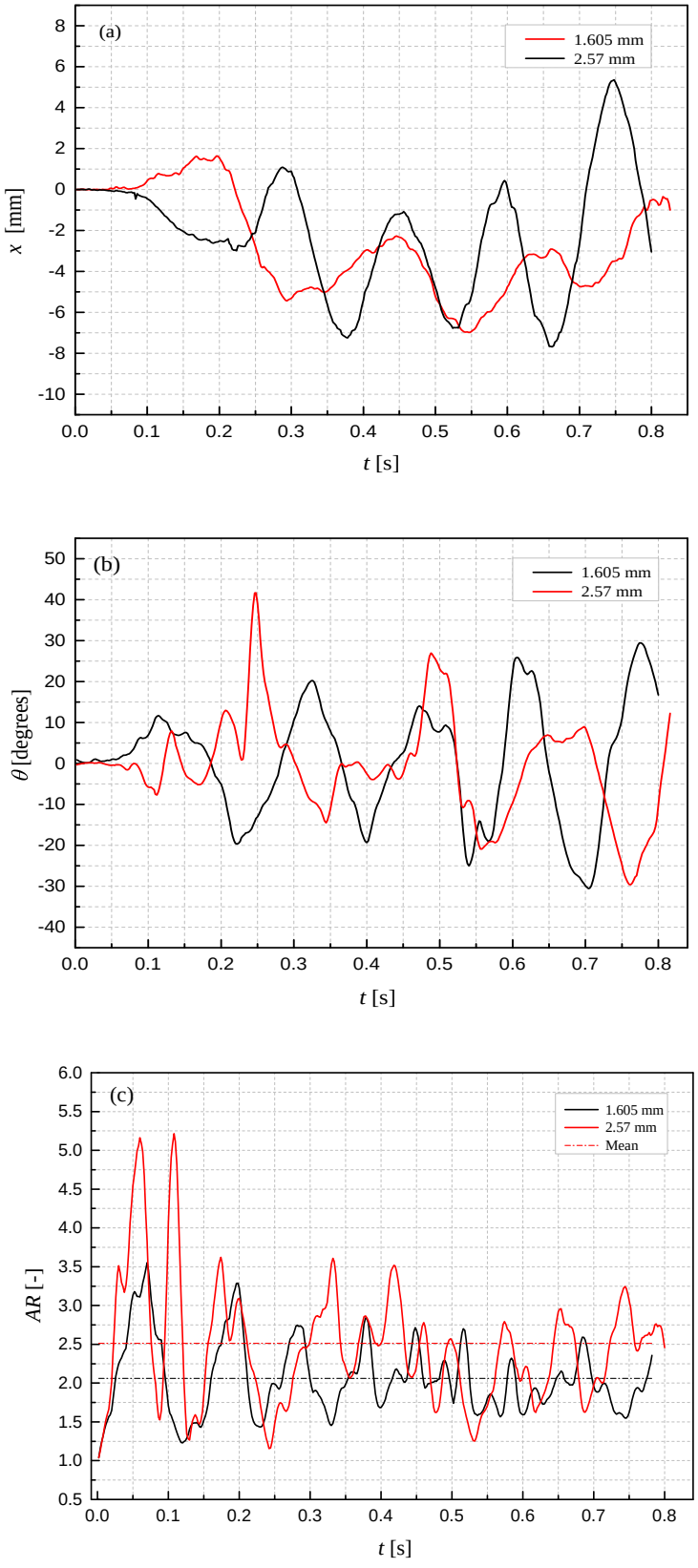


Figure 4.8: Comparison for the experimental results of the 1.605 bubble against the 2.57 mm bubble (a) position of centroids (b) tilt angle (c) aspect ratio.

overall bubble shape oscillation. Since the aspect ratio can only be represented by 2D plane, the xz-plane (direct image) was chosen to be analysed here as an example. The periodic behaviour is the main feature of the aspect ratio of both bubbles as compared in Figure 4.8c. At a ratio of value close to 1, both bubbles started their shape deformation which belongs to a circle. They increased to the highest level and then both bubbles periodically declined and wobbled at a mean value of 2.05 for the 1.605 mm and 2.5 for the 2.57 mm. Unlike the 1.605 mm bubble, it is observed that the 2.57 mm bubble oscillates differently and they exhibited a peak-to-trough amplitude of oscillation. A probable reason for that might be the uneven frequencies that result from the superposition of variety of fluctuation modes during the movement of the bubble surface and at different amplitudes (Fan and Tsuchiya, 1990).

4.4 Comparison of the experimental and the numerical observations

All the numerical simulations are performed in a 3D domain. The Navier-Stokes equations are discretised using the Finite Volume Method (FVM). The SIMPLE algorithm is used to couple the pressure with the velocity. Geo-Reconstruct is used as the volume fraction capturing scheme, which gives a sharp interface, not smeared like many other interface reconstruction techniques give. The Geo-Reconstruct method is explicit and so the Courant number is kept, for all the cases, to be less than 1 necessitating very small time steps. Since fine grid (0.093 mm) and multiple levels of refinement are used, 15 inner iterations were enough to reach the convergence target while in most cases the convergence was

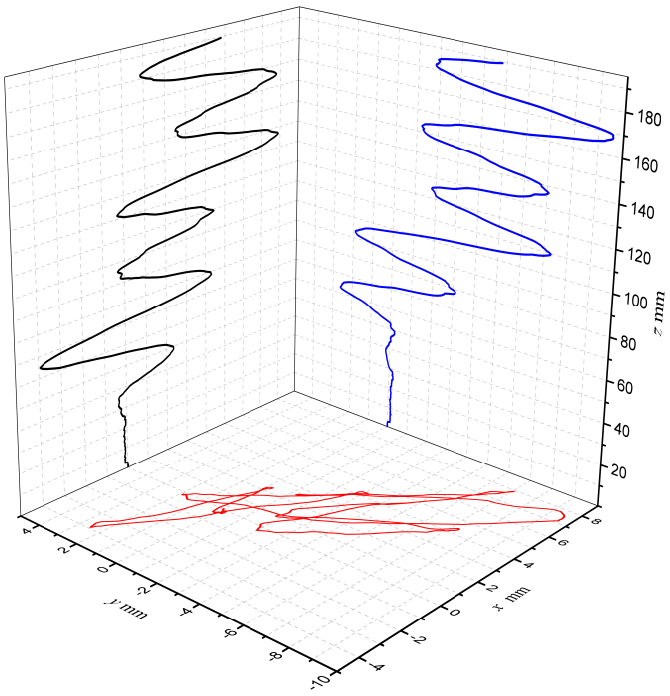
reached in just 10 iterations.

The following initial and boundary conditions were made to simplify the calculations. A rectangular box is filled with stagnant water, by setting the value of α_l to 1 throughout the domain. A single spherical bubble at rest was placed in the centre of the computational box. This is done by marking those cells inside the bubble and setting α_l to zero there. The velocity gradient at the walls is included by setting up no-slip boundary condition. A free surface boundary condition was used at the top of the domain by patching in a region whose volume fraction of air was 1 above the water.

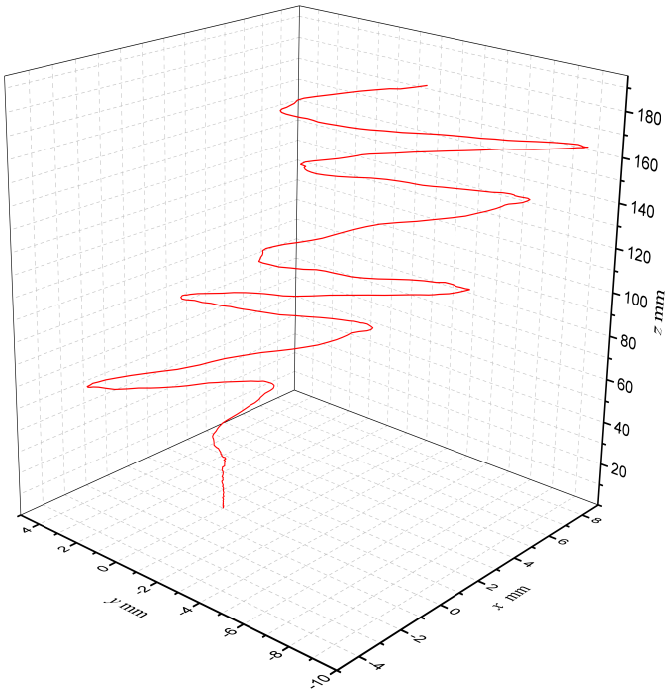
We realise that there is a great spread of results for different experimental bubbles, but not for numerical bubbles, which would follow the same path with the same initial and boundary conditions. Hence, we are making general comparisons between two instances of bubbles that were nearly the same size, released in different ways, an experimental single run and numerical single run.

It can be seen in general that the numerical solution supports the experiments and the studies in the literature regarding a zigzag motion is the dominant path for the bubble size studied here as depicted in the 3D presentation of the axes in Figure 4.9a-b. It is also observable from the x and y positions that the transverse migration of the simulated bubble started a little later because of the non-physical release method in the numerical model compared with the release from the needle in the experiments.

In Figure 4.10a, the simulated bubble oscillated with a period 0.2 s while the experimental bubble started with a period of 0.1 s. The centroids of the bubbles



(a)



(b)

Figure 4.9: Trajectories predicted by the numerical simulation for the 1.605 mm bubble (a) trajectories in 2D planes (b) 3D trajectory of the bubble.

are also clearly seen sometimes running out of phase. This is because they were running on different modes of oscillation. Afterwards, they met at short time and then the experimental bubble preceded the simulated bubble. In Figure 4.10b, a comparison between the orientation of the bubble from the simulations and the experiments is shown. Regarding the amplitude of the tilt oscillation, there was a considerable difference that can be noticed between the CFD approach and the experiments. The fluctuation of the orientation of the bubble in the experiment followed the same oscillations of the trajectory path in Figure 4.10a. While this is not the case for the simulated bubble.

For the aspect ratio comparison shown in Figure 4.10c, the deformation in shape captured by the VOF method was in good agreement with the experiments at the start of the deformation, i.e., both reached the ultimate extent of deformation that is 3.5. Then, sudden discrepancy of about 10 % on average occurred so that the VOF method introduced always higher deformation. As a result, the simulated bubble is expected to experience higher form drag while it rises up. It should be mentioned that part of the error associated with the measurements of the aspect ratio could be the difficulty in ignoring the orientation of the bubble within the measurements.

The dynamics of the simulated bubble in yz direction is also depicted in Figure 4.11a-c. The comparison that was made in Figure 4.10c and Figure 4.11c with respect to the aspect ratio in the xz and the yz planes showed a slight increase in the deformation of the simulated bubble compared to the experiments. The different shape might result in different heat and mass transfer rates.

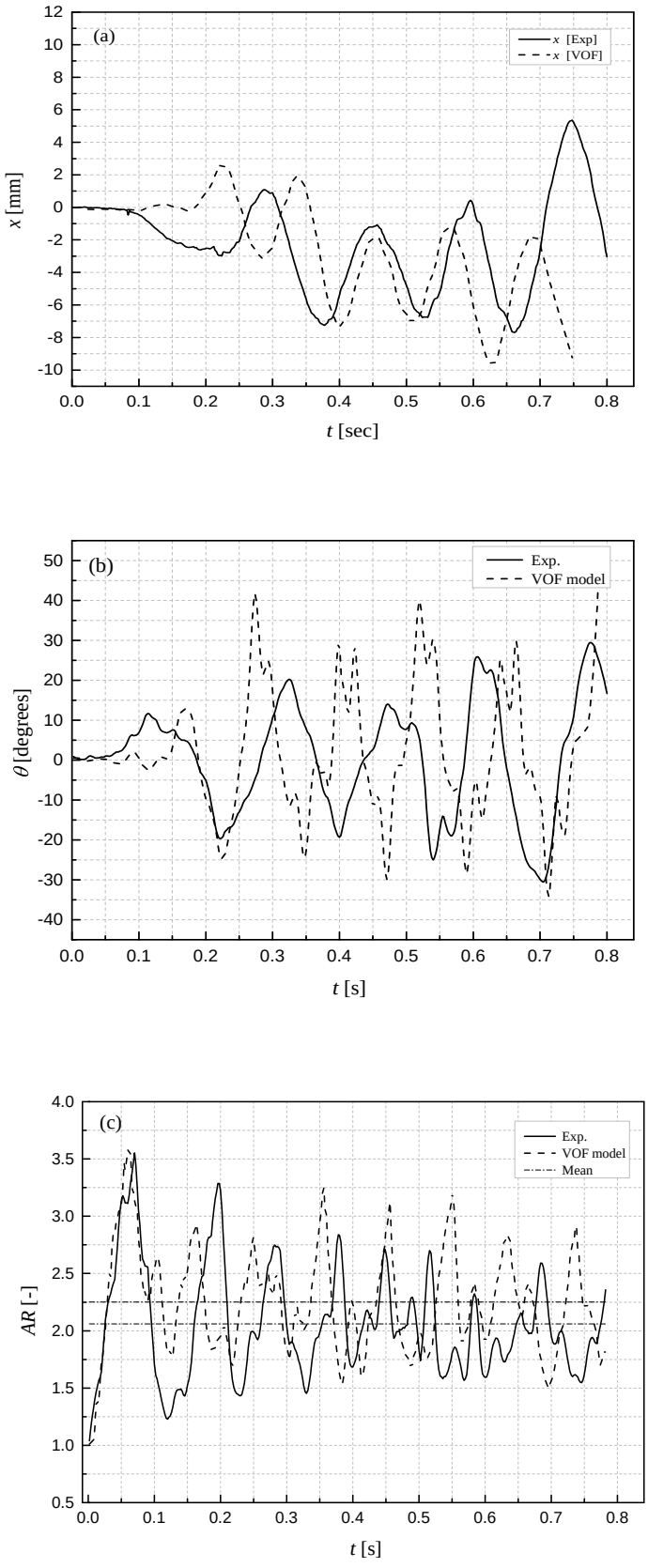


Figure 4.10: Comparison between the experimental and the numerical methods for r=1.605 mm in the x-plane (a) lateral positions (b) orientation of the bubble along the path (c) aspect ratio of the major and the minor axes.

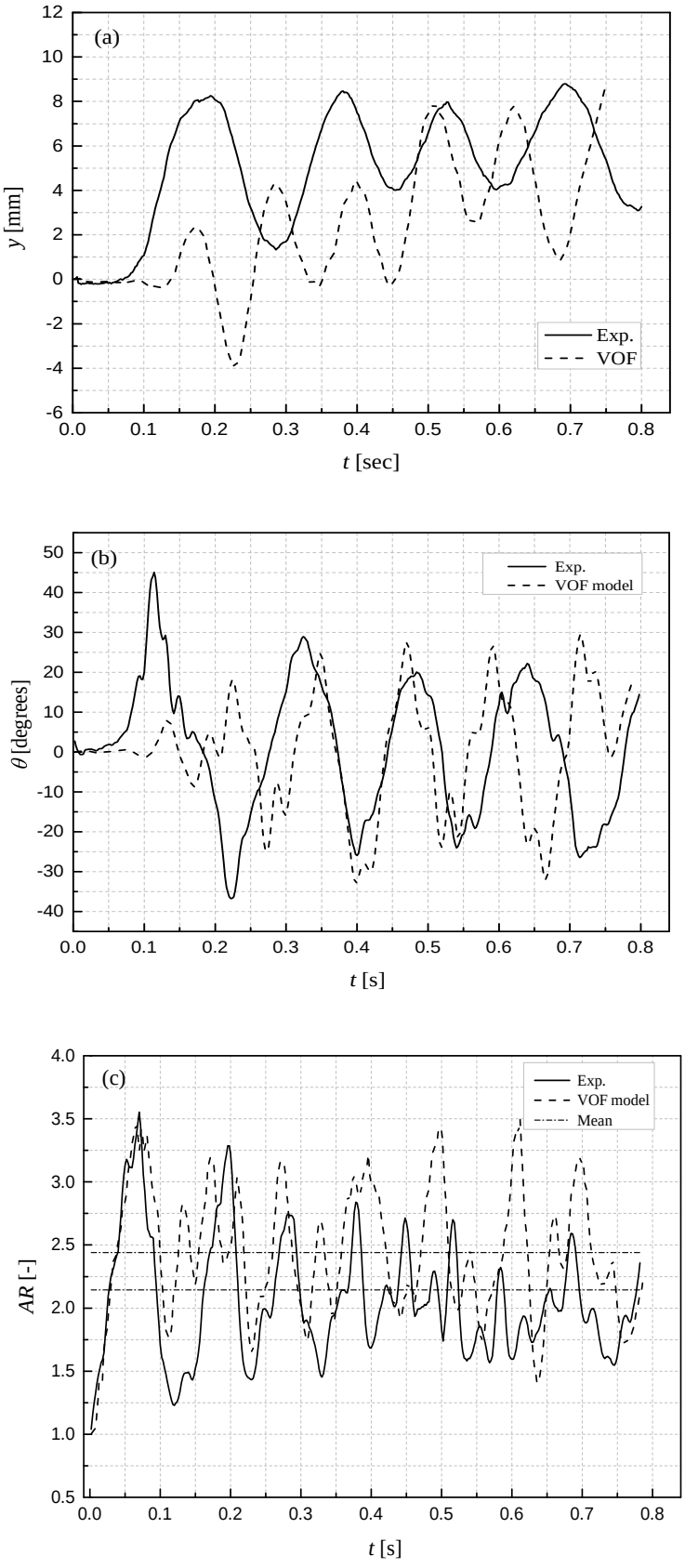


Figure 4.11: Comparison for the results of the VOF method with the experiments in the y-plane (a) positions of centroid (b) tilt angle (c) aspect ratio.

4.5 FFT analysis of the bubble dynamics

In order to check the validity of the CFD codes against the experiments along the whole time period, the frequencies of the important parameters are investigated here as can be seen Figure 4.12. Fast Fourier Transform (FFT) was used here. The number of data points used was 400 and the sampling rate was 500 Hz. The Normalised Power Spectrum (NPS) of the data is computed for important parameters. The NPS can be defined as

$$\mathrm{NPS}=\frac{\mathrm{FFT}[f(t)]\overline{\mathrm{FFT}[f(t)]}}{\langle \mathrm{FFT}[f(t)]\overline{\mathrm{FFT}[f(t)]}\rangle},$$

where FFT indicates the fast fourier transform, the overbar is a complex conjugate and $\langle\,\rangle$ is an average.

The bubble travelling time and the characteristics of the shape are significantly influenced by different frequencies of oscillation. The experimental frequency of orientation, tilt, oscillated at 5.62 Hz which is the same frequency of the bubble path in the x-direction. In addition, the frequency of the minor axes ratio is 11.3 Hz where it is clearly seen that it is double the frequency the bubble kinetics (the path and the orientation). Furthermore, it seems that the shape oscillation nearly has the same frequency as the bubble rise velocity which is again nearly twice the frequency of the bubble trajectory. That was previously noticed by the experiments of Lunde and Perkins (1998). These frequencies were noticed for all of the runs and for the different classes of bubbles studied. A summary of the mean results for all three bubble sizes studied is presented in Table 4.2.

On the other hand, the VOF method failed to capture the same oscillation

Table 4.2: Summary of the average results for the bubble sizes studied here.

	Bubble radius r_{ave} [mm]		
	1.6	2.0	2.55
Average major axis [mm]	4.31	5.64	6.86
Average aspect ratio [-]	2.04	2.27	2.53
Average velocity [mm/s]	258.1	237.7	228.3
Reynolds number [-]	824	972	1191
Frequency of bubble tilt [Hz]	5.64	4.37	3.61
Frequency of shape oscillation[Hz]	11.32	8.69	7.32
Frequency of bubble motion [Hz]	11.6	8.08	6.86

patterns in the experiments. The orientation of the bubble using the VOF method fluctuated at a higher frequency of 7.61 Hz. Also, there is not such a clear relationship between the shape oscillation or the motion and the path oscillation, as the latter should fluctuate at a frequency half of the former. Thus, the VOF method could lead to behaviour different from that for the experiments. This different behaviour, in turn, makes the bubble in CFD code having different shape and consequently it might affect the hydrodynamic parameters such as the drag experienced by the bubble. These small details constitute the basis to understand how valid are the numerical techniques in achieving accurate calculations, particularly in the three dimensions, whereby the computational techniques are considered as a promising tool of design to reduce the cost of the experiments. The study of the bubble oscillation is important because it is thought that they may contribute to the interaction of two bubbles or more especially at high Reynolds numbers as

will be discussed in detail in the next chapters.

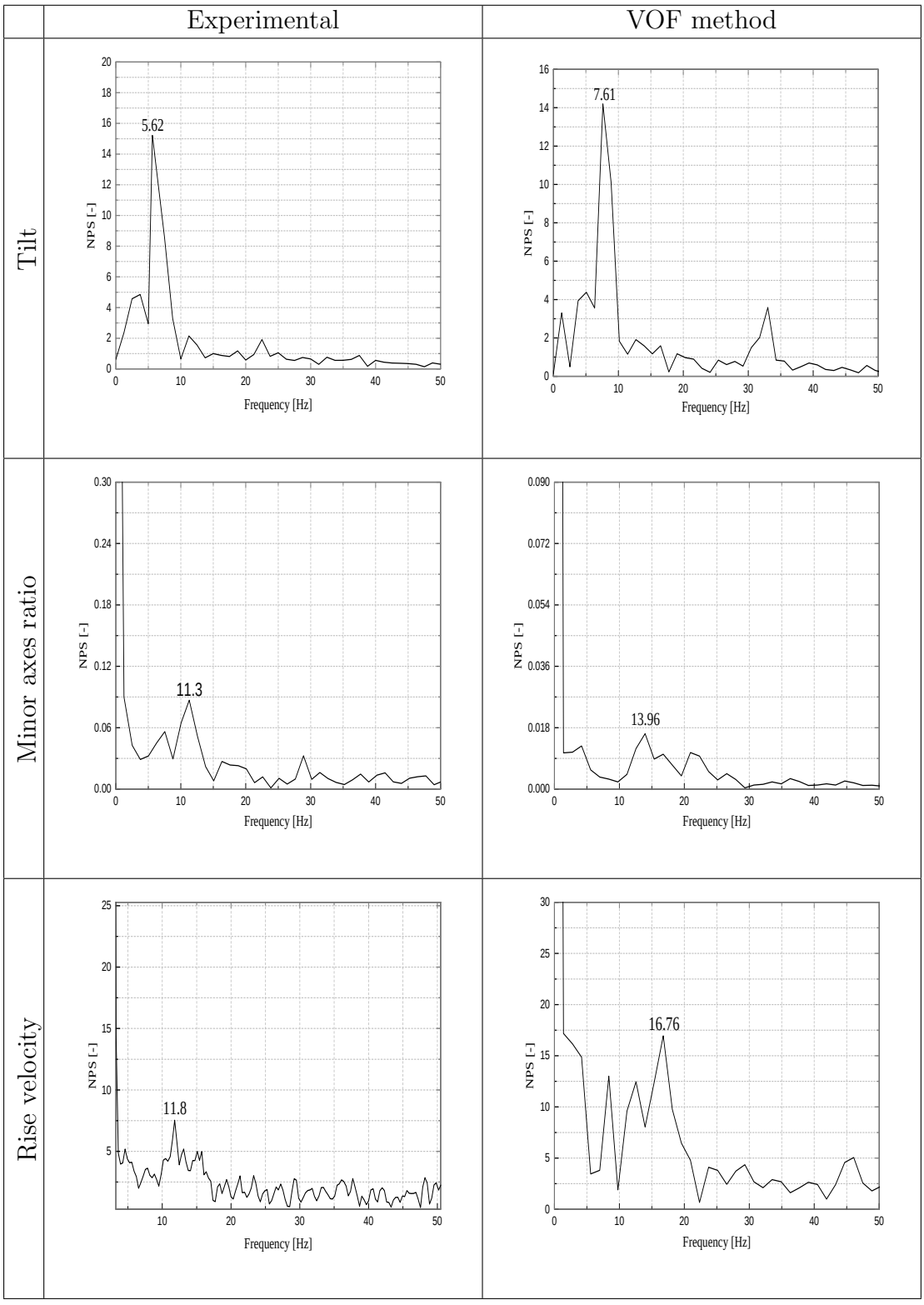


Figure 4.12: Comparison of the FFT analysis for the experiments with the VOF method.

4.6 Summary

The study of the single bubble behaviour is considered useful for many reasons. One of them is to improving the general understanding of the bubble dynamics and its shape oscillation. It is thought that the shape oscillation plays an important role in deciding the bubble dynamics including, for example, bubble trajectory and bubble motion. These effects were studied here experimentally and numerically in 3D for three sizes of bubbles. The measurements confirmed the dominance of the zigzag path for all of the bubbles of the size range studied here. The smaller bubble showed a late initiation of oscillation compared to the larger bubble. The larger bubble, however, had the higher frequency of oscillation. It has been experimentally established that there is a link between the shape oscillation and the rise velocity of the bubble. This was clear when the frequencies of both dynamics were identical. That was observed for all of the experimental runs of the bubble sizes studied. However, this kind of interaction has not been seen in the VOF method. In addition, the CFD code has overestimated the other different parameters such as the shape deformation and the kinetics of the bubble. Overall, the VOF method over predicted the experiments by about 30%.

5

INTERACTION OF BUBBLE PAIRS AT LARGE SEPARATION DISTANCES

5.1 Introduction

The experimental and the numerical evidence in the previous studies for bubble-bubble interaction, especially for deformable bubbles, are lacking. They have been mostly focused on spherical bubbles at low Reynolds number ($\mathrm{Re} \leq 200$). Hence, in this chapter, an attempt to get insight into the bubble-bubble interaction when the bubbles are no longer spherical is provided. The bubbles studied here have Reynolds number, $\mathrm{Re} \simeq 950$. The bubbles at this range of Reynolds number deform seemingly at random and have complicated interactions due to the complex hydrodynamics of bubbles of these larger radii.

In order to cover that gap, a considerable number of experiments in addition to numerical simulations were conducted. This chapter also presents a justification of the numerical simulations against the experiments.

5.2 Experimental materials and procedure

The same test section that was described in Chapter 3 is used to generate pairs of bubbles. This is achieved by placing two stainless steel nozzles side by side at the centre of the box. The nozzles were fixed into a brass base that was

designed so that the nozzles to be removed independently in such a way that many axial separation, $\triangle x$, and as a result different centre to centre separation, s, between the bubbles could be achieved. The internal diameter of each nozzle, d_i is 2 mm, which produced bubbles at about 2 mm equivalent radius, r. The air is pumped through each nozzle using a separate syringe pump of the same model with relatively low flowrate to reduce background perturbations induced by the wakes of a rising series of bubbles. Stagnant tap water was used here as a liquid phase. The experiments were carried out at room temperature ($\approx 21\,^{\circ}C$) and at atmospheric pressure. In order to track the interaction between the bubbles in three dimensions, a mirror having the same specification that was previously described in Section 3.2 is used here.

The bubbles were allowed to rise freely beyond control environment (controlled experiments) in order to mimic the real industrial situation regarding getting two bubbles with different sizes. As a result, the equivalent radii of the bubbles produced deviated at most by 10%. The bubbles are also accordingly produced having different initial configurations (an offset in both vertical and horizontal directions, i.e, ($0^{\circ} < \theta < 90^{\circ}$) and sometimes they rise side by side (θ=0°). Bubble pairs were recorded using a high-speed video camera (NAC HotShot) with 500 frames per second. The water level was 200 mm above the tip of the nozzles. The recorded height was 180 mm which left us with a spatial resolution of 0.15-0.142 mm/pixel. The non-dimensionalised initial axial separations, $\triangle x$, normalised by the average bubble radius, r_{ave}, were 4 and 4.5 and a considerable number of measurements were collected (216 and 203 of data points for each

nozzle gap respectively). This provides a significant database to generate bubble-bubble interaction statistics. Bubble pairs that rise at an offset were isolated and then placed into different categories depending on their initial vertical separation distance, $\triangle z$, normalised by the average bubble radius, r_{ave}. Based on that, the centre to centre separation distance, s, in this chapter entirely lies in the range of $4.2 < s < 11$. Accordingly, the initial relative angle of configuration, θ_i, was $20° < \theta_i < 65°$. Figure 5.1 shows the configuration of the bubbles and the non-dimensional distances.

Depending on our experimental setup, two bubbles with appreciable deviation in radii are generated. The leading bubble, B_1, the first generated bubble, on occasion, assumes an ellipsoidal shape even before the second bubble, B_2, trailing bubble, is released. $s = \frac{2\sqrt{(\triangle x)^2+(\triangle z)^2}}{r_1+r_2}$, $\theta_i = \tan^{-1}\left(\frac{\triangle z}{\triangle x}\right)$, $\mathrm{Re}_{ave}=\frac{\rho_l|w_1 r_1+w_2 r_2|}{\mu_l}$.

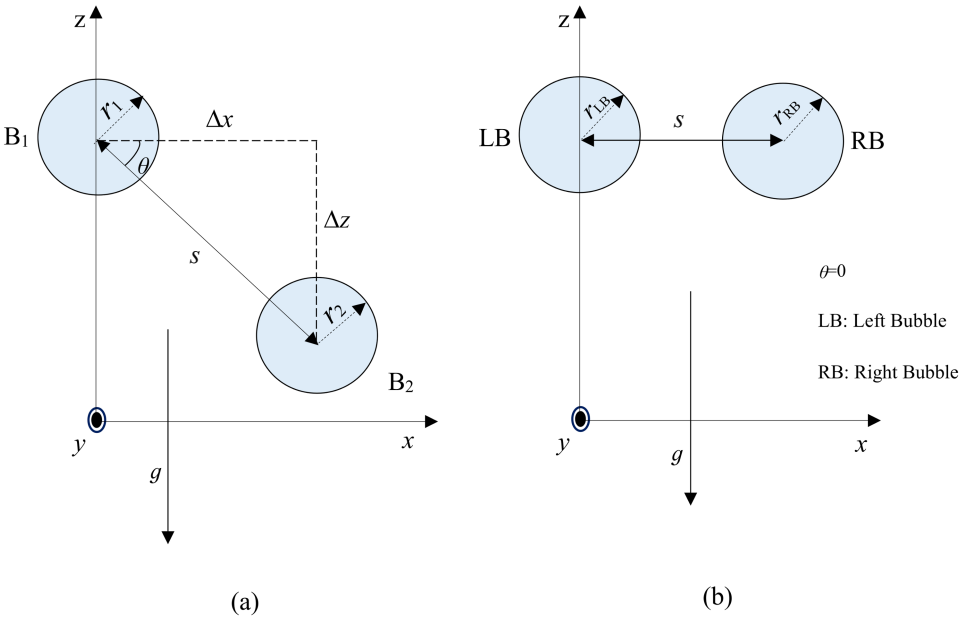


Figure 5.1: Relative configurations and coordinate system of bubble pair rising (a) bubbles rising at an offset, (b) bubbles rising side by side.

Detailed information of such parameters and the transient behaviour of the

bubbles were analysed using a code developed employing image processing technique in MATLAB. Detection of the bubbles in captured images is carried out by subtracting each frame from a background frame which is selected when the bubble is completely left the range of recording. RGB images are converted to grey-scale images. A global threshold of Otsu (1979) is then applied to binarise the greyscale images. Since there are four bubbles (objects) in each frame, they are localised by calling the connectivity parameter of each object as MATLAB labels each object in the image with a unique value (integer value). Figure 5.2a-c shows a raw image that was processed to get a binary image. Figure 5.2c shows the bubbles having different colours as they were differently labelled. Various important parameters can be now retrieved from each object.

In order to calculate the initial size of each bubble, the bubble rises initially with nearly a spherical shape after the release, the images captured immediately after the release were considered. The bubble at that stage is nearly spherical, allowing the estimate of major and minor axes. The length of the major and minor axes will then be averaged to get the bubble diameter. The centre of mass and the area of each bubble are also extracted. The error in the measurements is one pixel that is equivalent to 0.15-0.142 mm. The error measurements are available in Appendix A.

5.3 Hydrodynamic interaction of rising of bubbles

In this section, the problem of the bubble-bubble interaction at large separation distances is addressed. In general, the rising bubbles take different configurations



(a) Raw image (b) Global background (c) Binerized image

Figure 5.2: Detection and binarisation of pair of bubbles (a) raw image, (b) global background, (c) binarised image.

while they rise such as in-line, side by side or having an offset between their horizontal and vertical axes. However, the bubbles having an offset is considered the most likely configuration of rising bubble. Thus, this configuration of bubbles will be first presented. Then, the rising of bubbles side by side will be described.

5.3.1 A pair of bubbles rising with offset

First, the rise of a pair of air bubbles in tap water was experimentally studied. Bubble pairs had axes offset while they rose. Typical motion of a pair of bubbles is shown in Figure 5.3. The figure shows that the trailing bubble approached the leading bubble and collided with it. The influence of wake of the leading bubble is considered to be the cause of the collision. However, the pair did not coalesce and therefore the trailing bubble was repelled even though they collided in both views (xz and yz) as shown in Figure 5.3. This could be attributed to the insufficient time for the complete drainage of the film between the bubbles, which could be a result of the oscillation of the bubbles surface that was earlier discussed in Chapter 4.

Figure 5.4 shows the instantaneous vertical velocity of the pair of the bubbles in Figure 5.3 against the non-dimensional centre to centre distance between the



Figure 5.3: Typical motion of a pair of bubbles with offset axes.

bubbles, s. The initial centre to centre separation distance, s, in this figure is 6.6. It is important here to highlight the effect of the interaction between the

bubbles on their rise velocities. When the trailing bubble rises in the proximity of the leading bubble, near the wake, it begins to accelerate. Sharp increase in the rise velocity of the trailing bubble is seen when the separation distance, s, is close to 2.

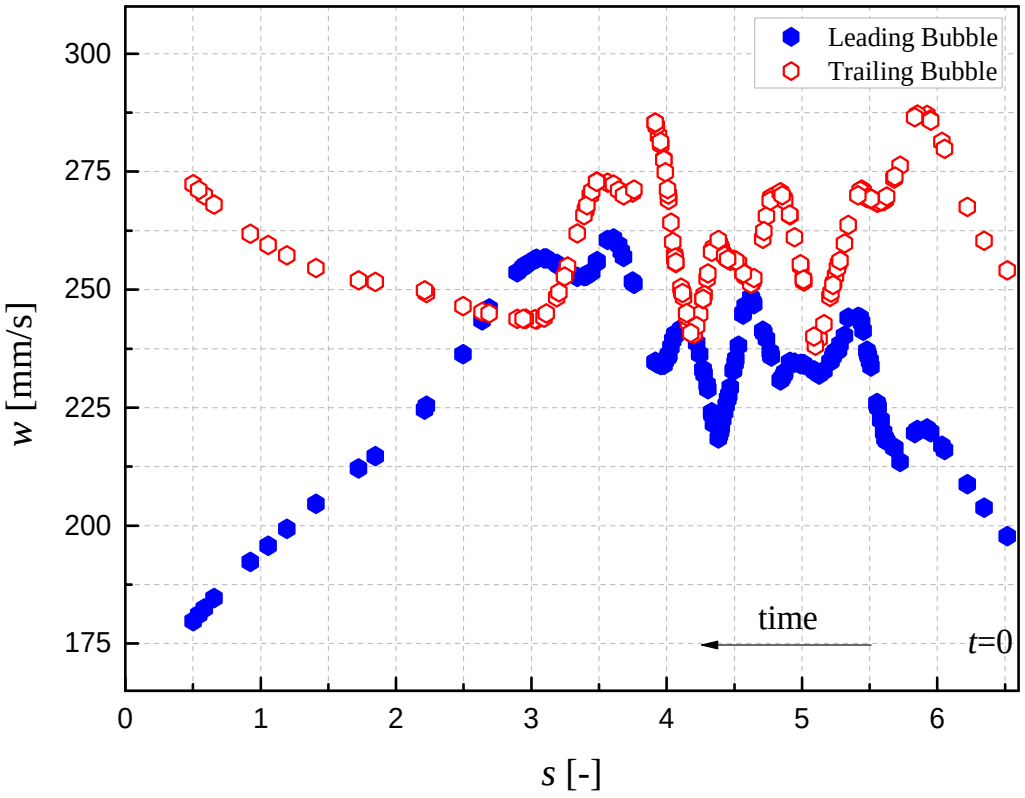


Figure 5.4: Bubble-bubble interaction effects on the vertical rise velocities of pair of bubbles (s=6.6, r_1=1.96 mm, r_2=1.92 mm).

On the other hand, the acceleration of the trailing bubble due to the wake suction has been observed for only few runs in our data. Figure 5.5 shows an example for the rise velocities of both bubbles (leading and trailing bubble) for s=8. The bubble velocities were almost having the same rise velocity value on average.

The motion of a pair of bubbles is investigated next in detail. Figure 5.6 shows

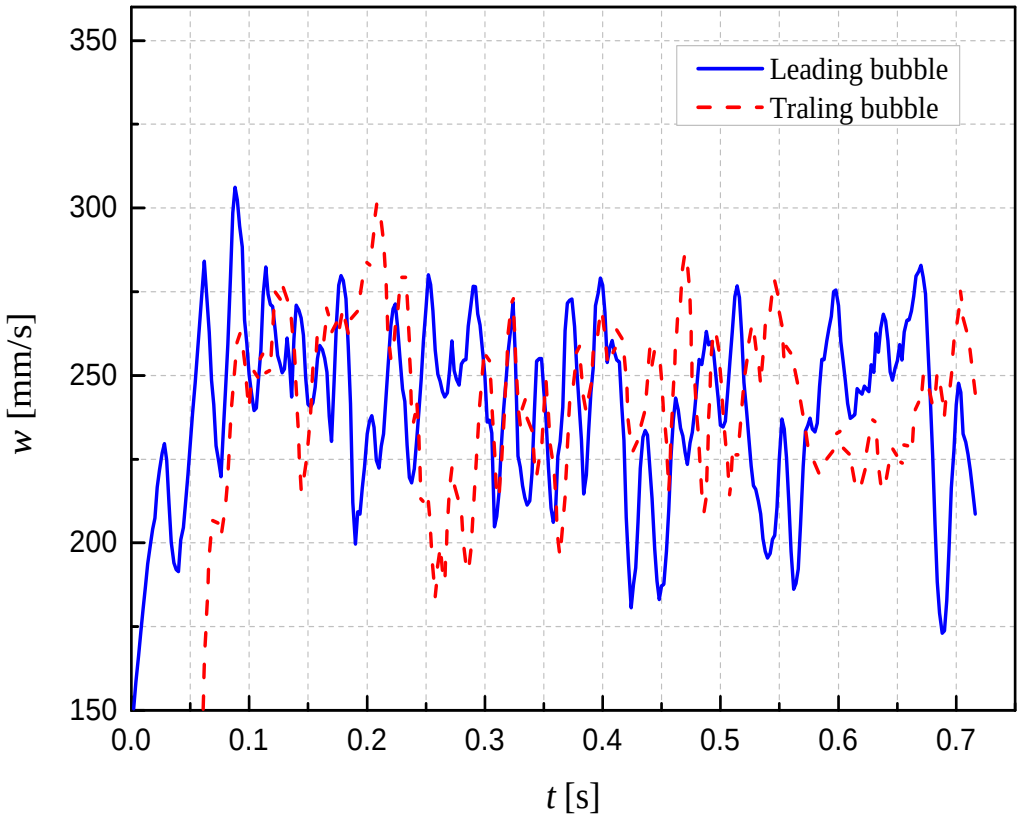
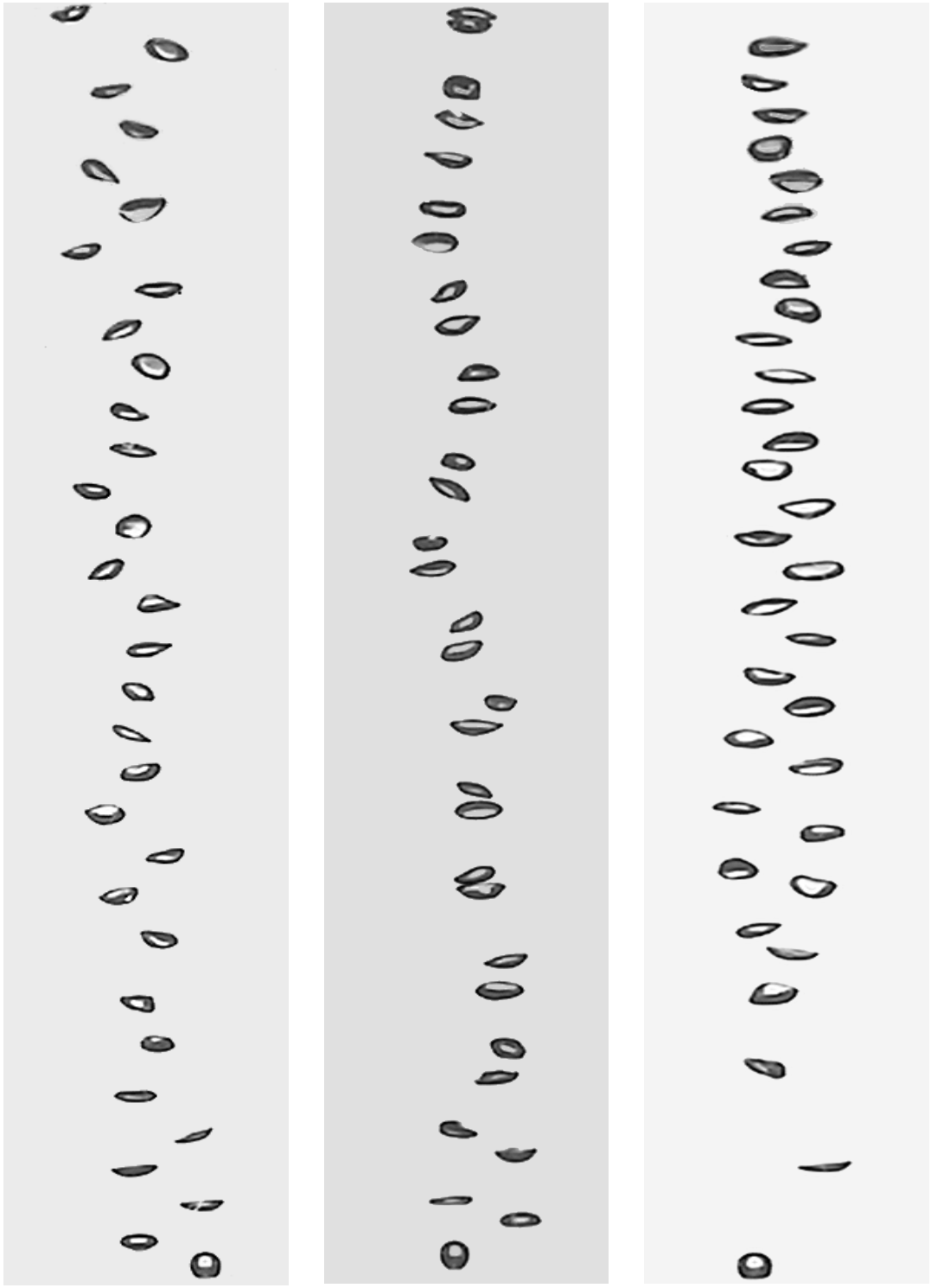


Figure 5.5: The rise velocities of a pair of bubbles at large separation distance (s=8, r_1=1.94 mm, r_2=1.97 mm).

three cases of the rise of two bubbles at different initial separation distances, s. It is noticeable that the pair of bubbles in the three cases showed different behaviours while they rose. In Figure 5.6a, the bubbles separated from each other along the whole path even the separation distance is small, s=4.6, compared to the other two cases. On the other hand, the pair of the bubbles in Figure 5.6b had almost the same initial separation distance, s=4.8, as the previous case. The trailing bubble kept accelerating until it approached with the leading bubble from the side.

It is worth investigating the cause of the separation of the bubble pair in Figure 5.6a and the approach of the trailing bubble to the leading bubble in



(a) (s= 4.6) (b) (s= 4.8) (c) (s= 8.1)

Figure 5.6: Pairs of bubbles rising having offset in their axes at different centre to centre distances. Bubble pairs do not coalesce while they rise.

Figure 5.6b. It was found that the size of trailing bubble slightly deviated from that of the leading bubble. The size of the trailing bubble was appreciably larger

than that of the leading bubble by 1.3% in Figure 5.6a and smaller by 1.3% in Figure 5.6b which might have led to that interesting behaviours. Hence, over the extensively collected data, the size of each bubble was calculated and then each pair of bubbles that obeyed the condition of approaching each other was recorded and labelled as "approaching". The pairs that did not approach each other were labelled as "separating".

The reason for the approach of the bubbles could be due to the average rise velocity of the smaller bubble is greater than that of the larger bubble within the range of the bubble size studied in this research. This is completely opposite to the general understanding that the larger bubble has the greater average rise velocity. The relationship between the terminal rise velocity and the bubble size of Clift et al. (1978), Figure 5.7, indicates that there are three distinct regions, characterised by positive (Region 1), then negative (Region 2) and then positive (Region 3) gradients. In Region 2 on the curve, $0.7 < r < 3.5$ mm, shows that the rise velocity gradient is negative. This means that for a particular size range of bubble, smaller bubbles will rise more rapidly than larger bubbles. The reason for that is the bubble at this range is no longer spherical and develops a secondary motion (lateral migration). This makes the bubble slowing down as it rises. It is important to state that most of the events of the approaching of the trailing bubble were noticeable when the centre to centre separation distance, s, is less than 6. At separations larger than that, the bubbles failed to approach. We think that the bubbles could approach if the experiments are performed with higher liquid height in the tank. The categories of interaction between the rising pairs

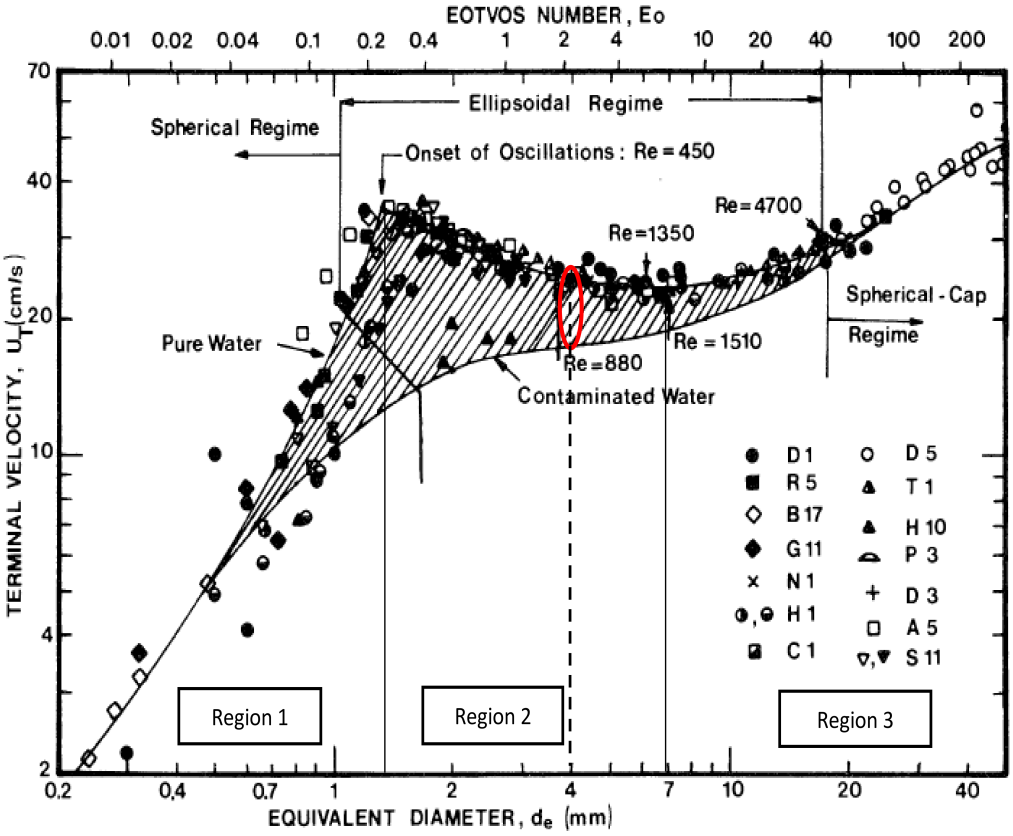


Figure 5.7: The Rise velocity of air bubbles in water (Clift et al., 1978).

of bubbles can be shown in Figure 5.8.

The trajectories and the velocities of each bubble are shown in Figure 5.9. Two cases are shown in this figure, one for each category, separating and approaching. In Figure 5.9a, the leading bubble size is larger than the trailing bubble by 1.3 % (the case in Figure 5.6a). The figure shows that both bubbles rose separating from each other over the whole period. It can be observed that they ended up with a little bit larger offset than that they initially started with. However, in Figure 5.9b, the trailing bubble approached the leading bubble and the initial vertical offset between the bubbles reduced by 50 %. This is because the size of the trailing bubble was smaller than the leading bubble size by 1.3 % (the case in Figure 5.6b). The average rise velocity, w_2, of the trailing bubble was greater

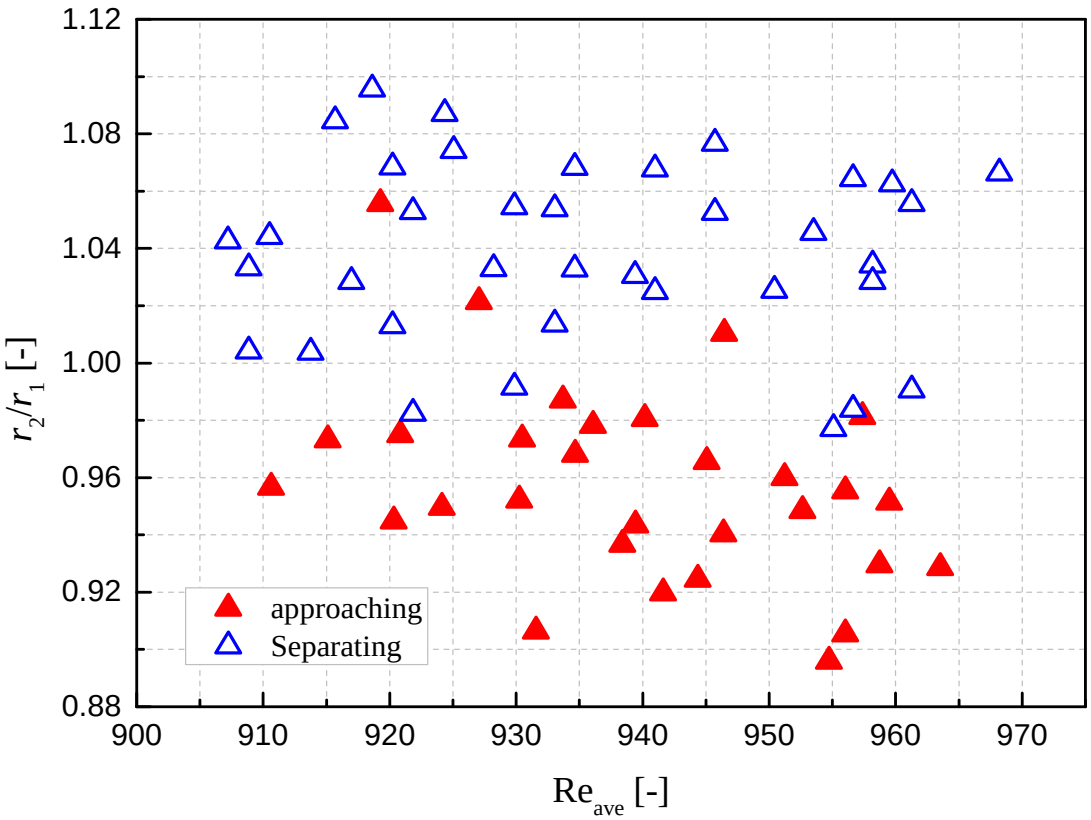


Figure 5.8: The effect of the bubbles size deviation on the interaction of bubbles.

than that of the leading bubble, w_1, by $\simeq 2.8\,\mathrm{mm/s}$. It is also clear that the bubbles in Figure 5.9b had temporal delays which were clearly seen in u and v velocities in this figure. However, the bubbles in Figure 5.9a did not show similar behaviour and they almost run entirely out of phase.

Similar results were observed by Kusuno and Sanada (2015a) but for lower Reynolds numbers and spherical bubbles. Kusuno and Sanada (2015a), in addition to the separating and the approaching mode, observed an overtaking category. However, this mode was not observed in the present work. That could be because their studied bubbles were spherical and hence the difference in the average velocity of the rising pairs of bubbles is greater than that in our case

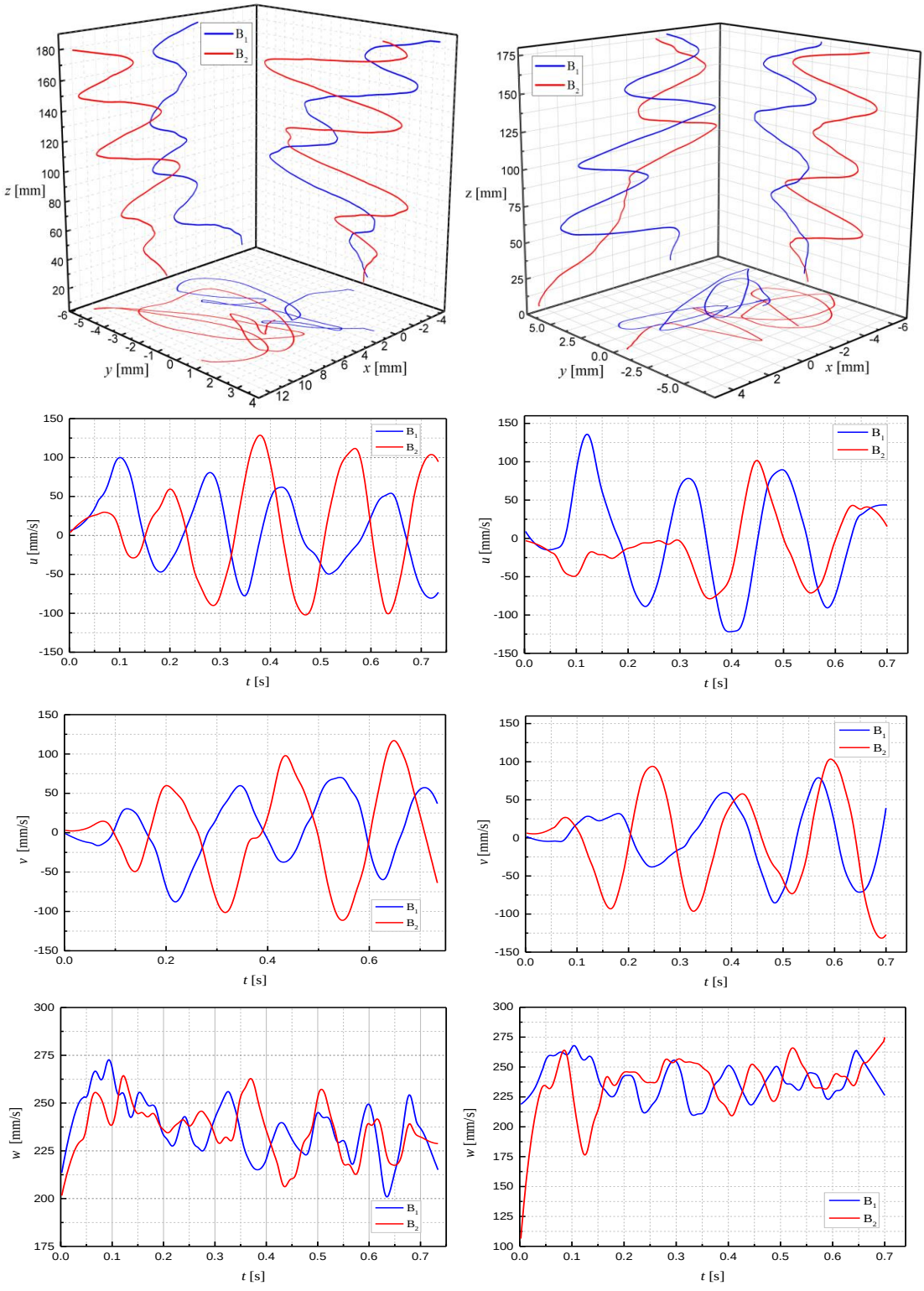


Figure 5.9: Three dimensional trajectory and bubble velocity for a pair of bubble: (a) separating (b) approaching.

even at very small size deviation ($\simeq 1\%$). It can also be well explained by closely looking at the relationship between the bubble size and the terminal rise velocity of Clift et al. (1978). It is observable that the gradient in Region 2, ellipsoidal region, is less abrupt than that in Region 1. That could be the reason behind the appearance of the overtaking category in the experiments of Kusuno.

The approaching category is important in the process of bubble-bubble interaction because it might result in the coalescence of the bubbles, particularly when the separating distance between them is small enough. The trailing bubble has two possibilities to coalesce with the leading bubble. First, the trailing bubble approaches the leading one and collides with it while they are still at small offset separating them. The other scenario is that when the trailing bubble is horizontally aligned with leading one. However, the coalescence process was not seen for all of the bubble pairs reported in this chapter. The coalescence is expected when the initial separation distances are significantly small and hence the coalescence is addressed in the next chapter.

Finally, in Figure 5.6c, the bubbles rose with an initial separation distance, s, equal to 8.1. The trailing bubble approached the leading bubble and then the vertical separation distance remained almost constant. This constant distance was somehow stable so that it is not clear whether it can be considered as an equilibrium distance that was pointed out by Yuan and Prosperetti (1994) for nondeformable bubbles or not. The equilibrium distance is generated, as explained by Yuan and Prosperetti (1994), due to the balance between the repelling force (potential force), generated in the flow field after the passage of the leading

bubble, and the attractive force, as a result of the viscous forces. Although the viscous forces are missing here, it is worth investigating this behaviour because some of the pairs of rising bubbles showed a constant vertical distance between them in the videos.

Yuan and Prosperetti (1994) reported that the equilibrium distance is unique for the range of Reynolds numbers, Re $\leq$ 200, they investigated. However, it is noticeable here that the trailing bubble sometimes escaped from the vertical line. This was also observed in the work of Watanabe and Sanada (2006) for deformable bubbles (Re = 100). This could be the result of the three dimensional effect of the experiments compared to the axi-symmetric numerical analysis done by Yuan and Prosperetti (1994). Another reason could be that the bubbles studied here have a large scale of deformation, not to mention the effect of the vorticity shedding from the wake of the upstream bubble. Therefore, we think that it would be better showing the equilibrium distance in terms of the 3D centre to centre separation distance, l. The equilibrium distance, l, can be defined as the constant distance achieved after the approach of the pair of the bubbles normalised by the initial average bubble radius. A sketch showing the distance l is depicted in Figure 5.10.

The results of the transient non-dimensional equilibrium distance, l, is shown in Figure 5.11a. The rising pair of bubbles showed almost constant distance particularly in the last 0.2 s. The equilibrium distance is shortened in some cases and the maximum deviation for some runs in the figure is within $1r$ on average. Thus, it can be reported here that the equilibrium distance for a deformable

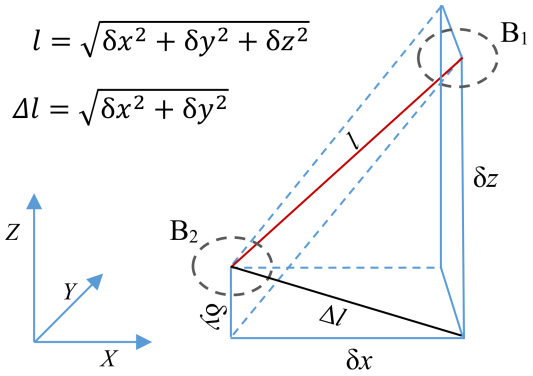
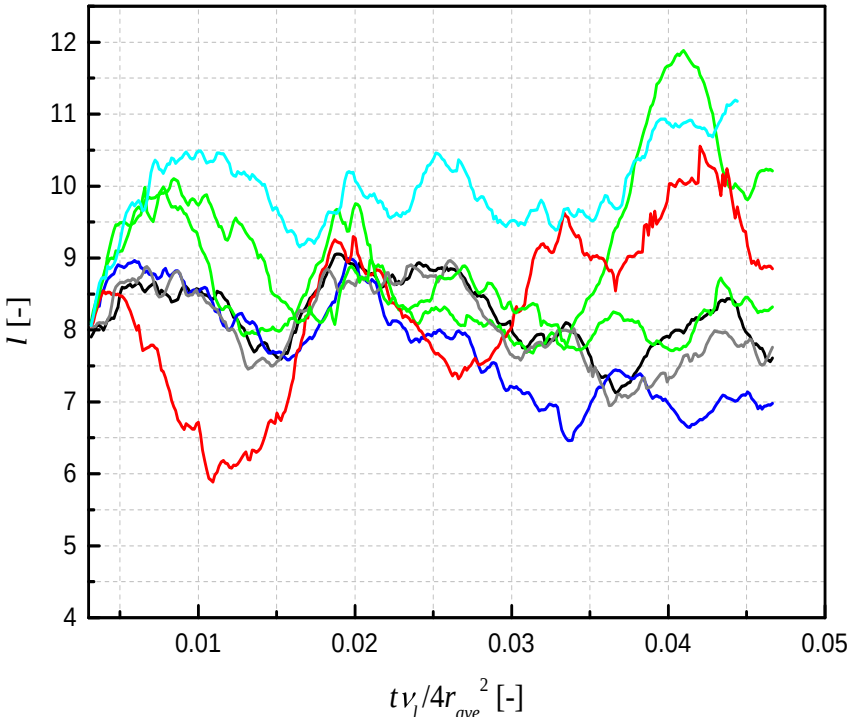


Figure 5.10: A sketch showing the 3D centre to centre equilibrium distance, l.

bubble does exist. This could be due to the difference in bubble sizes where, in this figure, all of the leading bubble sizes were either equal or appreciably larger than the trailing bubble sizes. However, if the trailing bubble is smaller, we will see a negative gradient for the l, which reflects the approach of the trailing to the leading bubble. The results for the l when the trailing bubble is smaller is shown in Figure 5.11b.

(a)



(b)

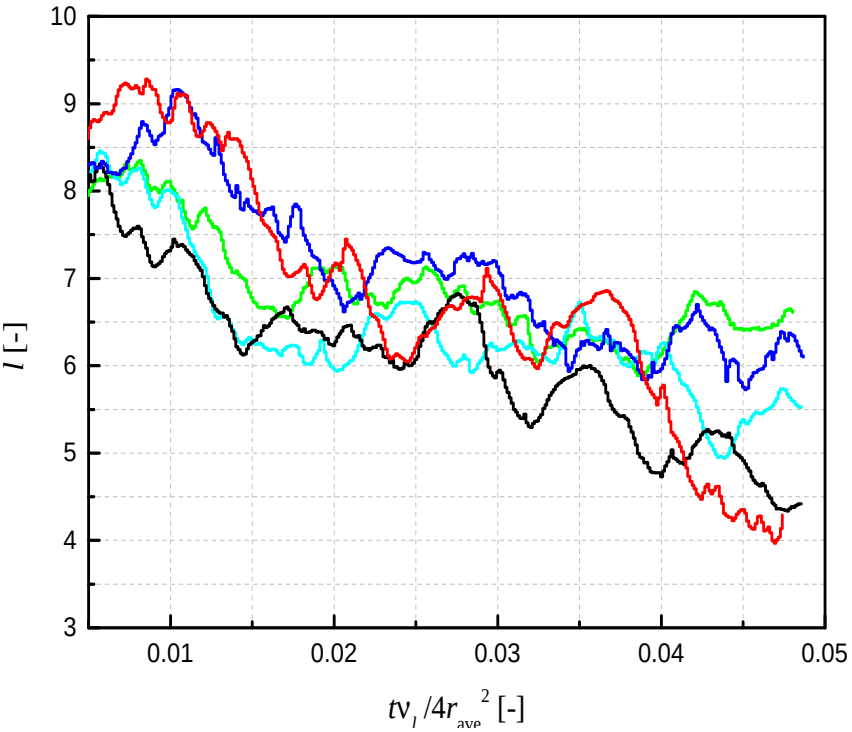


Figure 5.11: The 3D centre to centre equilibrium distance, l, between the bubbles (a) the trailing bubble is either equal or larger than the leading bubble, (b) the trailing bubble is smaller than the leading bubble.

Next, the effect of the interaction between the bubbles on the trajectories is discussed. As it was previously demonstrated that the studied bubbles rise in mostly zigzag trajectory, either keeping the zigzag motion or being affected by the interaction will be investigated. To accomplish that, a new parameter is introduced that is the deviation of both bubbles from the vertical line, Δl, which can be defined as $\Delta l = \sqrt{\delta x^2 + \delta y^2}$. Δl is also depicted in Figure 5.10.

In order to evaluate the effect of the distance between the bubbles, s, Δl is plotted in Figure 5.12a-b against the height of the liquid inside the column, z_l. The instantaneous locations of three observed runs are graphed and for (s=5 and s=8). Two corresponding figures (one for each case) are also projected on δy-δx plane to show the interaction from the above view. These figures are shown in Figure 5.12c-d. In Figure 5.12a and Figure 5.12b, it can be recognised that all the bubbles rose with nearly the same trajectory until they were at about z_l= 30 mm. The reason could be that the wake of leading bubble has not been, to some extent, well developed. Then, the bubble in both figures showed different trajectories during the remainder of their rise.

It is observed that the bubbles released at a small separation distance, s=5, rose with a little deviation in their trajectories for the six observed runs in Figure 5.12a. While, at larger separation distance, s=8, the trajectories were considerably deviated. This would reflect that the bubbles experience strong interaction when they are at small centre to centre separation distance and weak interaction at large separation distances. This can be justified due to the effect of the vorticity of the leading bubble wake that might cause the closest trailing bubble

bouncing when it is located near its effective region (Harper, 1997; Hallez and Legendre, 2011).

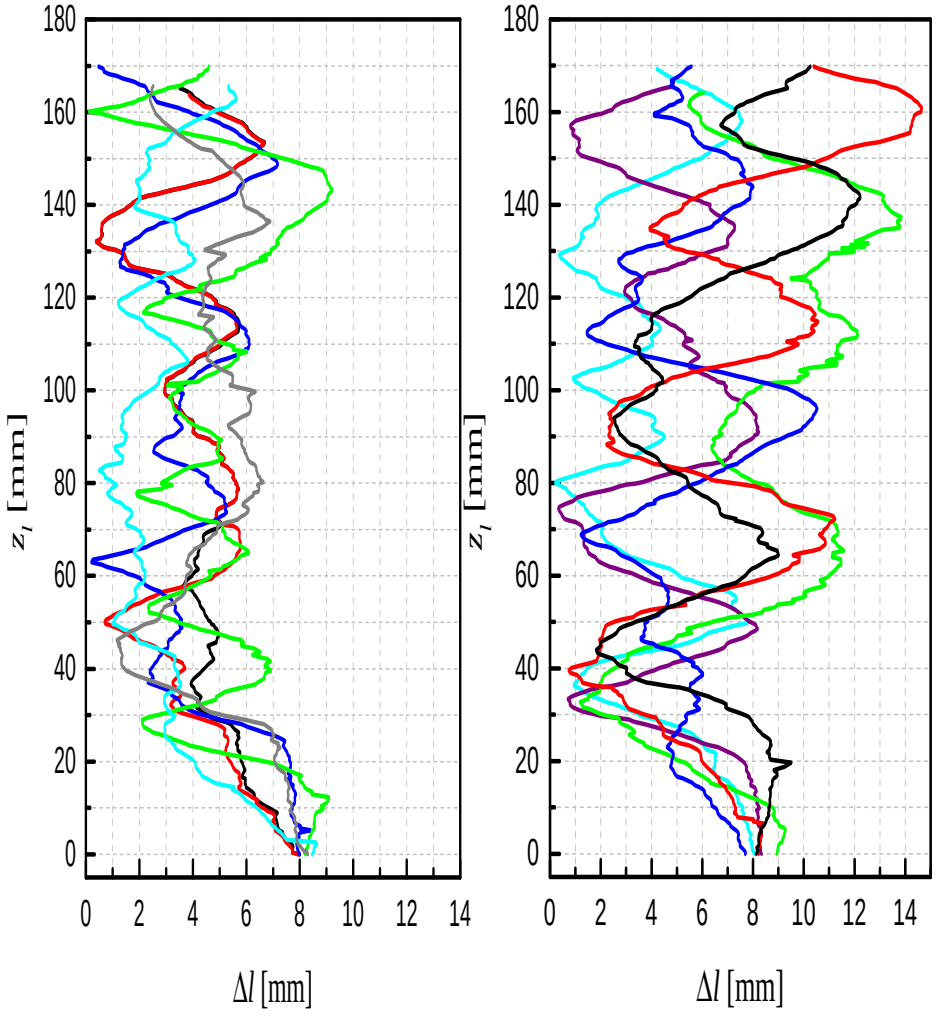
It is important to assess the degree of the scattering of the bubble trajectories in a quantitative way. Hence, the standard deviation of Δl, γ, is defined by Equation 5.1:

$$\gamma = \frac{1}{N} \sum_{i=1}^{N} \left(\Delta l_i - \bar{\Delta} l \right)^2 \tag{5.1}$$

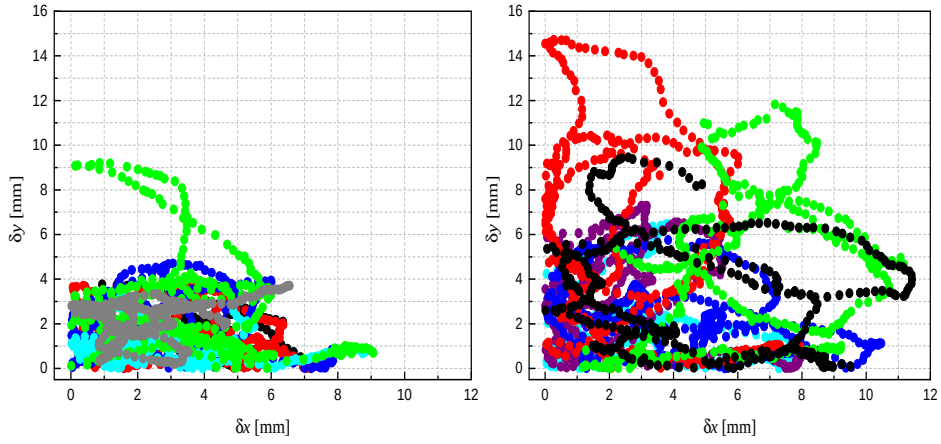
where N is the number of the observed runs and $\bar{\Delta} l$ is the mean value of the six runs of deviation studied. This means that the mean will be calculated over a row of six points and a column of 400 points which represent the number of frames. Δl_i is the instantaneous deviation of each data point in each run. The experimental data in Figure 5.12 was used to produce the degree of scattering of the bubbles, γ, in Figure 5.13. The scattering of the bubble, γ, was approximately identical for s=5 and s=8 at $z \leqslant 30\,\text{mm}$. Then, the value of γ significantly deviated for the smaller separation distance. Therefore, it should be emphasised that strong interaction between the bubbles increases as s decreases.

5.3.2 Bubbles rising side by side

The rise of two bubbles side by side is discussed in this section. Figure 5.14a-c shows three cases of rising bubbles aligned horizontally. As is to be expected with individual experiments, they are all different but do share a "bouncing" mode whereby the bubbles come close and then separate again. From these limited examples, it appears that one or two bounces occur before the bubbles become separated for the remainder of their rise. The effect of the vorticity generated at



(a) s=5 (b) s=8



(c) s=5 (d) s=8

Figure 5.12: Hydrodynamic interaction effect on bubbles trajectories.

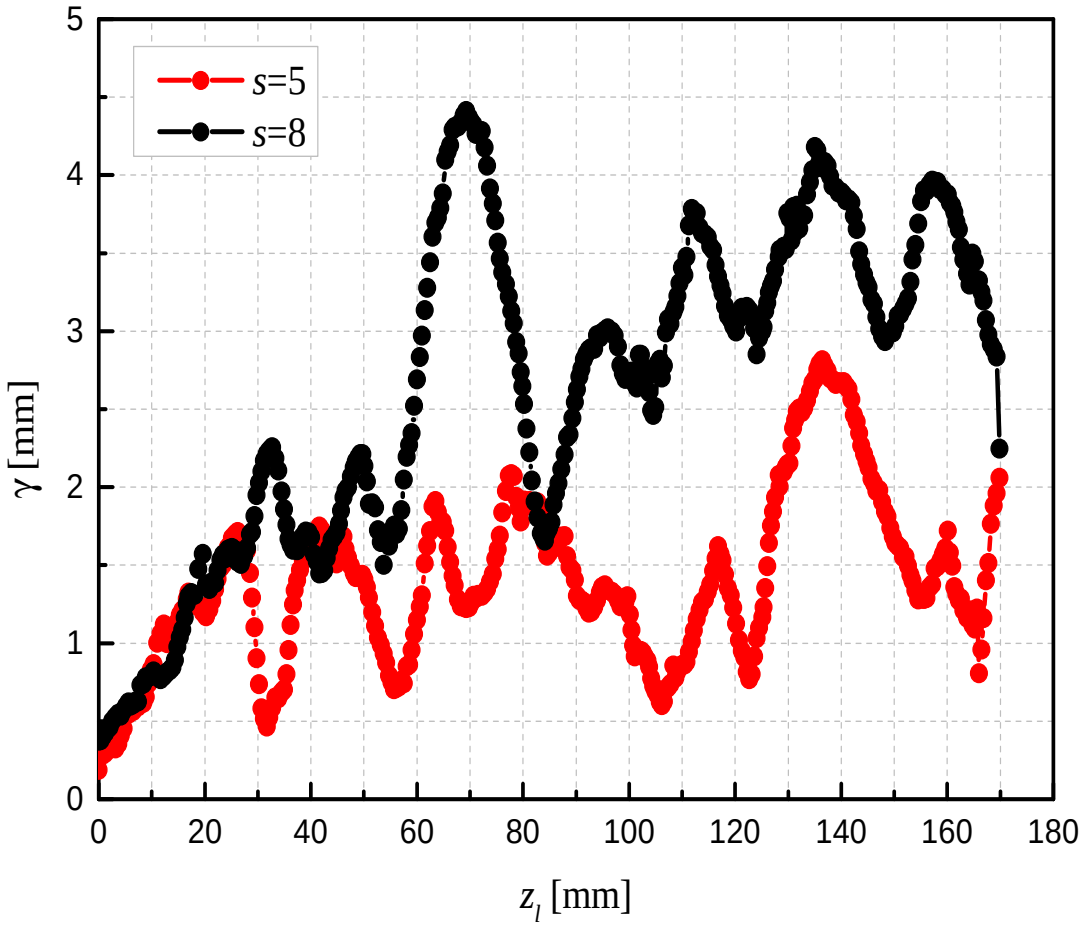
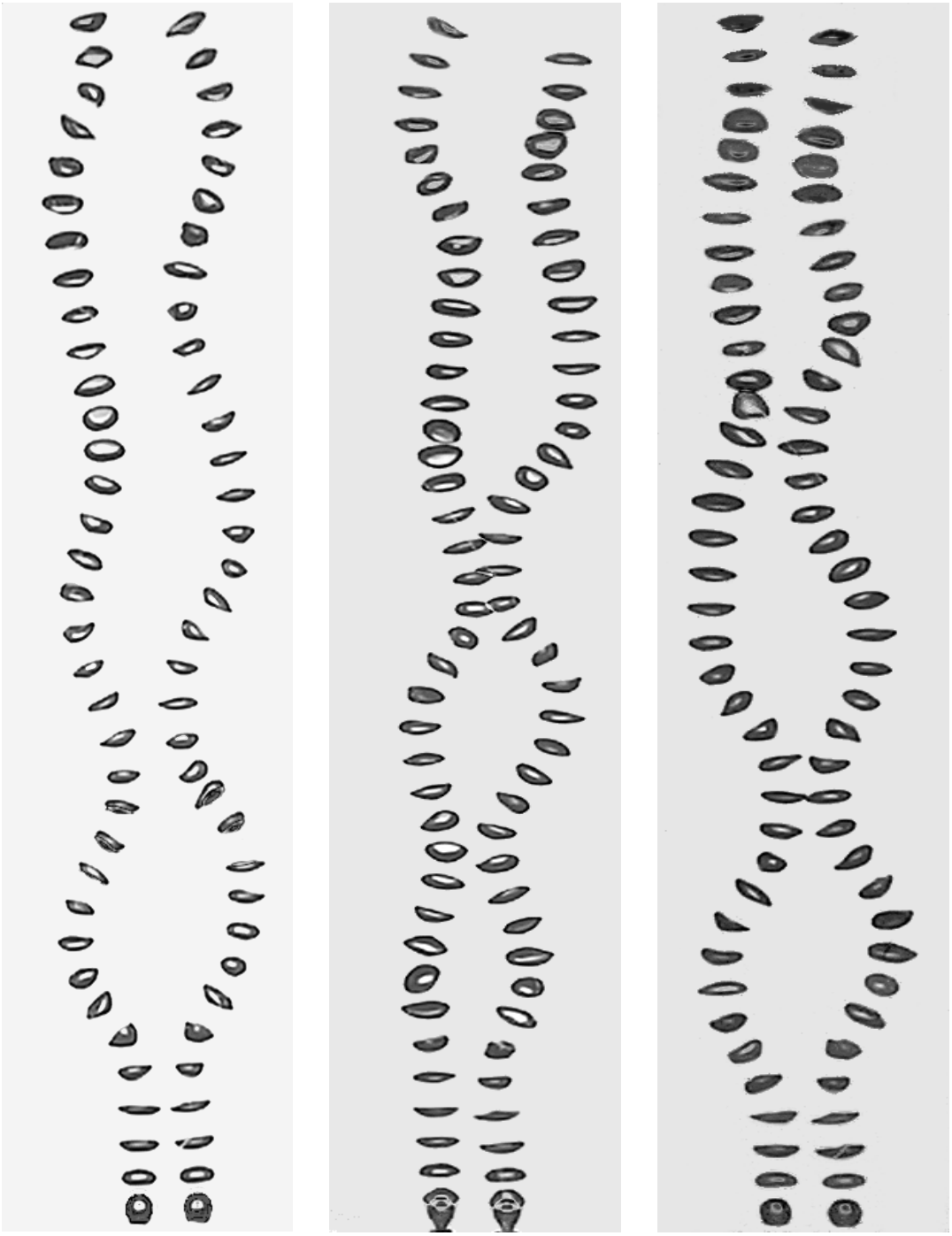


Figure 5.13: Scattering degree of bubble-bubble interaction.

the surface of the bubbles in such kind of interaction is acting in the horizontal direction which would be responsible for the bubbles altering their directions. That was pointed out by the numerical analysis of Legendre et al. (2003) at $30 \leq \mathrm{Re} \leq 100$. Hence, the repulsive force of the vorticity induces the lift force on the bubbles. However, the attractive forces should be dominant at the range of Reynolds number used in this study. That was not observed here, which could be considered due to the complex behaviour of our large bubbles as every bubble could take its own trajectory away from its counterpart bubble. The coalescence was also not observed in any of the experimental runs.



(a) (b) (c)

Figure 5.14: Pairs of air bubbles rising side by side.

Table 5.1: Experimental parameters of the investigated cases in Figure 5.14.

Case	r_{LB} [mm]	r_{RB} [mm]	R_{i} [-]	z_f [-]
Figure 5.14a	1.94	1.97	0.981	0.96
Figure 5.14b	1.95	1.99	0.977	2.14
Figure 5.14c	1.94	2.05	0.953	1.52

Further to our observations regarding the effect of the bubble size deviation on the interaction of the bubbles, the rising of bubbles side by side is the best way to test that. That is because both bubbles would be theoretically experiencing the same drag force. In addition, the left bubble, (LB) or the right bubble (RB) will not accelerate due to the effect of the wake. Hence, the rise velocity would be the only characteristic feature to evaluate the terminal behaviour of each bubble. From Figure 5.14 the three cases of bubbles present a good example for comparison and evaluation.

In Figure 5.14a the bubble on the left is smaller than the one on the right by 1.9 %. As can be seen from the figure that the smaller bubble has overtaken the larger one appreciably. The dimensionless final distance, z_f, between the bubbles was measured to be about 1. The second case in Figure 5.14b the left bubble was smaller by 2.3 %. It is clear that the smaller bubble further surpassed where z_{f} was more than 2 at the end of the recorded height. Finally, the bubbles in Figure 5.14c deviated by 4.7 % and the final distance, z_f, was 1.52. Table 5.1 summarises the detailed information on the bubbles discussed in Figure 5.14, where R_i is the initial ratio of bubble sizes deviation (r_{LB}/r_{RB}).

It can be reported here that there is no such kind of consistency relating the

increase in the final vertical distance, z_f, between the bubbles to the bubbles relative size. This inconsistency is shown in Figure 5.15 for a larger number of side by side cases at which the smaller bubbles ended with a greater distance compared with the larger bubbles. Many factors could be contributed to such inconsistency, for example, level of contamination of the liquid and modes of shape oscillation. Additionally, all the pairs of the bubbles in Figure 5.14 have not shown any kind of symmetry in their paths which could be a result of the slight deviation in their initial sizes as well.

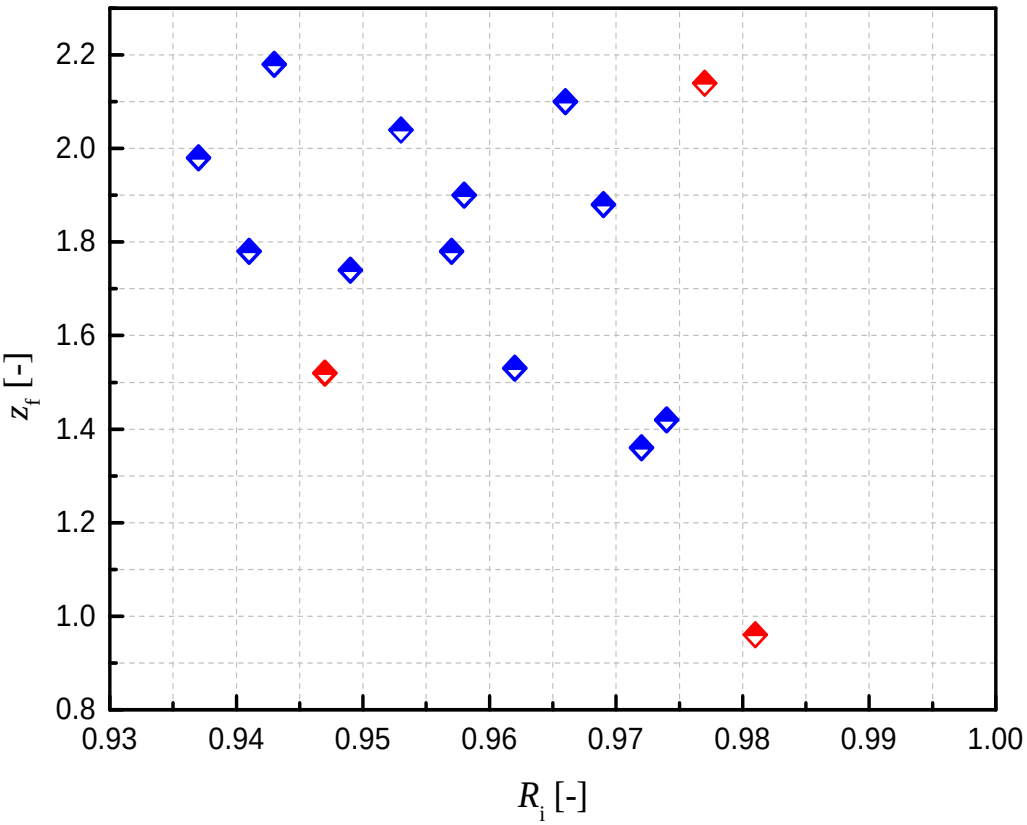


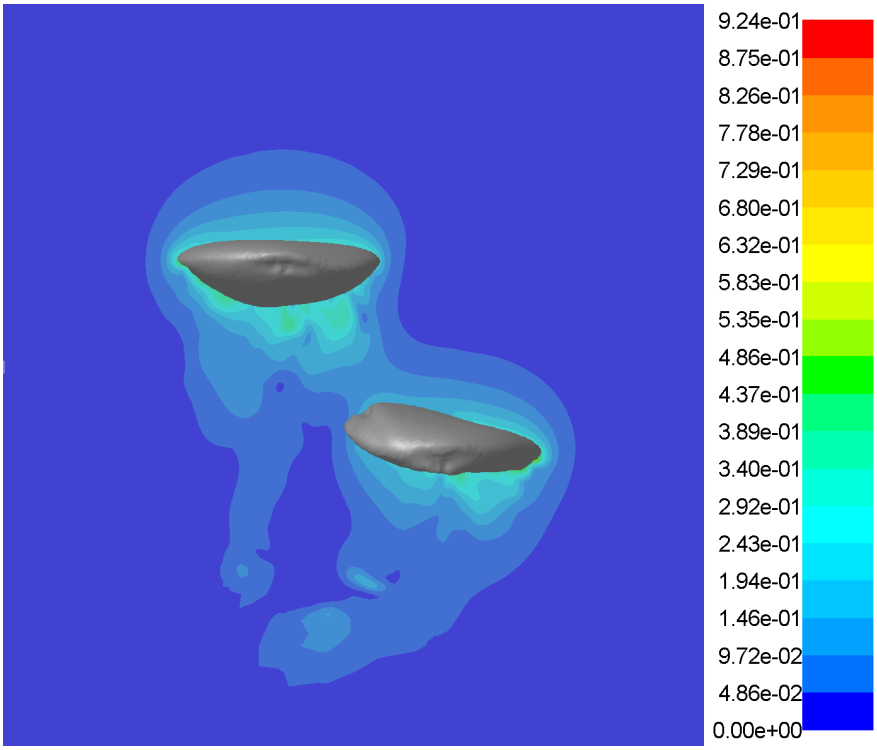
Figure 5.15: The final separation distance related to the initial relative size of bubbles rising side by side, the red symbols represent the data points in Table 5.1.

5.4 Numerical investigation of bubble-bubble interaction

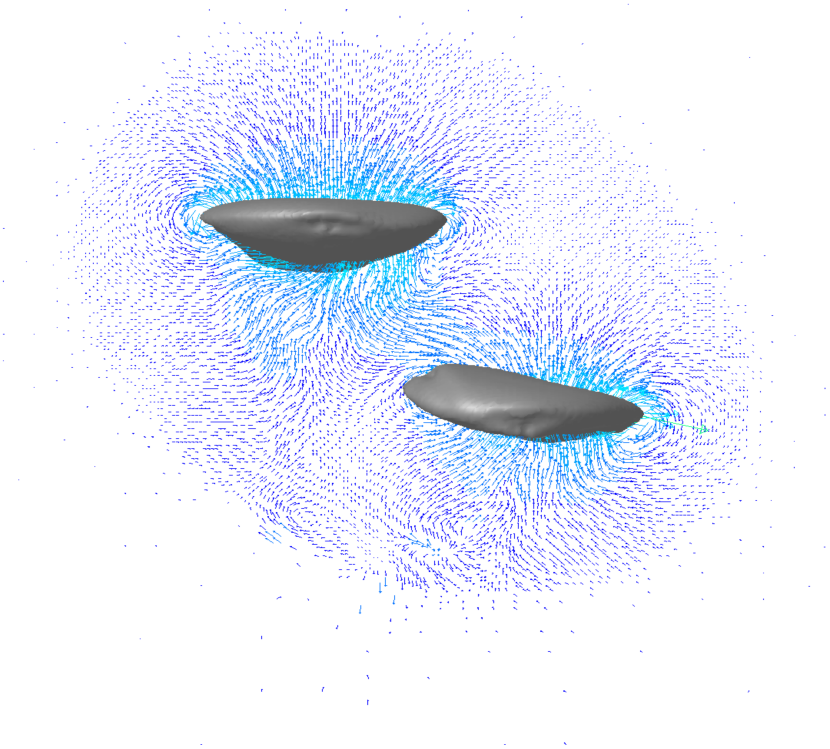
In this section, the motion of bubble pairs rising having offset in the vertical and horizontal coordinates were modelled numerically because detailed information can be extracted from the simulations compared to the experiments. That means that a better understanding of the hydrodynamic interaction between the rising bubbles can be achieved. Therefore, two spherical bubbles were allowed to rise freely. All the simulations in this section were done using a mesh with reasonable quality that was 0.125 mm for the finest level of adaptive mesh. That was based on the predictions that the coalescence is not expected in such kind of large centre to centre separation as the experiments have also approved. However, if the coalescence is likely to happen, the mutual distances between the bubbles have always to be smaller than the mesh size otherwise the coalescence would occur (Bunner and Tryggvason, 2002). Grid independence was described in detail in Chapter 3.

The contribution of the hydrodynamic effects is important in deciding the ultimate state of the interaction between the bubbles whether they, for example, coalesce or bounce. The distribution of the velocity and the velocity vectors around the leading and the trailing bubbles are shown in Figure 5.16a-b as an example. These figures also show a developed velocity distribution and vorticity structures around the bubbles. This would reflect the strength of the numerical adaptive mesh in capturing such kind of small structures.

It is important here to address the effect of the region behind the leading



(a)



(b)

Figure 5.16: Distribution of velocity around two rising bubbles at their mid way through the computational domain (a) contours of velocity magnitude (b) velocity vectors.

bubble (the wake) on the behaviour of the trailing bubble. Here the bubbles were placed having equal sizes. Detailed information on the size of the bubbles and the number of the elements per radius are presented in Table 5.2. The simulation controls and boundary condition are detailed in Section 3.1.7.1. The results of a pair of bubbles are qualitatively agreed with the experiments whereas it has been pointed out that the trailing bubble did not approach the leading bubble and a constant distance was maintained between the bubbles.

Since, the numerical simulation has the strength to show the intervals when the trailing bubble is located near the wake region of the leading bubble, detailed distribution of velocity in nearby and far fields flow regions behind the leading bubbles is shown in Figure 5.17a. This figure also shows the distribution of the vorticity around both bubbles. The vorticity structure is shown in Figure 5.17a using a 2D plane inside the computational box.

Since the bubbles studied here tend to migrate laterally, sometimes their existence within the flow field generated by the leading bubble wake is intermittent. In addition, the vorticity distribution around the bubbles is not fully developed because they occasionally travelled out of the plane. This is normal because of the three dimensional nature of the cases investigated here. Therefore, the Q-criterion approach could be the best tool showing the 3D propagation of the vorticity and the history of the wakes of both bubbles. The Q-criterion is shown in Figure 5.17b.

The trailing bubble rose up and the wake of the leading started developing. The trailing bubble now reached the tail of the leading bubble wake. Afterwards,

Figure 5.17: Distribution of vorticity for a pair of equally sized bubbles bubbles rising at s =4.5 ($\triangle t$= 0.08 s) viewed using (a) 2D plane (b) Q-criterion.

the trailing bubble gradually approached the wake of the leading bubble but it did not enter the wake except in the sixth shot of Figure 5.17b. Then, it is observed that the trailing bubble separated from the wake region and kept a constant region particularly in the last three shots. It is worth investigating the equilibrium distance between the bubbles from the numerical simulations.

Figure 5.18 illustrates the instantaneous nondimesioanlised equilibrium distance between the bubbles, l, over the whole time period. From the figure, the bubbles maintained a constant distance with a small deviation escpecially near the end of the simulation. Thus, it can be reported here that there is a constant equilibrium distance between the rising bubbles for this case where the bubbles were equal in sizes. Therefore, it can be said that the numerical simulation has in general agreed with the experiments. It can be also reported here in contrary to the numerical simulations of Hallez and Legendre (2011) that the approach of the equally sized bubbles has not been seen neither in the present simulations nor in the experiments.

The effect of the deviation in the size of the rising pairs of bubbles on their interaction is now discussed and compared with the equally sized rising pairs. Two different cases were set up to test the response of the numerical simulations to the slight change between the rising pairs of bubbles and how that is valid against the experiments. The bubbles in both cases were arranged so that the trailing bubble was smaller than the leading one by 5 % and 10 % respectively. Detailed information on the bubbles and the quality of the mesh utilised are tabulated in Table 5.2.

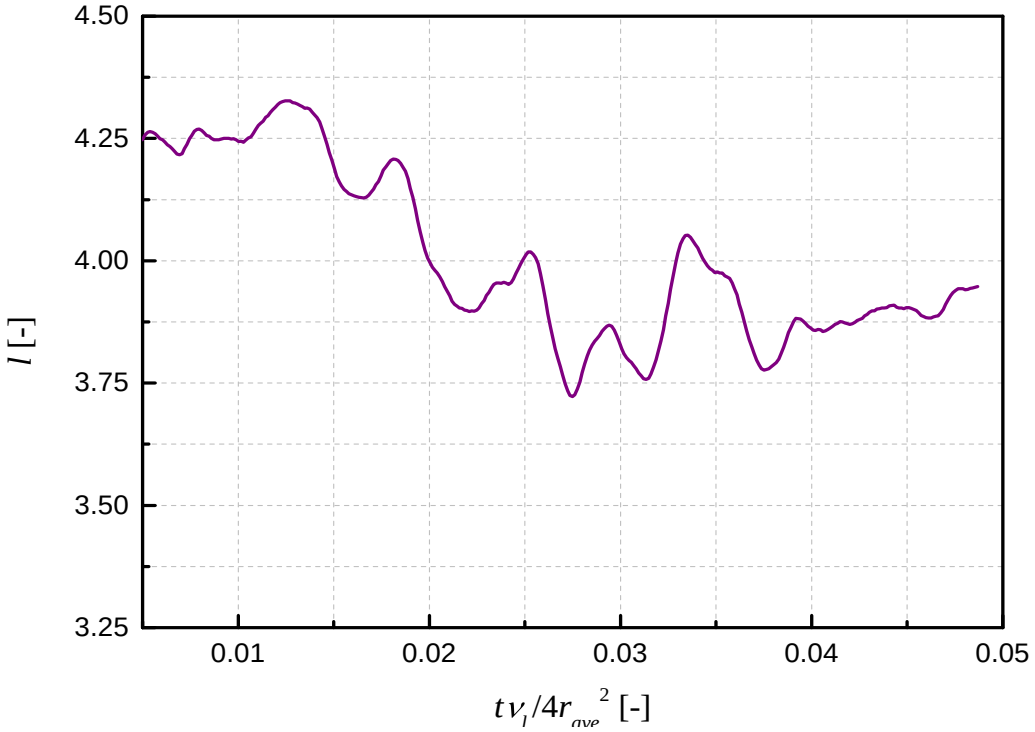


Figure 5.18: Instantaneous behaviour of the 3D centre to centre equilibrium distance, l, between the bubbles from the simulations.

Table 5.2: Summary of the simulation parameters for the investigated cases.

Case	s [-]	r_1 [mm]	N_r [-]	r_2 [mm]	N_r [-]
a	4.5	2	16	2	16
b	4.5	2	16	1.9	15.2
c	4.5	2	16	1.8	14.4

where N_r is the number of grid points per radius. The results of the numerical solutions of both cases and the previous case when the rising bubbles were equally sized are figured in Figure 5.19a-c. The terminal distance between the rising pair in Figure 5.19b is smaller than that in Figure 5.19a in which the bubbles kept almost a stable equilibrium distance. That can be attributed to the acceleration of the trailing bubble as it had the greater average rise velocity.

Further decrease in the size of the trailing bubble in Figure 5.19c resulted in the further approaching of the trailing bubble with the leading bubble from the side and therefore they travelled side by side. It is also observed that the approaching happened nearly at the middle of the computational domain height. Hence, encouraging signs can be read from the figure below that the computational calculations have well responded to the slight deviation in the size of the rising bubbles. This can be considered as a verification to the experimental observations in the previous sections.

Interestingly and as a result of the interaction between the bubbles, the coalescence is more likely to occur in the last two cases if smaller separation distance between the bubbles was intended. Thus, the next chapter will cover the interaction of bubbles at small separation distances.

Figure 5.19: Comparison of the numerical simulations for differently sized bubble pairs to the equally sized pair of bubbles (a) equally sized bubbles ($\triangle t$= 0.12 s)(b) trailing bubble, right bubble, smaller than the leading bubble (left bubble) by 5 % (c) trailing bubble (right bubble) smaller by 10 %.

5.5 Summary

Owing to the extensive experimental data collected in this study, the motion of a pair of bubbles rising configured with vertical offset upon release or rising side by side was investigated. Apart from some small experimental inconsistencies, all bubbles were approximately of the same initial diameter. The effect of the wake of the leading bubble was highlighted in accelerating the trailing bubble for limited cases. Encouraging findings were experimentally achieved and addressed correlating the approach or the separation of the trailing bubble from the leading bubble depending on the initial slight deviation in the trailing bubble size. Three dimensional numerical simulations were implemented here which have qualitatively agreed with the experiments. As a result of the bubble size deviation, the equilibrium distance between the bubbles found for the spherical rising bubbles has been pointed out for the deformable bubbles in this study.

In the case of bubbles rising side by side, the bubbles bounced and they did not show sufficient attraction for the coalescence. The motion of the bubbles side by side was also used to test the validity of the effect of the appreciable deviation in bubble sizes on the approaching of the trailing bubble to the leading bubble. The results have statistically provided the evidence that the smaller bubbles rise faster than the larger bubbles which might have led to the approach of the trailing bubble.

6

INTERACTION OF BUBBLE PAIRS AT SMALL SEPARATION DISTANCES

6.1 Introduction

As a consequence of the interaction between the bubbles, the coalescence could occur between the rising bubbles. The coalescence of bubbles has been the subject of many investigations. Most of those have been theoretical or direct numerical simulations. However, lacking of experimental verifications particularly for the deformed bubbles and the incomplete understanding of the modelling of the coalescence are noticeable in the previous work reported. Hence, it is aimed in this chapter to provide verification materials and identifying the important parameters that govern the process, not only through experiments but also by numerical simulation. Indeed, the experiments will additionally provide validation material for the numerical simulations. This is because many factors other than, for instance, computational grid refinement or cells distortion near the surface could be affecting the coalescence process. Many simulations were carried out in this chapter with the aid of the adaptive mesh technique that we have developed. Since the focus is on studying the coalescence insightfully, this work would represent a guide for bubble column modellers in systems where coalescence is experienced.

6.2 Experimental procedure

Three different axial separations between the pair of nozzles were used in order to generate bubbles to study the effect of this parameter on the likelihood of coalescence. An axial displacement of 0.25 mm was fixed between the nozzle tips for each set of nozzles. Therefore, the three initial axial separations, $\triangle x$, normalised by the average bubble radius r_{ave}, were 2.25, 2.375 and 2.5. Extensive measurements were collected for each nozzle set 232, 219 and 242 data points respectively to develop a reasonable database for bubble-bubble interaction and coalescence of bubbles.

Depending on our experimental setup, two bubbles with appreciable deviation in radii are generated. The leading bubble, B_1, the first generated bubble, on occasion, assumes an ellipsoidal shape even before the second bubble, B_2, trailing bubble, is released. In other words, both bubbles will always be having different shapes, different separations and different sizes along the experiments. The deviation in the released bubble pairs did not exceed 10% throughout the whole experimental runs. The data was grouped depending on the vertical separation distance, $\triangle z$, normalised by r_{ave}. The data was divided into several groups or slots depending on an increment equivalent to 0.5 in $\triangle z$ representing each group. This criterion was adopted here because the relative initial angle, θ_i, between the encountered bubbles will be almost at 10° with which there is not much noticeable variation that the bubbles would experience (Maeda et al., 2013).

Three different dimensionless distances that were normalised by the average

radius of the bubbles, r_{ave}, will be used in this chapter. These distances are axial separation distance, $\triangle x$, vertical separation distance, $\triangle z$, and centre to centre distance, s. A general arrangement of the bubbles rising side by side or having an offset is shown in Figure 6.1.

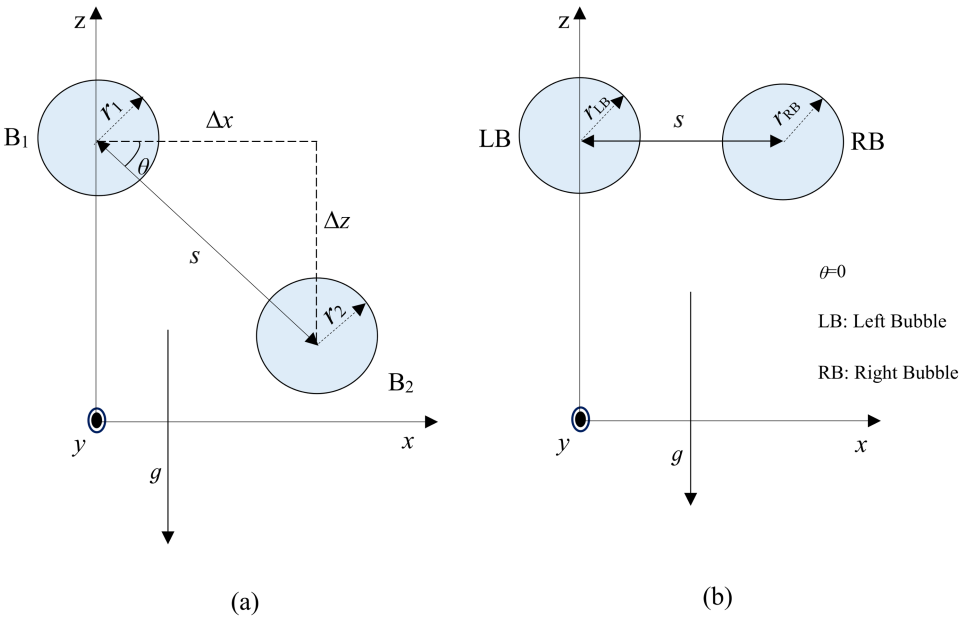


Figure 6.1: Relative configurations and coordinate system of bubble pair rising (a) bubbles rising at an offset, (b) bubbles rising side by side.

6.3 Factors affecting coalescence of bubbles

In this section, we will try to highlight and address the different factors that affect the coalescence of bubbles. For that purpose, the collected experimental data will be analysed. Accordingly, the numerical modelling will be set depending on these factors in the next section. This would really help for better understanding of that complex process and therefore its modelling can be improved.

6.3.1 Effect of separation distance

Since the bubbles were released at small axial separation distances, many coalescence events were recorded. The coalescence probability data was correlated with the vertical separation distance, $\triangle z$, for all the axial separation distances, $\triangle x$, used as can be seen in Figure 6.2. At $0 < \triangle z < 0.5$ the bubbles were considered to coalesce at side by side mode, $0° < \theta < 10°$.

First of all, the probability of coalescence when the bubbles rose side by side was at its highest value, 0.35, for the smallest axial separation distance, $\triangle x$=2.25. In comparison to the other two axial separation distances studied $\triangle x$=2.375 and $\triangle x$=2.5, the coalescence probability has generally decreased to 0.26 and 0.2 respectively.

Then, the probability of coalescence was significantly decreased as the relative angle, θ_i, slightly deviated from 0°. This sudden decrease was observed when the bubbles, for all the axial separations, were vertically separated by a distance approaches to 1. A probable reason for that is that the effect of the vorticity of the leading bubble wake is significant at that distance. The vorticity here acts as a drift force (lift force) on the trailing bubble as was proposed by the analytical and numerical studies of Harper (1997); Hallez and Legendre (2011). This could result in the trailing bubble being quickly pushed away from the effective region of attraction of the leading bubble and therefore the chance of coalescence would be decreased. Although this scenario was reported for the spherical bubbles, this can be considered valid here for the ellipsoidal bubbles studied based on the decreased

probability of coalescence observed. However, for the ellipsoidal bubbles, another scenario is expected where even if the trailing bubble is initially drifted from the line of the interaction, it would rejoin again due to the lateral migration nature of both ellipsoidal bubbles.

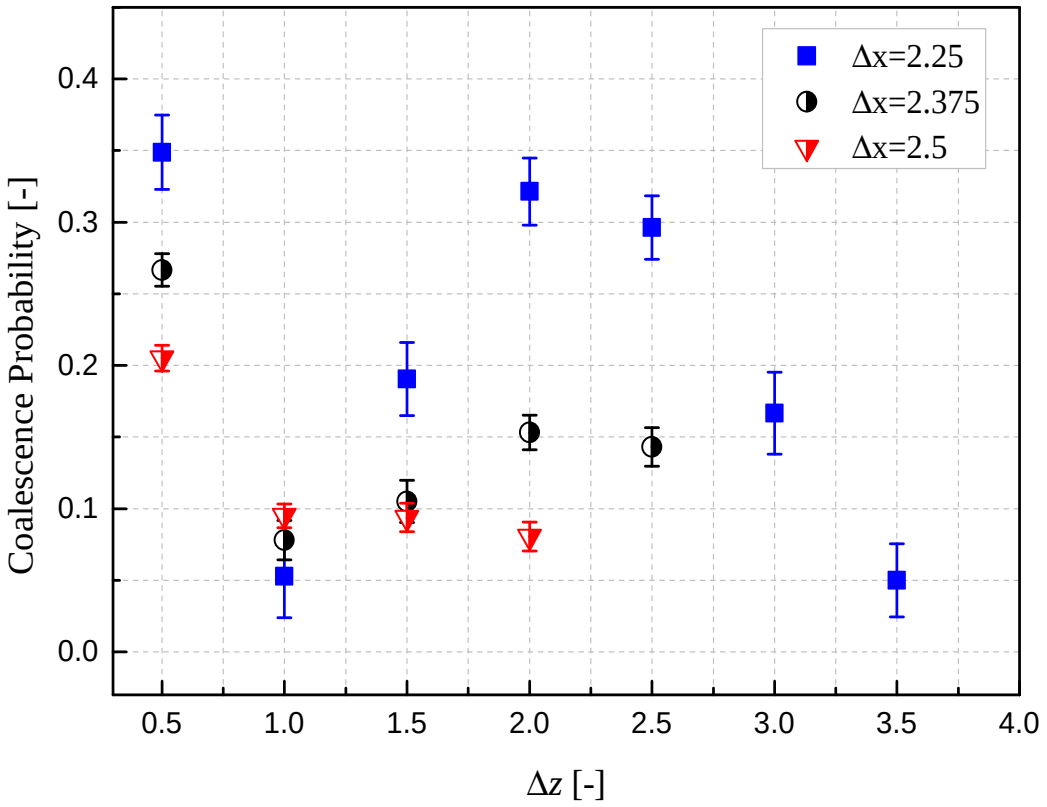


Figure 6.2: Coalescence probability from set of the three nozzles used in this study, the error bars represent the standard error which relates the standard deviation to the sample size.

Figure 6.3 shows a sketch for these expected scenarios that a trailing bubble could experience while it rises in the vicinity of the wake of a leading bubble.

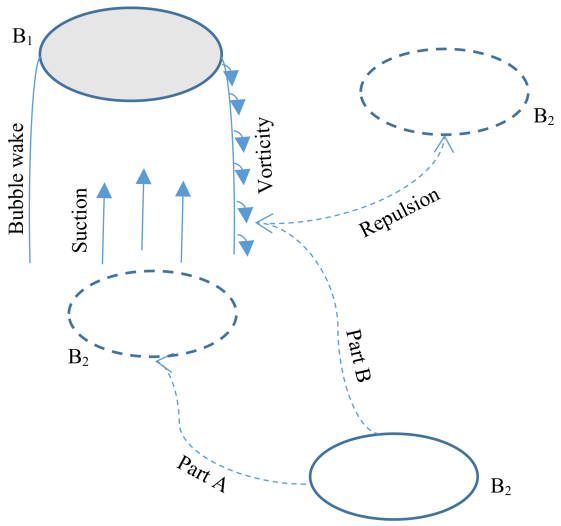


Figure 6.3: Sketch showing the expected scenarios that a trailing bubble could experience when it travels nearby the wake of a leading bubble.

An appreciable increase in the coalescence probability was noticeable for the smallest axial gap when the bubbles were within a vertical distance, $\triangle z$ close to 1.5. That was followed by a remarkable increase, especially for the smallest axial separation distance, $\triangle x$, when the bubbles separated by a non dimensional distance equivalent to 2. Here, the contribution of the vorticity of the leading bubble wake is still effective in drifting the trailing bubble but the difference is that the vertical distance between bubbles is large enough so that the trailing bubble would have approached the leading bubble. The approach could be because the size of the trailing bubble is smaller than the size of the leading bubble. As a result, the trailing bubble has the greater rise velocity which would have made the trailing bubble approaching the leading bubble. Afterwards, a drop down in the tendency of coalescence was gradually seen apart from $\triangle z$=2.



A similar trend was predicted for the next separation distance $\triangle x$=2.375. However, after the reduction in the coalescence probability at $\triangle z$=1, a moderate jump in the coalescence probability was observed compared to that at $\triangle x$=2.25. The reason here might be owing to the increase in the axial separation distance, $\triangle x$, between the bubbles. There were no coalescence events recorded when $\triangle z$ was larger than 2.5.

The behaviour for $\triangle x$=2.5 showed a different mode of coalescence probability where there was no jump in the behaviour after the reduction at $\triangle z$=1. The coalescence probability at that distance was even a bit greater than those for $\triangle x$=2.25 and 2.375. Apart from $\triangle z$=2, the likelihood of coalescence has dropped down again for all of the gaps.

It should be added here that the coalescence was not observed when larger axial separation distance, $\triangle x = 2.62$, was used.

The statement can be drawn here that the theoretical studies could be validated by the experiments even though the previous was based on small spherical bubbles.

6.3.2 Effect of relative bubble size

It is worth seeking another factor that might contribute to increasing or decreasing the coalescence probablity. The radii ratio of the trailing bubble to the leading bubble, r_2/r_1, was plotted against the average Reynolds number, Re_{ave}, of both bubbles. Striking results have been found when the ratio of the bubble sizes decreased below 1, the coalescence probability was highly increased. The reason

for that was previously discussed as in Section 5.3.1. These results are plotted in Figure 6.4.

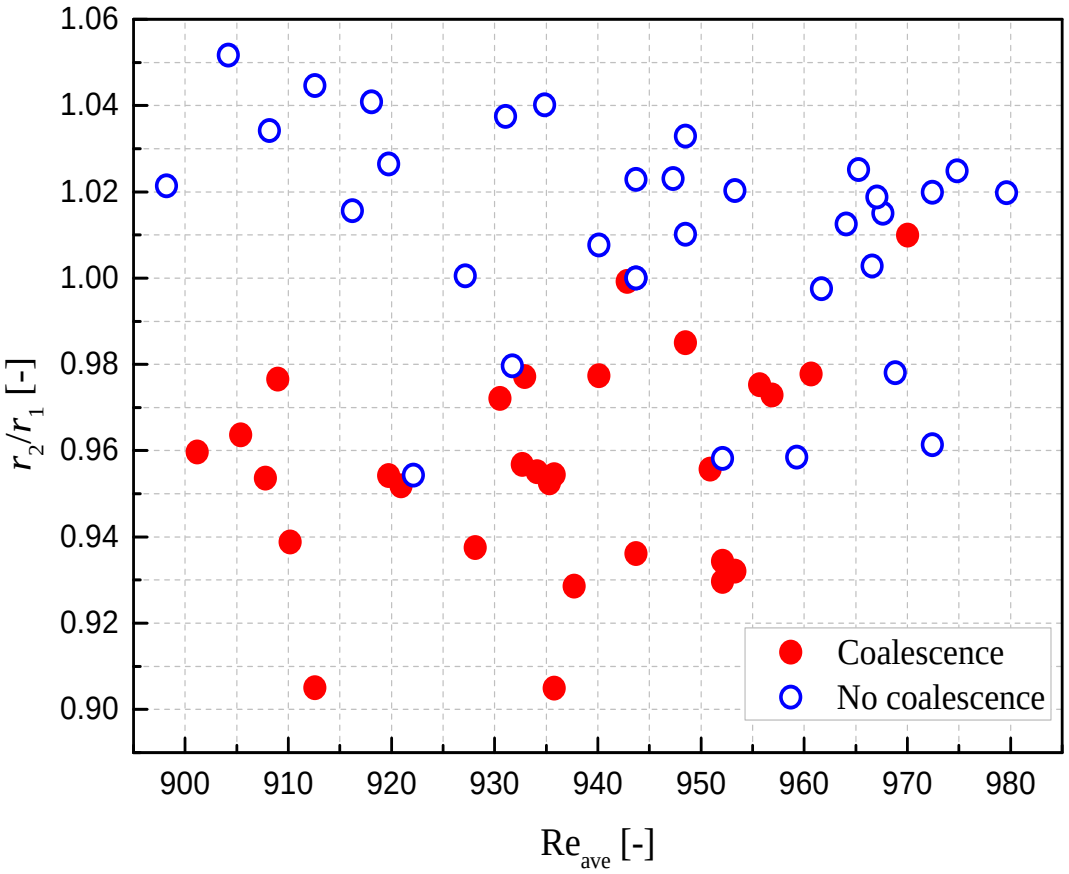


Figure 6.4: Effect of relative bubble size on the coalescence of bubbles when the trailing bubble is smaller than the leading bubble, there is a higher probability of coalescence.

Here, it is again the trailing bubble has the greater rise velocity which makes the trailing bubble approaching the leading bubble gradually until they row at an angle, $\theta_c, \leq 40^\circ$ and then they get coalesced. Similar graph was produced by Kusuno and Sanada (2015a) for spherical bubbles with $r \approx 0.5$ mm. Our findings are completely opposite to their findings owing to the different bubble sizes which for our study lie within the ellipsoidal regime. An ellipsoidal bubble is known to slow down because it develops a secondary motion (lateral motion). Hence, that

imposed the trailing bubble (smaller bubble) had greater average rise velocity compared to that of the leading bubble (larger bubble).

The encouraging finding is that the difference can be effective as it has been found that when the trailing bubble is appreciably smaller, even when $r_2/r_1 \simeq 2\,\%$, the coalescence is more likely to happen. However, if the trailing bubble has equal or larger size, the probability of coalescence of those bubbles is rare. This is explained by the negative gradient in the terminal velocity that an ellisoidal bubble has when its size is in the ellipsoidal range ($r \approx 0.7$-$2.5\,\mathrm{mm}$) as was shown in the general relationship between the terminal rise velocity and the bubble size in Clift et al. (1978).

It is also worth mentioning that the data showed in Figure 6.4 was captured at a vertical distance, $\triangle z$, larger than 2. That is to avoid the eventual deformation of the bubbles that could lead to coalescence although we know the higher contribution of the vorticity of the wake of the leading bubble in preventing the coalescence. The vorticity develops a drift force which would result in the trailing bubble to be quickly pushed away from the leading bubble.

The superimposed images and its corresponding 3D behaviours of two coalesced bubbles are shown in Figure 6.5a and Figure 6.5b, respectively. The trailing bubble is smaller than the leading bubble by $\approx 5\%$.

The trailing bubble, the smaller bubble, first travelled away from the leading bubble due to the developed drift force from the wake of the leading bubble as it was explained by Hallez and Legendre (2011). Then the bubbles, during their migration around each other, crossed each other and the trailing bubble continued

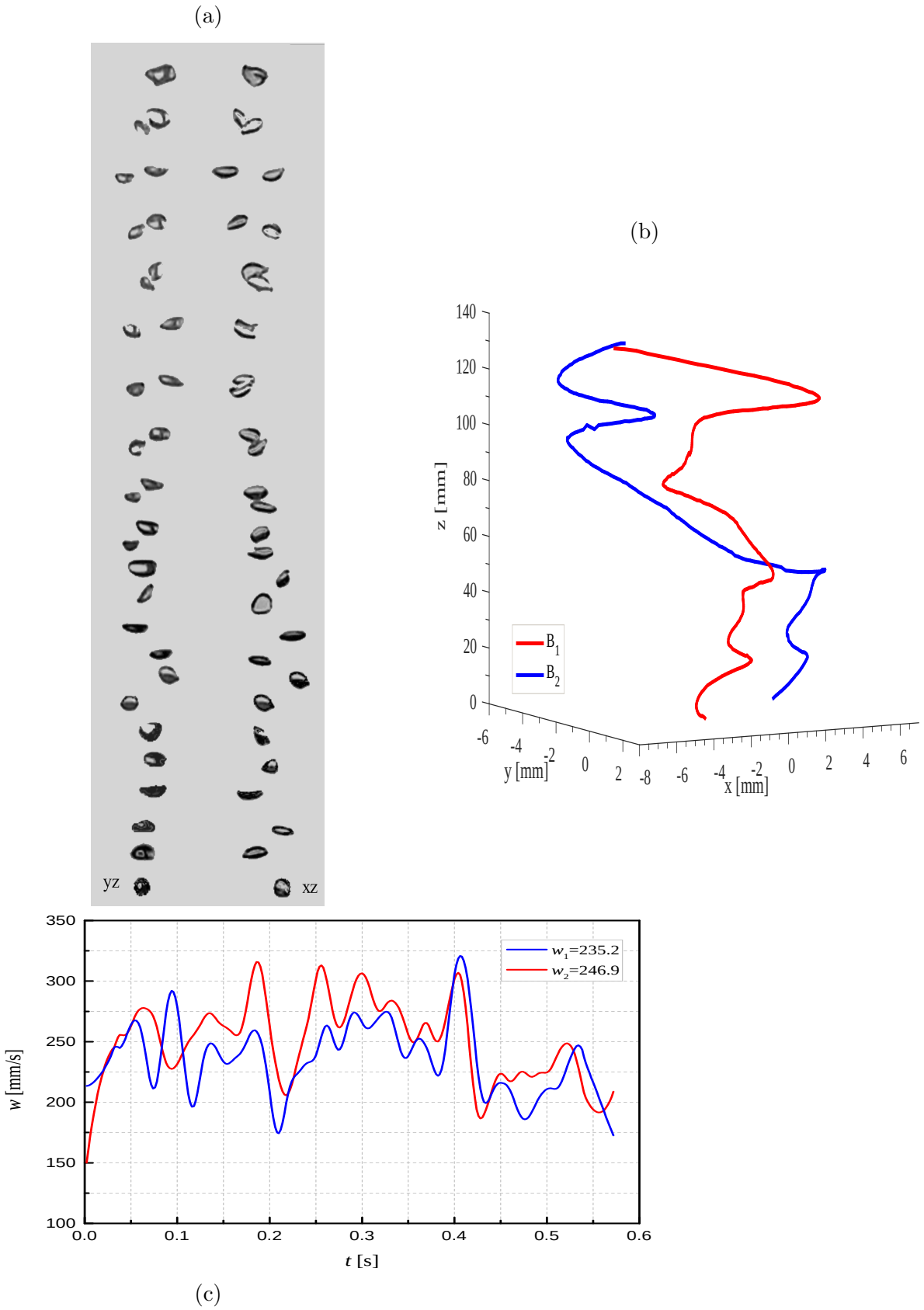


Figure 6.5: Relative motion of two coalescing bubbles, the trailing bubble is smaller than the leading bubble by 5 % (a) superimposition of frames in xz and yz planes showing the approach of the trailing bubble, (b) 3D trajectory of both bubbles, (c) rise velocity of both bubbles.

separating from the leading bubble at some places until it reached the leading bubble from the side and merged with it. That was the observation in most of the coalesced data points at offset configurations reported in this study. Figure 6.5c shows the instantaneous rise velocity of both bubble. This figure shows that the average rise velocity of the trailing bubble, $w2$ is greater than that of the leading bubble, $w1$, by $\approx 11\,\mathrm{mm/s}$. That slight difference might have drastically contributed to the coalescence process seen in Figure 6.4.

Next, the separation distance, s, was plotted against the coalescence angle, θ_c, the angle between the bubbles prior to the coalescence. The relationship is shown in Figure 6.6. Here, in the relation between θ_c and s, most of the data showed that the coalescence happened when the trailing bubble approached the leading bubble at $\theta_c \leq 40°$. This is consistent with our observations regarding the approach of the trailing bubble to the leading bubble based on its appreciably greater rise velocity. The contribution of the wake is seen less because the initial separation distance between the bubbles is small so that the trailing bubble would be more affected by the vorticity of the wake that push the trailing bubble away. The slight difference in the velocity of rise of the trailing bubble, also contributes in further decreasing of the distance separating the bubbles. The trailing bubble could return to the effective region of the wake where it can be caught by the wake of the leading bubble and therefore the coalescence happened. This scenario has low probability as it can be seen in Figure 6.6.

In Figure 6.6 also the relative interaction between the bubbles that is represented by the initial angle, θ_i, at the release is correlated against the separation

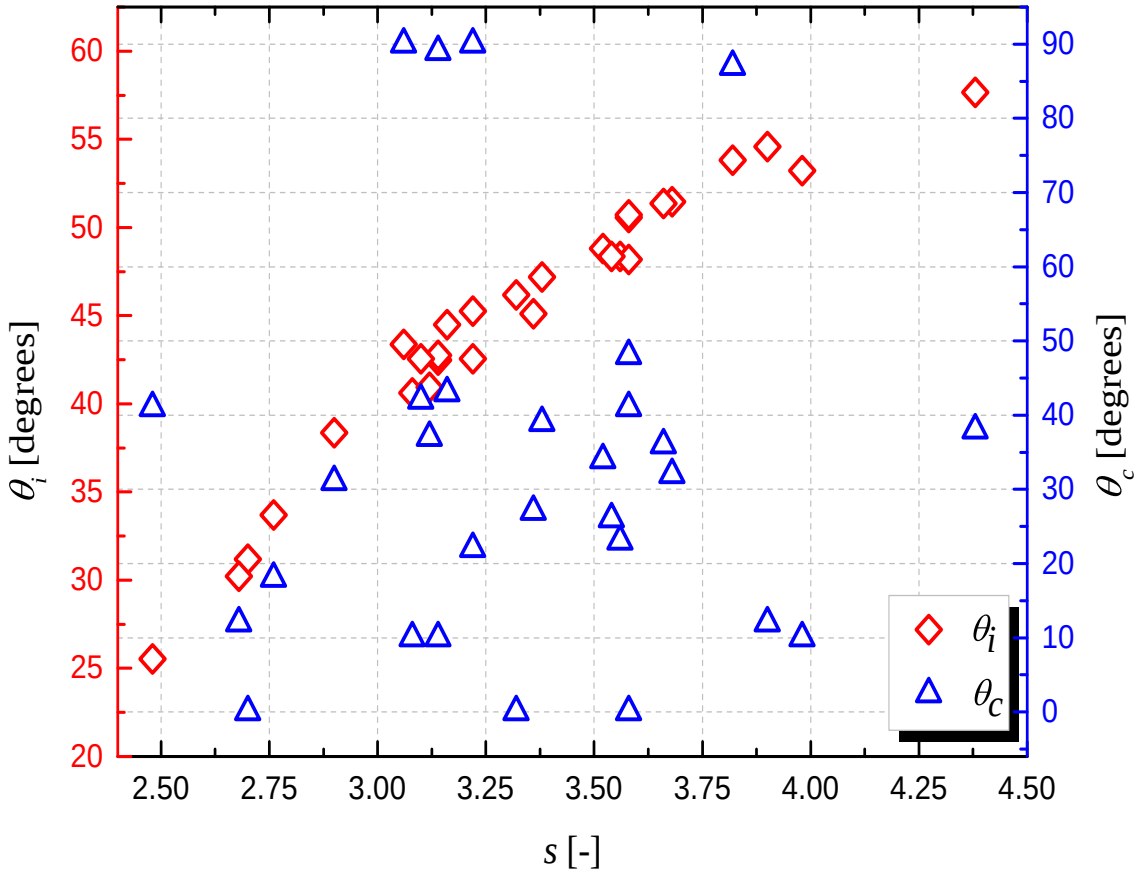


Figure 6.6: Initial and final interaction between the bubbles represented by the initial relative angle, θ_i, and the coalescence (equilibrium) angle, θ_c.

distance, s. This is important to show initial boundaries at which the coalescence is more likely to happen.

The bubbles are attracted to each other when they are in the range of $25.5\,^\circ < \theta_i < 57.6^\circ$. There is no previous study has identified these boundaries except the theortical work of Kok (1993a) which was for spherical bubbles using the potential flow theory. He found that the bubbles could coalesce if θ_i between them is $35\,^\circ < \theta_i < 54.7^\circ$. It seems that the ellipsoidal bubbles in our study do not deviate much from the findings of Kok (1993a) except a small deviation in the smallest angle, θ_i=25.5°. It should be noted that, at this angle, the coalescence between the

bubbles is rare.

It should also be referred to that the slight difference in the size of the rising bubbles could have played an important role in the enhanced probability of coalescence compared to the work of Kok (1993a) which was based on equally sized bubbles. More information on the spatial boundaries of the interaction of the bubbles will be deduced in the next section when validating the numerical simulations against the experiments.

In order to support our observations, a few experiments were conducted by generating a trailing bubble much smaller than the leading bubble. The trailing bubble produced at an equivalent radius equals to $r \approx 1.4\,\text{mm}$ by replacing the nozzle responsible for releasing the trailing bubble with a smaller one. One of the axial separation distance, $\triangle x$=2.25, studied here was tested. It was selected because it is considering the highest probability of coalescence. Two examples of coalescence are shown in Figure 6.7 which shows the superimposed evolution for the bubbles before and after the coalescence. In the first example in Figure 6.7a, the centre to centre separation distance between the bubbles, s, is 3.4 ($\triangle z$=2.5). These parameters were normalised by the radius of the leading bubble, r_1. The behaviour of the trailing bubble is interesting here where, in addition to its approach of the leading bubble from the side, it has overtaken the leading bubble which then caught the trailing bubble and merged with it. This behaviour can be considered due to the further increase in the rise velocity of the trailing bubble at this size.



(a) r_1=1.88 mm, r_2=1.39 mm



(b) r_1=1.85 mm, r_2=1.41 mm

Figure 6.7: Time evolution of two different sized bubbles.

In the second example, Figure 6.7b, the striking conclusion was that the trailing bubble approached the leading one and got coalesced with it at a larger

separation distance, s=6.9, which was almost double the distance over which the coalescence occurred when the slight deviation between the bubbles is within 10 %. The reason for that is the rise velocity of the trailing bubble is greater than that of the leading bubble which makes it possible for the trailing bubble to approach the leading bubble. It is also worth mentioning that it has been found that the probability of coalescence for these experiments was enhanced where 8 runs out of 20 showed coalescence. A quantification on the coalesced pairs is summarised in Table 6.1.

Table 6.1: Summary of coalescence parameters of additional experiments to test the effect of further deviation in bubble size ratio on the coalescence.

Coalescence	r_1 [mm]	r_2 [mm]	r_2/r_1 [-]	s [-]
yes	1.88	1.39	0.74	3.4
yes	1.85	1.41	0.76	6.9
yes	1.86	1.34	0.72	7.7
yes	1.91	1.39	0.73	8.2
yes	1.93	1.62	0.84	3.1
yes	1.86	1.52	0.82	3.6
yes	1.87	1.51	0.81	6.3
yes	1.89	1.49	0.79	6.6

Some of the experimental data that show both coalescence and no coalescence events is tabulated in Table 6.2. Similar parameters to those presented by Kok (1993b) have been reproduced.

Table 6.2: Summary of the important parameters of experimental results obtained.

Coal.	r_{ave} [mm]	s [-]	r_2/r_1 [-]	θ_i [deg.]	t_c [ms]	θ_e [deg.]	Coal.	s [-]	r_{ave} [mm]	r_2/r_1 [-]	θ_i [deg.]	t_c [ms]
yes	1.98	3.57	0.985	50.56	726	0	no	3.80	1.97	1.028	53.31	> 800
yes	1.99	3.81	0.975	53.81	658	87	no	4.21	1.96	1.023	57.08	> 800
yes	1.89	3.97	0.963	53.22	528	10	no	3.43	2.02	1.007	49.51	> 800
yes	1.90	3.56	0.938	48.35	472	23	no	3.51	2.02	1.025	50.71	> 800
yes	1.95	3.68	0.928	51.46	414	32	no	3.53	2.05	0.977	51.51	> 800
yes	1.97	3.65	0.936	51.37	468	34	no	3.97	2.03	1.019	55.95	> 800
yes	1.99	3.57	0.932	50.71	340	65	no	3.80	2.03	1.014	54.51	> 800
yes	2.02	3.05	1.00	43.36	556	79	no	4.02	2.03	1.040	56.62	> 800
yes	1.99	3.15	0.972	44.49	607	90	no	3.98	2.01	0.961	55.87	> 800
yes	1.98	3.21	0.934	45.25	546	22	no	3.10	1.98	1.012	43.03	> 800
yes	1.94	3.21	0.972	42.48	584	10	no	2.85	1.97	1.010	36.83	> 800
yes	1.89	3.14	0.976	42.55	610	90	no	3.10	1.92	1.000	41.06	> 800
yes	1.88	3.21	0.959	48.18	484	48	no	3.10	2.00	1.026	43.56	> 800
yes	1.94	3.58	0.977	42.75	646	86	no	2.78	2.03	1.04	37.32	> 800
yes	1.92	3.14	0.951	40.62	514	10	no	2.42	2.03	1.019	24.17	> 800
yes	1.92	3.08	0.954	57.67	454	38	no	2.84	1.99	1.024	37.32	> 800
yes	1.96	4.26	0.999	42.55	314	42	no	3.28	1.98	1.024	46.37	> 800
yes	1.96	3.10	0.974	46.18	714	0	no	3.37	2.02	0.958	48.63	> 800
yes	1.89	3.31	0.953	45.00	496	27	no	3.59	2.01	1.002	51.41	> 800
yes	1.98	3.35	0.929	54.59	622	12	no	3.06	2.02	1.018	43.23	> 800
yes	1.98	3.90	0.955	38.35	496	31	no	3.05	1.97	1.000	41.56	> 800
yes	2.01	2.89	0.977	25.54	534	89	no	3.08	2.00	0.958	43.23	> 800
yes	1.94	2.47	0.956	30.21	524	16	no	3.20	1.94	0.979	43.76	> 800
yes	1.95	2.67	0.904	33.69	332	18	no	3.11	1.92	0.954	41.28	> 800
yes	1.95	2.76	0.954	40.94	502	51	no	3.29	1.88	1.051	43.70	> 800
yes	1.98	3.12	0.955	31.18	456	0	no	3.20	1.93	1.00	43.56	> 800
yes	1.90	3.55	0.905	48.35	340	12	no	3.16	1.99	1.022	44.42	> 800
yes	1.93	3.52	0.937	48.85	402	46	no	3.22	2.01	1.032	46.10	> 800
yes	1.95	3.39	0.952	47.20	476	39	no	2.95	1.94	1.044	38.58	> 800
							no	2.76	1.89	1.021	30.68	> 800

A relationship, which is to the best knowledge of the author is shown for the first time, has been found when correlating the radii ratio and the time required for coalescence. This relationship, Figure 6.8, implies that the smaller the trailing bubble size is, the less the time required for the coalescence and vice versa.

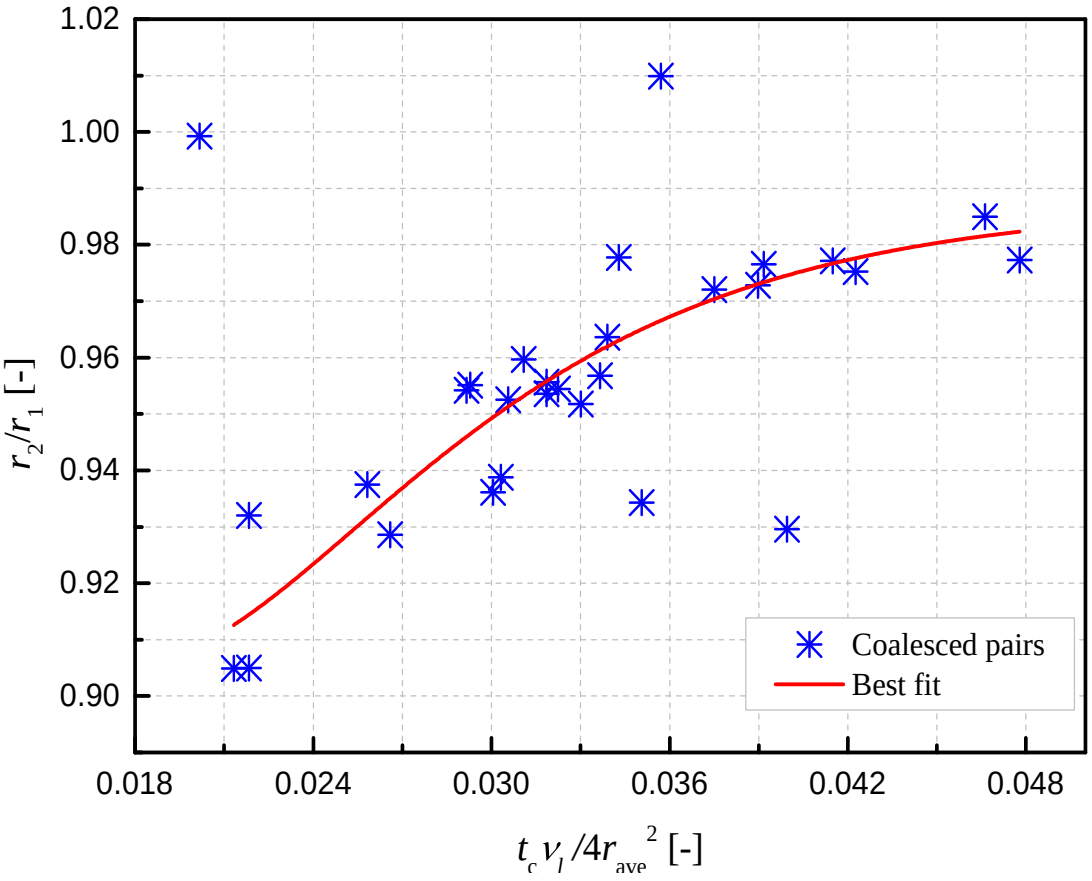


Figure 6.8: The nondimensionalised time delay before the coalescence of a pair of bubbles related to the initial bubble size ratio.

A general trend could be easily fitted to represent that behaviour even though a few points on the graph deviated from that trend. The deviation from the trend could be ascribed to another factor that is the separation distance, s, between the bubbles which is appreciably deviated at the initial release of the bubbles. However, any small separation distance, s, between the rising bubbles might have

been compensated by the greater average rise velocity of the trailing bubble.

For those pairs that did not show the coalescence, however, we are anticipating that the coalescence could be observed between them if the height of liquid in the test section is made larger than that we are investigating in the current research.

6.4 Numerical observations

Following the experimental results, we use the numerical simulations to study the effect of the slight deviation in the sizes on the coalescence of air bubbles rising in quiescent water. The simulations were carried out using Ansys-Fluent v150. The computational domain was generated to reflect the experimental test section except for the height which was restricted to 220 mm and the water level inside is maintained to 200 mm. Figure 6.9 shows the adaptive mesh region used and the configuration of the bubbles. The selection of the best mesh quality was tested as explained in Chapter 3 Section 3.2.3. The literature review on the grid independence, we found, for example, that 25 elements per radius were sufficient to make the difference in the rise velocity of a single bubble, identity of bubble shape, streamlines and recirculation region behind the bubble compared to experiments very small (Jan, 1994; Bunner and Tryggvason, 2002). Since tracking the coalescence events, particularly with the VOF model, requires very fine mesh, the computational resources were maximised by selecting the finest mesh that provides us with 22 grid points per radius (N_r). Hence, this resolution can be considered sufficient to provide accurate tracking for the coalescence of

bubbles.

The configuration of the bubbles will be restricted between θ_i=0° (bubbles rising side by side) and θ_i=90° (bubbles rising in line). Many simulations were carried out using our developed adaptive mesh method to cover different sizes of trailing bubbles and at different initial axial separations and centre to centre separations. Those simulations were also used to generalise a map for the boundaries at which the coalescence might occur and in comparison with experiments.

To test the validity of the numerical simulations against the experiments, three cases of simulations representing three different classes of trailing bubble sizes were done. The conditions for the calculations were set with the following physical parameters: ρ_l=998 kg/m^3, ρ_g=1.225 kg/m^3, μ_l=0.001 N.s/m^2, μ_g=1.8×10^{-5} N.s/m^2 and σ=0.072 N/m.

The validity of the numerical approach against the experiments in capturing the effect of the slight difference in bubble sizes was first investigated using three cases. Table 6.3 lists the simulation parameters and the conditions for the test cases. All the bubbles in the simulation runs were initially placed having an axial separation, $\triangle x$, and centre to centre separations, s, 2.25 and 3.28, respectively.

Table 6.3: Summary of the simulation parameters for the investigated cases.

Case	s [-]	r_1 [mm]	N_r [-]	r_2 [mm]	N_r [-]
a	3.36	2	21.5	2	21.5
b	3.36	2	21.5	1.9	20.5
c	3.36	2	21.5	1.8	19.5

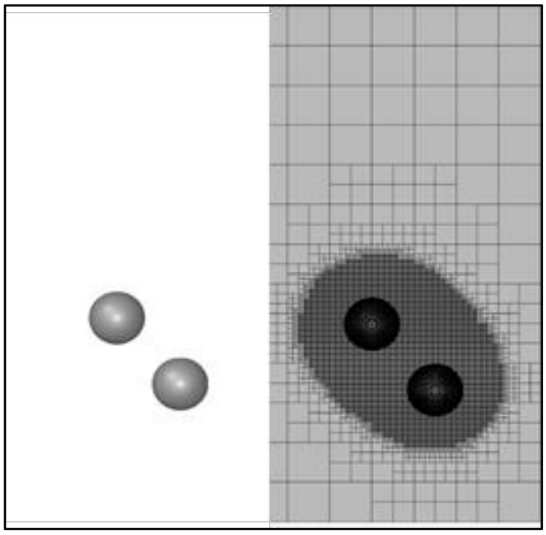


Figure 6.9: Bubbles configuration and adaptive mesh region.

Figure 6.10 shows the time evolution of the bubbles having three classes of bubble sizes. The case in Figure 6.10a shows that the equal bubbles did not coalesce. The bubbles have maintained a constant distance between each other rather than approaching each other. However, the other two cases in Figure 6.10b and c have shown coalescence when the trailing bubble size was smaller by 5 % and 10 % respectively of that of the leading bubble. This agreed well with the experimental findings in the previous section. Another aspect that can be observed from these simulations is the mode of coalescence, especially for the cases b and c described in Figure 6.10. They showed a difference in terms of the final orientation before the coalescence. When the bubbles deviated at 5% of their initial bubble sizes in Figure 6.10b, the coalescence happened at an angle, coalescence angle, θ_c, equal to 25°. For the case in Figure 6.10c in which the bubbles deviated at 10 %, the trailing bubble approached the leading bubble from the side and united with it. This would reflect the greater acceleration that the smaller trailing bubble in

case c had compared to that in case b. It is also an indication that the numerical approaches can detect the appreciable deviation in bubble sizes which is in an agreement with the experimental approaches. Table 6.4 presents a quantification for the three cases of the numerical simulations discussed in Figure 6.10 with the relevant experiments.

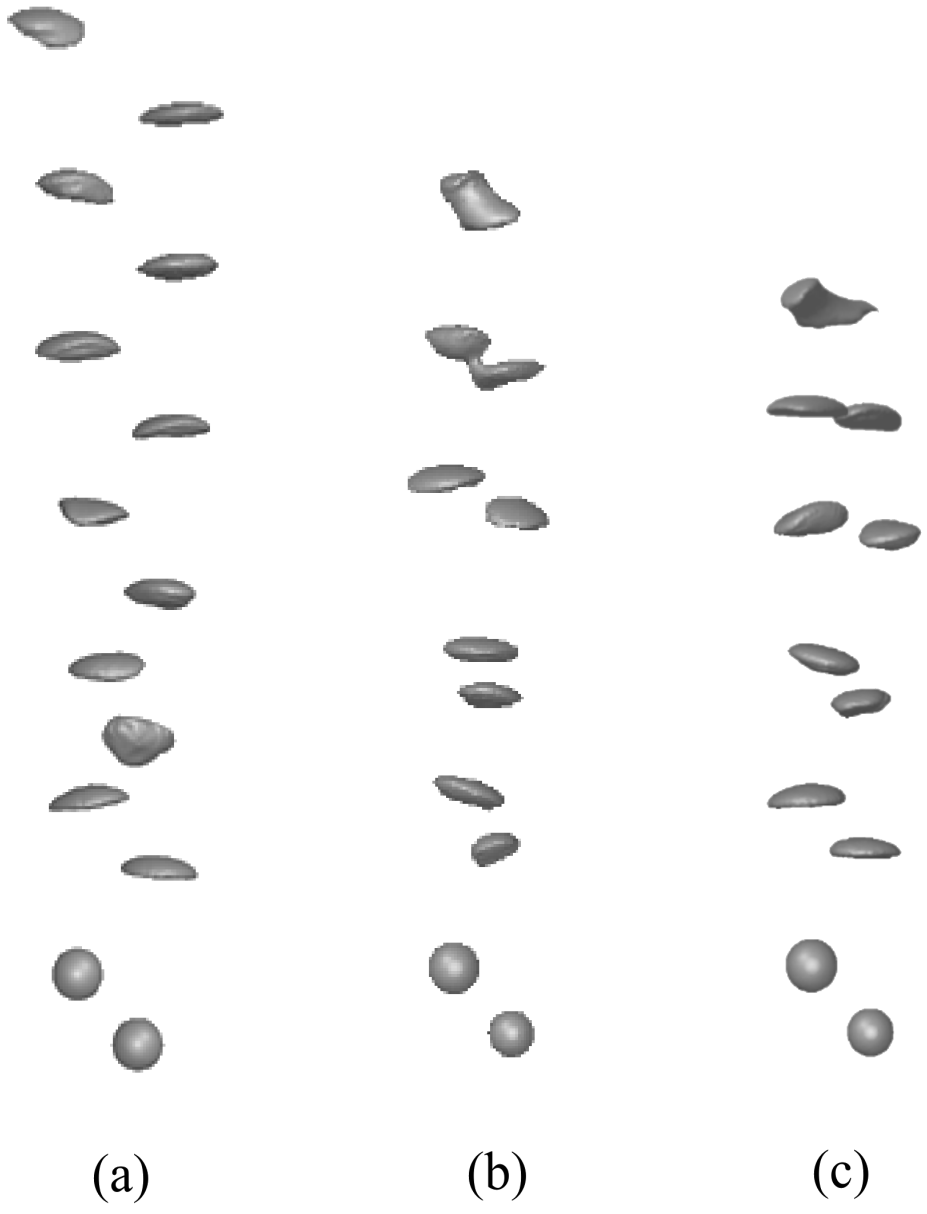


Figure 6.10: Tested three cases of deviation in rising bubble sizes (a) equal-sized bubbles, (b) the trailing bubble is smaller by 5 % (c) the trailing bubble is smaller by 10 %.

Table 6.4: Comparison of the parameters obtained from the numerical simulations with the experiments.

Case	Coalescence		Coal. distance [-]		Coal. time t_c [ms]	
	Exp	Sim	Exp	Sim	Exp	Sim
a	No	No	-	-	-	-
b	Yes	Yes	$69\,r$	$80\,r$	568	689
c	Yes	Yes	$48\,r$	$67\,r$	402	596

The experiments and numerical simulations agreed well when the trailing bubble is smaller than the leading bubble by 5 %. However, when the trailing bubble is smaller than the leading bubble by 10 %, a discrepancy of about 50% between both approaches is found. This high deviation could be considered due to the difference in release methods of bubbles in both the simulations and the experiments. It could also be the type and size of the mesh used in the simulations. It should be mentioned the nature of coalescence process of deformed bubbles is complex and the experiments showed a scatter for the time of coalescence with the size deviation.

Next, this study contributes to validate the numerical approaches in capturing the coalescence boundaries in comparison with the experiments. Based on this, a map for the disagreement between these boundaries can be generalised to be used as a guide for future work. It also tests the influence of the slight difference in bubble sizes as a whole on the coalescence process of a pair of deformable bubbles in a numerical frame. That was reached benefiting from our adaptive mesh model which facilitated testing many cases. The map was generated with different bubble classes with respect to the trailing bubble size.

The first class was generated when both bubbles have the same initial sizes. The second class of bubbles was when the trailing bubble had a smaller size than that of the leading bubble by 5 %. For the separation distances, since the axial distance, $\triangle x$, was maintained constant, the separation distance, $\triangle z$, was appreciably increased by 0.25 mm for the consecutive simulation runs. Once a bubble pair does not show the coalescence, the separation distance, $\triangle z$, is decreased to 0.125 mm between the bubble pair. Then, the simulation run will be repeated depending on the new $\triangle z$. Accordingly, 11 simulation runs were needed to generate the map. The coalescence map is shown here at the upmost boundaries at which the coalescence could happen. Then, this map was expressed by the normalised centre to centre separation distance, s, and the initial angle of interaction, θ_i, for a single axial separation distance used in the experiments, $\triangle x$=2.25. This map is shown in Figure 6.11.

It has been experimentally shown in Section 6.3.2 that the effect of the deviation in bubble sizes have a high impact on increasing the general tendency of coalescence. Thus, the numerical simulations emphasise the experiments as the unequally-sized bubbles showed coalescence at a distance increased for the axial separation tested. The probability of coalescence when the trailing bubble diameter is smaller by 5 % increased by 11 % compared to the equally sized bubbles. That probability would increase if the variation between relative bubble size is further decreased for instance to about 10 %. The map was then produced to relate our experimental boundaries. It has been found that the experimental effective region for coalescence is larger than that for the numerical simulations

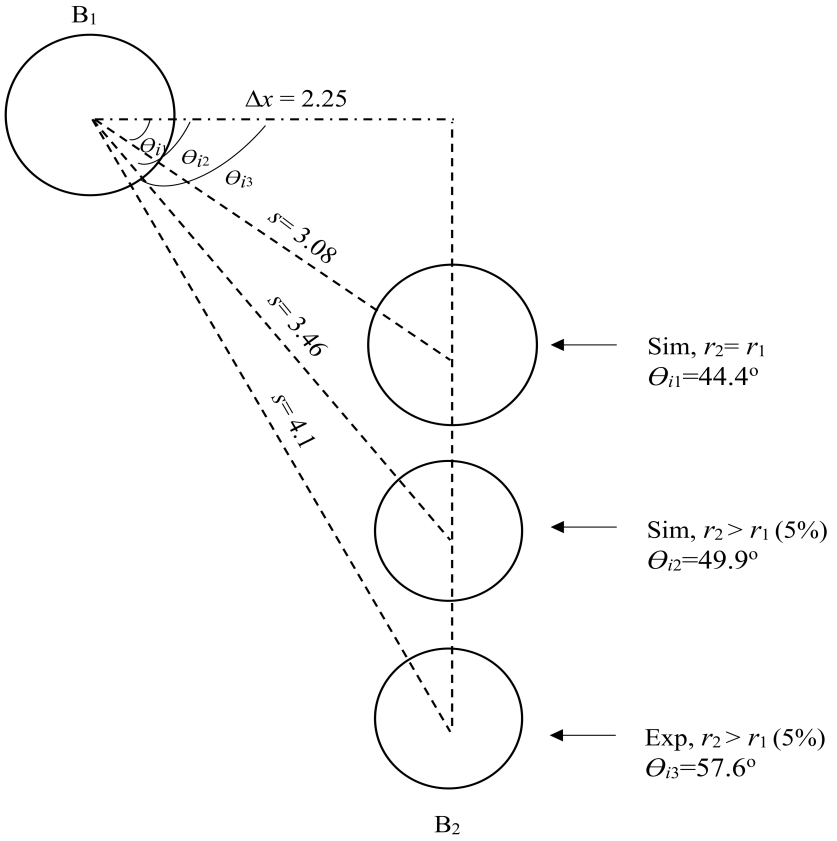


Figure 6.11: A map for the spatial boundaries of coalescence from the numerical simulations and the experiments. This map also shows the disparity between both results based on the change in the trailing bubble size.

of equal and unequal sized bubbles by 30% and 21%, respectively. This is owing to the difference of initial and boundary conditions between the experiments and the numerical simulations.

Overall, the findings here are of importance as they would improve the detectability of the numerical simulations in any future analysis of complex systems such as bubbly flows.

6.5 Characterisation of pairwise coalescence

6.5.1 Background

The characterisation of pairwise interaction is useful to parameterise the rise of many bubbles into the system. However, the parameterisation is not straightforward because neither the use of the analytical results nor the use of the computational studies could result in characterising bubble-bubble interaction of deformed bubbles. For example, many hundreds of simulations are required to construct such kind of quantitative model (Manga and Stone, 1995). Thus, the discussion in this section will be restricted to the use of our collected experimental data to achieve that scope. Since our experimental database consists of several bubble size variations, and also the interaction information, it will be used to quantitatively model the coalescence between the bubbles. Davis (1984) correlated the rate of bubble coalescence, J_{12}, Equation 6.1, with the relative bubble size, r_2/r_1, Eotvos number, Eo, and the capture radius of interaction, x_c, which is defined as the radius of the circle in which the rising bubbles trajectories locate. Figure 6.12 shows the horizontal separation distance between the bubbles, x_c.

$$J_{12} \approx n_1 n_2 \pi (w_2 - w_1) x_c^2 \left(\mathrm{Eo}, \frac{r_2}{r_1} \right) \tag{6.1}$$

where n_1 and n_2 are the numbers of bubbles of radius r_1 and r_2, respectively. $(w_1 - w_2)$ is the relative rise velocity of two bubbles. Zhang and Davis (1991) used Equation 6.1 to characterise the collision rate of small spherical bubbles due

to Brownian motion. Based on Equation 6.1, Manga and Stone (1995) introduced a functional form that related x_c^2 to Eotvos number and the relative bubble size. This functional form is given in Equation 6.2:

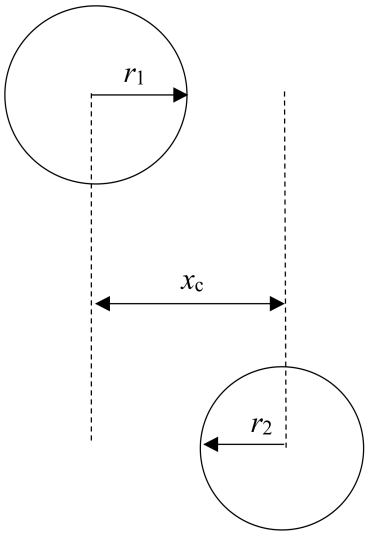


Figure 6.12: Schematic of the horizontal separation distance between the bubbles.

$$\frac{x_c^2}{(r_1+r_2)^2} = 0.3\left(\frac{r_2}{r_1}\right)^{0.5} + \frac{1}{2}\mathrm{Eo}\left(\frac{r_2}{r_1}\right)^{6} \tag{6.2}$$

Their model agreed well with the experimental data of the rising of air bubbles in corn syrup. In summary, few studies have investigated quantifying the coalescence of bubbles with the deviation in bubble sizes. Thus, the next section will characterise the boundary that separates the coalescence likelihoods according to bubble size deviation.

6.5.2 Model construction

It should be noted here that the cross section, x_c, can be equivalent to the initial axial separation distance between the bubbles after the release of both bubbles. In

addition, the initial vertical separation, $\triangle z$ should be sufficiently large in order to characterise the coalescence here. Referring to the abovementioned correlations, we shall consider the following functional relationship and seek any further appropriate modifications:

$$\frac{x_c^2}{(r_1+r_2)^2} = k\left(\frac{r_2}{r_1}\right)^q \tag{6.3}$$

where q should be negative since our bubbles arrangments are compeltely opposite to the setup of Manga and Stone (1995) where their largest bubble was the trailing bubble. It is also shown from our experiments that the trailing bubble controls the coalescence of bubbles by approaching the leading bubble due to its greater rise velocity. Thus, the cross section of coalescence, x_c, is inversely related to the relative bubble size. In order to determine the coefficients k and q, the regression analysis was applied to the experimental data of the largest axial separation distance at which the coalescence happened, $\triangle x$=2.5. Therefore, the resulted model can be given by:

$$\frac{x_c^2}{(r_1+r_2)^2} = 1.45\left(\frac{r_2}{r_1}\right)^{-3.71} \tag{6.4}$$

The experimental data that showed the coalescence and that did not show are plotted in Figure 6.13. All of the coalesced pairs in this figure fitted well to our model within an error margin of 5%. Additionally, it predicted the boundary determining the coalescence and non coalescence regions. The pairs that did not coalesce were mostly out of the coalescence region and they gradually approached

the boundary between the regions as their relative size largely deviated. Hence, further deviation in the relative bubble size could result in the coalescence between the bubbles. The model of Manga and Stone (1995), Equation 6.2, is also shown in Figure 6.13. Here, the equation was modified in order to fit our bubbles arrangement and is given by:

$$\frac{x_c^2}{(r_1+r_2)^2} = 0.3\left(\frac{r_2}{r_1}\right)^{-0.5} + \frac{1}{2}\mathrm{Eo}\left(\frac{r_2}{r_1}\right)^{-6} \tag{6.5}$$

here $x_c^2/(r_1+r_2)^2 \simeq 1$ corresponds to the vertical rise of bubbles with no hydrodynamic interaction between them. As can be seen that there is a good agreement between our model and the modified model of Manga and Stone (1995). Nevertheless, one could notice that the modified model of Manga and Stone (1995) has underestimated the capture radius as r_2/r_1 approaches 1. However, when the r_2/r_1 smaller than 0.9, there is a great disagreement between our model and the modified model of Manga and Stone (1995). This could be because the model of Manga and Stone (1995) was based on experimental data of high viscous liquid (corn syrup).

Next, the rate of coalescence, J_{12}, was calculated using the model described by Equations 6.3 and 6.4. The average rise velocity of a single bubble, w, was used to non dimensionlise J_{12}. Since we restrict our model to the rise of two bubbles, n_1 and n_2 take the value of 1. The results are shown in Figure 6.14. The smaller the relative size r_2/r_1, the higher the rate of coalescence is predicted. No coalescence is predicted in Equation 6.1 as r_2/r_1 approaches 1. This is because

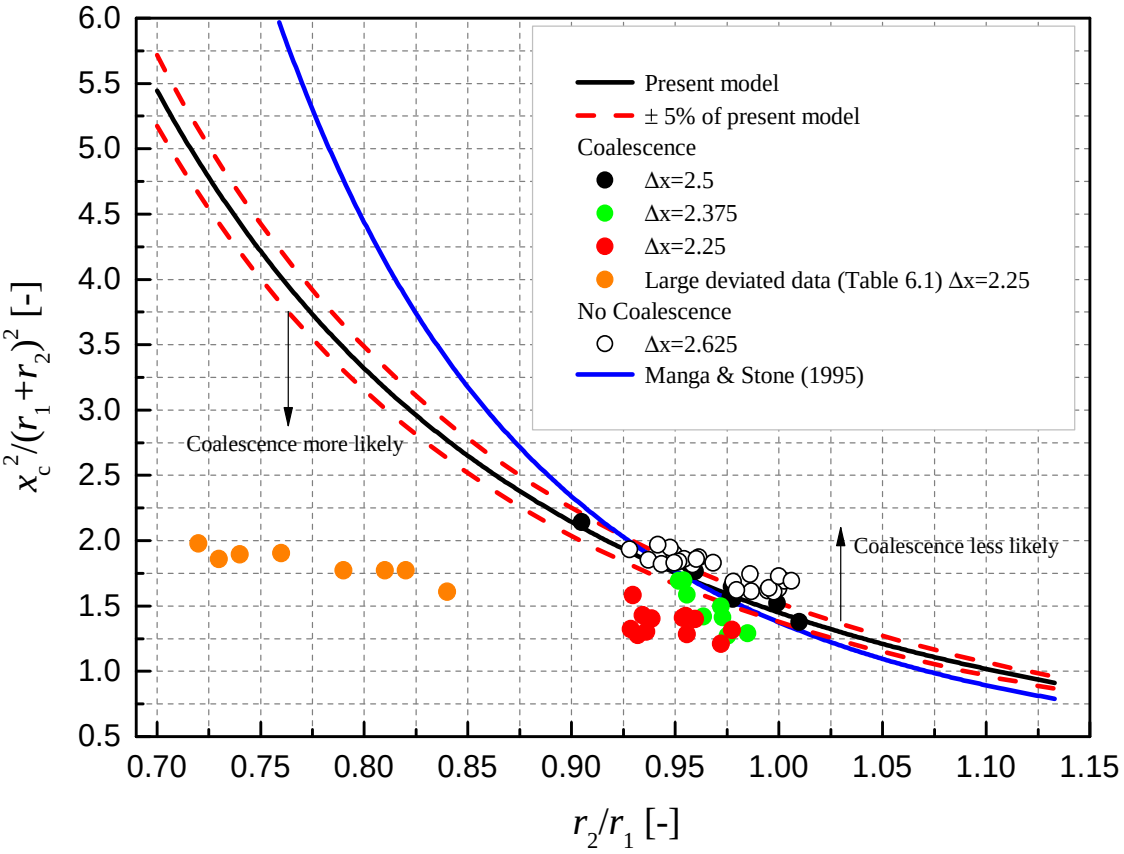


Figure 6.13: Comparison between the suggested model and the experimental data.

the relative velocity of the bubbles, $(w_2 - w_1)$ will approach 0. However, the deformation of the equally-sized bubbles could result in the eventual coalescence (Manga and Stone, 1993). Hence, the rate of coalescence plotted in Figure 6.14 could be underestimated when $r_2/r_1 \longrightarrow 1$.

Indeed, there is no available data in the literature to compare with the model of coalescence rate. Thus, the additional experiments that were shown in Table 6.1 were used for comparison. The velocity of the bubbles was considered depending on the average radius of the rising bubbles. This data has well agreed to the coalescence rate model, J_{12}. In addition, the simulation cases when the trailing bubble was smaller by 5 % and 10 % were also used. The simulation data also

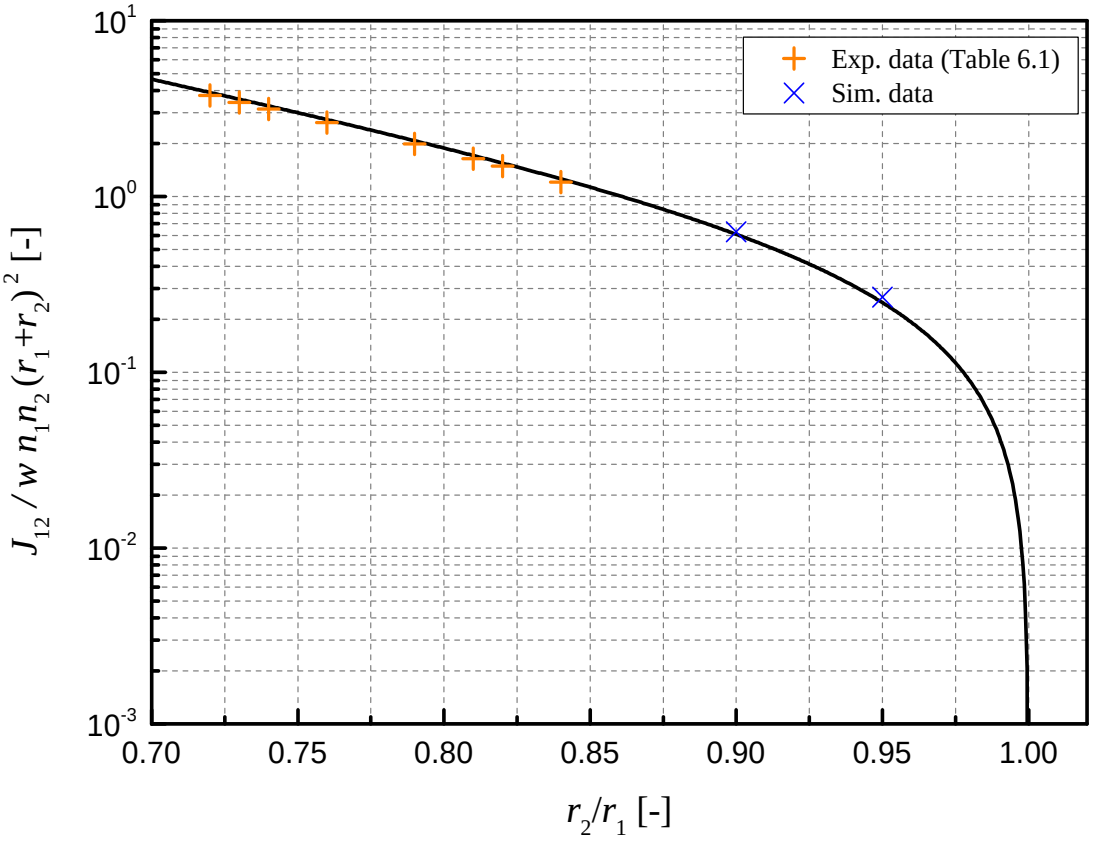


Figure 6.14: Dimensionless rate of coalescence based on Eq. (6.4) and the model of Davies (1984).

well fitted to our coalescence rate model with a little bit overestimation. This could be because of the velocity calculated from the simulation deviates from the experiments by $\simeq 6\,\%$.

6.6 Summary

This chapter contributed to providing a useful database for the coalescence of a pair of deformed air bubbles in water. An insight has been provided about the likelihood of coalescence events that two nozzles could generate in a system of different bubble configurations. The observations were agreed with the theoretical work reported by others though their work was based on spherical bubbles interaction. Then, the factors that promote the coalescence of bubbles were investigated. It has been found that when the trailing bubble was slightly smaller than the leading bubble, an increased number of coalescence events were recorded. That was ascribed to the appreciable increase in the rise velocity of the trailing bubble compared to the leading bubble. Additionally, the time required for coalescence was generally related to the deviation in bubble sizes.

The numerical validation for the experiments was tested using the corresponding model for cases of equal and different sized bubbles. It has well predicted the effect of the deviation in size on the pairwise coalescence of bubbles.

Then, the difference between the experiments and the simulations regarding the effective region over which the bubble might coalesce were highlighted. Hence, this chapter introduced a map to show the general disparity between the numerical simulations and the experiments so that it would establish a ground for further progress on bubbly flow modelling.

Finally, a quantitative model to determine the coalescence boundaries has been presented. The model then was qualitatively compared to a previous model

and good agreement was achieved. Enhancement of coalescence was noticed as the bubble size ratio decreased. Depending on the proposed model, the rate of coalescence was also correlated with the relative bubble size. The experiments and the simulation data fitted well to the coalescence rate model.

7

CONCLUSIONS AND RECOMMENDATIONS

This chapter highlights the main conclusions form this study and the related recommendations for further work which have not been covered during the study.

7.1 Conclusions

There is unanimous agreement that the proper modelling of multiphase flow systems is far from complete although much work has been done. This is due to the difficulty that these systems present in terms of, for example, jumps in density and viscosity and the effect of surface tension. Furthermore, the lacking of experimental data that are necessary to proceed with perfection of the modelling especially when the system assumes interaction between bubbles. This motivated the work conducted in the present Thesis. The bubble dynamics, the interaction of bubbles and the coalescence of bubbles were experimentally and numerically studied in Chapters 4, 5 and 6 respectively. Many numerical simulations were planned firstly to be done in this research with high accuracy and secondly to model complicated problems such bubble-bubble interaction.

In Chapter 3, a new adaptive mesh technique was developed to track the bubbles. The technique uses the ANSYS-Fluent software with the standard multiphase model, the Volume of Fluid (VOF) method. In order to achieve a desirable level of refinement of the mesh around the bubbles, the standard refinement/coarsening algorithm in Fluent is used. However, to mark the region around the bubbles that needs to be refined, a scalar Lagrangian equation is solved where a source of the scalar is applied inside the bubbles while at the walls of the domain, a Dirichlet condition is used where the scalar is fixed at zero. The mesh is then refined in the region where the scalar is greater than one quarter of its maximum value. As the bubbles rise, the scalar equation is repeated solved and so the refinement region is automatically modified around the bubbles with little appreciable increase in the number of cells in the mesh. This technique was tested and verified against two numerical examples and the rise of single bubble. In comparison with a fixed mesh, the developed model reduced the computational cost required to model the rise and the coalescence of two bubbles compared to fixed mesh simulations. In addition, the accuracy of the model in capturing similar topology was demonstrated. The discrepancy in the rise velocity of a single bubble using a fine mesh was found to be about 6% compared to the experimental value.

In Chapter 4, the dynamics of single bubble rising were investigated. It has been showed that the zigzag path is dominant in our moderate bubble sizes. Over the two sizes of bubbles compared against each other, appreciable increase in the shape deformation was observed for the larger bubble size, r=2.57 mm,

compared to the smaller one, r=1.6 mm. Both bubbles compared in this study were experimentally tilted at the same angle. While, the frequency of orientation predicted by the VOF method was over estimated by 25%. In addition, the frequency of bubble deformation is also higher than that obtained by the present experiments. The experiments have demonstrated that the frequency of the bubble rise velocity had the same frequency of bubble shape oscillation and twice the frequency of the path oscillation. This could imply that there is an interaction between the bubble motion and its shape instability. On contrary, such kind of interaction was not observed using the CFD method. This different behaviour predicted by the VOF method might lead to different flow and drag encountered by the bubble.

In Chapter 5, the interaction of bubbles at large separation distances was investigated. This chapter closely described the effect that each bubble brought to its counterpart when they rose at different configurations. It has been found that the slight deviation in the relative bubble size led to the trailing bubble, which was appreciably smaller, approaching the leading bubble, while the pair of the bubbles was found to be separating vice versa. This achievement was supported by statistically small sets of bubbles rising side by side. These sets showed that the smaller bubble preceded the larger bubble although there was inconsistency between the final separation distance and the relative size of the rising bubbles. It was also highlighted that equilibrium distance found in case non deformable bubbles either did not exist or shortened for our deformable bubbles. Furthermore, the effect of wake of the leading bubble on the trajectory of the trailing bubble

was discussed. The results showed that strong interaction between the bubbles was found when the centre to centre distance, s, was small and this interaction became gradually lighter when s was larger than 6. The numerical simulations in this chapter also provided a justification to the experiments whereas the relationship between the relative bubble and the approach of the trailing bubble to the leading bubble was shown using three cases in which the trailing bubble size was equal to the size of the leading bubble in the first case and deviated at 5% and 10% for the second and the third cases respectively.

In Chapter 6, the coalescence of bubbles as a result of the interaction between the bubbles at small separation distances was investigated. The coalescence probability per each nozzle used was quantified showing the rejection effect on the trailing bubble if it was located at a vertical distance close to 1. Then the coalescence probability increased apart from that. The slight deviation in the trailing bubble size played a significant role in increasing the tendency for coalescence between bubble pairs. This is considered to the appreciable increase in the rise velocity of the smaller bubble, trailing bubble, adding to that its existence in the wake region of the leading bubble, as a result the trailing bubble accelerated until approached the leading bubble and coalesced with it. To support this finding, few experiments were conducted in which further reductions in the trailing bubble size were planned. They showed an enhanced coalescence of bubbles and even the initial distance between the bubbles was found to be doubled. A new relationship between the time required for coalescence and the relative bubble size was pointed out which was found that the time required for coalescence decreased

as the bubble size ratio increased. The numerical analyses in this chapter also showed an increased tendency of coalescence of bubbles as the trailing bubble was smaller. A map showing the discrepancy between the numerical simulations and the experiments in terms of the boundaries at which the coalescence might occur. This map was based on that the trailing bubble size was smaller than the leading bubble size by 5%.

Finally, a characterisation model for the spatial boundaries of coalescence with the relative bubble size was presented. The constructed model is simple and it correlated the most important parameters affecting the coalescence of bubble based on previous observations of others. That was done by using the least square method to fit the present experimental data of the coalescence at the largest separation distance. The model has well modelled the boundaries between the coalescence and the no coalescence region compared to the present experimental and previous model. Then, the non dimensional rate of coalescence as a function of the relative bubble size was also presented. The rate of coalescence is largely governed by the bubble size ratio, which decays as the relative bubble size, r_2/r_1, approaches 1.

7.2 Recommendations

Number of avenues are still not covered by the researchers numerically or experimentally into the study of bubble-bubble interaction dynamics.

Further to the work presented in Chapter 5, models that can account for the drag coefficient of deformable bubble should be investigated whereas there

is only models for drag calculation for interaction of spherical bubbles. For the experiments, the present data in Chapter 5 or Chapter 6 can be used to find the drag coefficient of the both leading and trailing bubble. For the numerical analyses, since the drag coefficient can not be calculated directly, the pressure field around each bubble, more specifically the trailing bubble, should be extracted first before calculating the drag force. Some of the previous equations available for calculating the drag coefficient of single deformable bubble could be of use such as Equations 2.16-2.18 to construct the model of the trailing bubble.

The effect of the wake of the leading bubble on the trailing bubble is considered as an ongoing demand for research and should be addressed. The problem of experimentally getting contours for the wake region is not straightforward as most of the techniques require to inject a dye inside the liquid which could change the physical properties of that liquid. The PIV technique, however; can be an alternative although low concentration of particles is injected in the liquid. Since the PIV captures the structures in single 2D plane, few adaptations are necessary to get structures in two or more of 2D planes. The work of Brücker (1999), for example, who used two PIVs and set of mirrors to track the 3D behaviour of single bubble.

Another area could be covered in relation to the work presented in Chapter 6 related the presented model for the coalescence of bubbles. Numerically, there is possibility to construct semi empirical model depending on available stochastic models for coalescence that are introduced into Lagrangian-Eulerian model. Based on that few thousands of bubbles can be modelled. Using a User Defined

Function, some assumptions can be considered such as defining an effective distance at which the bubbles are very close and therefore they can be recorded as coalesced bubbles.

Finally, a coalesced bubble is known that it slows down and experiences a volume and surface area. The magnitude of slowing down and the expansion of volume and the surface area should be studied. There have been some experiments that have investigated such kind of dynamics. However, similar numerical investigation has not been done. The process of tracking each individual bubble is a bit challenging because there are two bubbles and both of them are labelled as air phase. Thus, to accomplish this, we suggest here to use the Species model in Ansys-Fluent. In this model, a mixture of two air phases are introduced. There is another advantage for using the Species model that we can track the mixing inside the bubble after the coalescence. This might be useful in some applications such as microfluidic reactors. An example of successful modelling using the Species model is shown in Figure 7.1. Again the adaptive mesh technique is necessary here to track the bubbles before and after the coalescence. Different configurations of bubbles can be modelled using the Species model mixed with the adaptive mesh method.

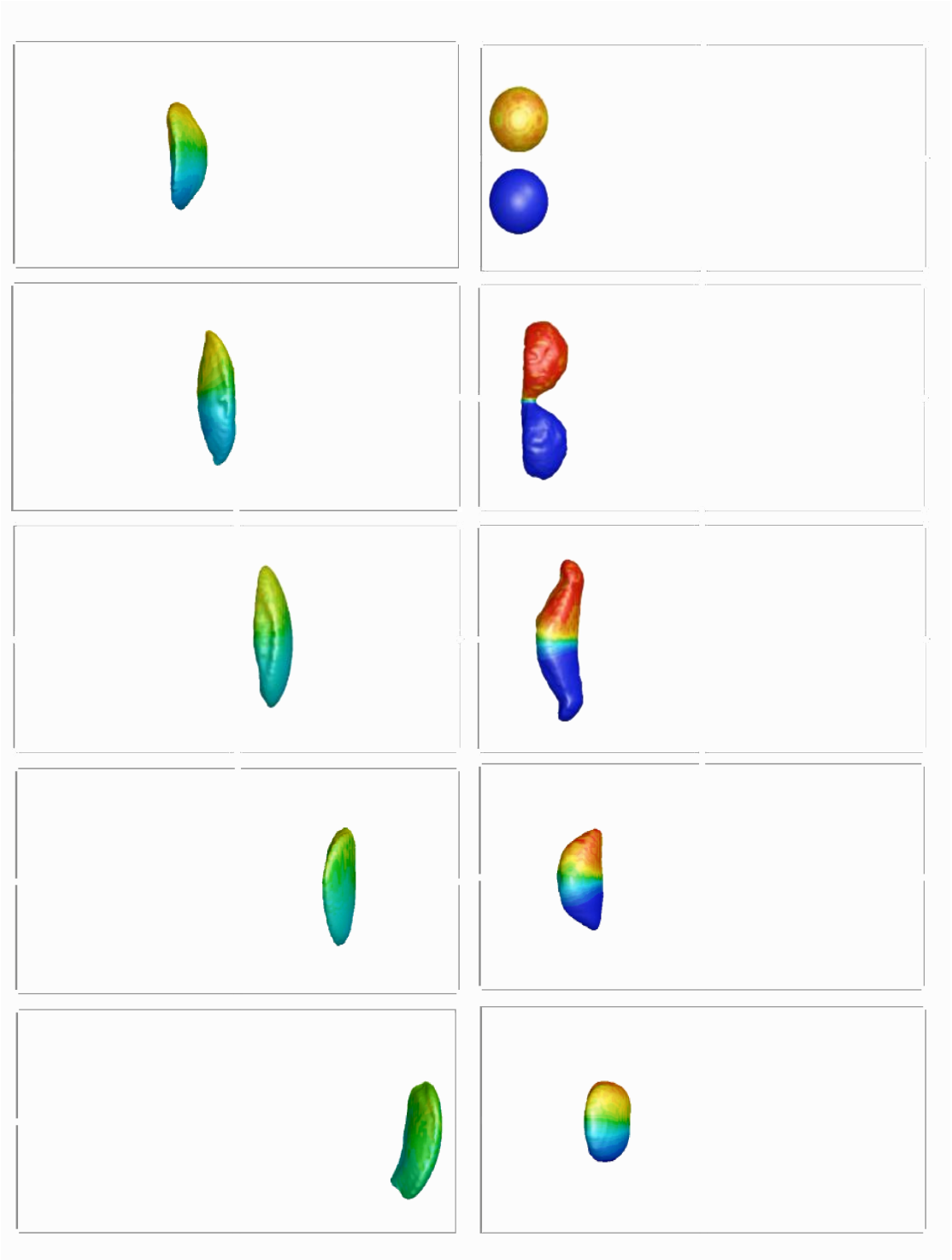


Figure 7.1: An example showing bubbles rising side by side modelled using Species model in Ansys-Fluent.

BIBLIOGRAPHY

AIAA. Guide for the verification and validation of computational fluid dynamics simulations. *Technical Report AIAA-G-077-1998, American Institute of Aeronautics and Astronautics Reston, VA*, 1998.

A. S. Almgren, J. B. Bell, P. Colella, L. H. Howell, and M. L. Welcome. A conservative adaptive projection method for the variable density incompressible navier–stokes equations. *Journal of Computational Physics*, 142(1):1–46, 1998.

T. Auton. The lift force on a spherical body in a rotational flow. *Journal of fluid Mechanics*, 183:199–218, 1987.

N. Aybers and A. Tapucu. Studies on the drag and shape of gas bubbles rising through a stagnant liquid. *Wärme-und Stoffübertragung*, 2(3):171–177, 1969.

P. Bagchi and S. Balachandar. Shear versus vortex-induced lift force on a rigid sphere at moderate re. *Journal of Fluid Mechanics*, 473:379–388, 2002.

S. A. Baz-Rodríguez, J. Ramírez-Muñoz, A. Soria, and J. C. Sacramento-Rivero. Hydrodynamic interaction of two spherical bubbles rising in-line: A semi-analytical approach. *Chemical Engineering Communications*, 201(5):674–687, 2014.

A. Biesheuvel and L. Van Wijngaarden. The motion of pairs of gas bubbles in a perfect liquid. *Journal of Engineering Mathematics*, 16(4):349–365, 1982.

J. Blazek. *Computational Fluid Dynamics: Principles and Applications: Principles and Applications*. Elsevier, 2001.

J. Brackbill, D. B. Kothe, and C. Zemach. A continuum method for modeling surface tension. *Journal of Computational Physics*, 100(2):335–354, 1992.

C. Brücker. Structure and dynamics of the wake of bubbles and its relevance for bubble interaction. *Physics of fluids*, 11(7):1781–1796, 1999.

B. Bunner and G. Tryggvason. Dynamics of homogeneous bubbly flows part 1. rise velocity and microstructure of the bubbles. *Journal of Fluid Mechanics*, 466:17–52, 2002.

I. B. Celik, U. Ghia, P. J. Roache, et al. Procedure for estimation and reporting of uncertainty due to discretization in CFD applications. *Journal of Fluids Engineering-Transactions of the ASME*, 130(7), 2008.

P. Chen, J. Sanyal, and M. Dudukovic. CFD modeling of bubble columns flows: implementation of population balance. *Chemical Engineering Science*, 59(22):5201–5207, 2004.

A. Chesters and G. Hofman. Bubble coalescence in pure liquids. In *Mechanics and Physics of Bubbles in Liquids*, pages 353–361. Springer, 1982.

R. Clift, J. Grace, and M. Weber. Bubbles, drops and particles. *Academic Press, New York*, 1978.

C. Crowe, T. Troutt, and J. Chung. Numerical models for two-phase turbulent flows. *Annual Review of Fluid Mechanics*, 28(1):11–43, 1996.

M. Dai and D. P. Schmidt. Adaptive tetrahedral meshing in free-surface flow. *Journal of Computational Physics*, 208(1):228–252, 2005.

R. H. Davis. The rate of coagulation of a dilute polydisperse system of sedimenting

spheres. *Journal of Fluid Mechanics*, 145:179–199, 1984.

A. de Vries, A. Biesheuvel, and L. Van Wijngaarden. Notes on the path and wake of a gas bubble rising in pure water. *International Journal of Multiphase Flow*, 28(11): 1823–1835, 2002a.

A. W. G. de Vries. *Path and wake of a rising bubble*. University of Twente, 2001.

J. de Vries, S. Luther, and D. Lohse. Induced bubble shape oscillations and their impact on the rise velocity. *The European Physical Journal B-Condensed Matter and Complex Systems*, 29(3):503–509, 2002b.

E. Delnoij, J. Kuipers, and W. Van Swaaij. Dynamic simulation of gas-liquid two-phase flow: effect of column aspect ratio on the flow structure. *Chemical Engineering Science*, 52(21):3759–3772, 1997a.

E. Delnoij, F. Lammers, J. Kuipers, and W. Van Swaaij. Dynamic simulation of dispersed gas-liquid two-phase flow using a discrete bubble model. *Chemical Engineering Science*, 52(9):1429–1458, 1997b.

D. A. Drew and S. L. Passman. *Theory of multicomponent fluids*. Springer, 1999.

G. Drogaris and P. Weiland. Coalescence behaviour of gas bubbles in aqueous solutions of n-alcohols and fatty acids. *Chemical Engineering Science*, 38(9):1501–1506, 1983.

P. Duineveld. Bouncing and coalescence of two bubbles in pure water. In *IUTAM Symposium on Waves in Liquid/Gas and Liquid/Vapour Two-Phase Systems*, pages 151–160. Springer, 1995a.

P. Duineveld. The rise velocity and shape of bubbles in pure water at high reynolds number. *Journal of Fluid Mechanics*, 292:325–332, 1995b.

P. Duineveld. Bouncing and coalescence of bubble pairs rising at high reynolds number in pure water or aqueous surfactant solutions. In *In Fascination of Fluid Dynamics*,

pages 409–439. Springer, 1998.

P. C. Duineveld. Bouncing and coalescence of two bubbles in water. *Ph. D. thesis, Twente University*, 1994.

K. Ellingsen and F. Risso. Measurements of the flow field induced by the motion of a single bubble. In *Proc. Third Intl Conf. on Multiphase Flow, Paper*, volume 286, 1998.

K. Ellingsen and F. Risso. On the rise of an ellipsoidal bubble in water: oscillatory paths and liquid-induced velocity. *Journal of Fluid Mechanics*, 440:235–268, 2001.

L.-S. Fan and K. Tsuchiya. *Bubble wake dynamics in liquids and liquid-solid suspensions*. Butterworth-Heinemann, 1990.

A. Fluent. Users guide 15.0. *Ansys Inc*, UDS Theory, 9, 2014.

F. Garner and D. Hammerton. Circulation inside gas bubbles. *Chemical Engineering Science*, 3(1):1–11, 1954.

J. Grace. Shapes and velocities of bubbles rising in infinite liquids. *Trans. Inst. Chem. Eng.*, 51(2):116–120, 1973.

D. Greaves. A quadtree adaptive method for simulating fluid flows with moving interfaces. *Journal of Computational Physics*, 194(1):35–56, 2004.

W. L. Haberman and R. K. Morton. An experimental study of bubbles moving in liquids. *Transactions of the American Society of Civil Engineers*, 121(1):227–250, 1954.

Y. Hallez and D. Legendre. Interaction between two spherical bubbles rising in a viscous liquid. *Journal of Fluid Mechanics*, 673:406–431, 2011.

J. Harper. On bubbles rising in line at large reynolds numbers. *Journal of Fluid Mechanics*, 41(04):751–758, 1970.

J. F. Harper. Bubbles rising in line: why is the first approximation so bad? *Journal of Fluid Mechanics*, 351:289–300, 1997.

R. A. Hartunian and W. Sears. On the instability of small gas bubbles moving uniformly in various liquids. *Journal of Fluid Mechanics*, 3(01):27–47, 1957.

N. Hasan and Z. binti Zakaria. Computational approach for a pair of bubble coalescence process. *International Journal of Heat and Fluid Flow*, 32(3):755–761, 2011.

J. C. Hunt, A. A. Wray, and P. Moin. Eddies, streams, and convergence zones in turbulent flows. *Center for Turbulence Research Report CTR-S88*, pages 193–208, 1988.

M. Ishii and T. Chawla. Local drag laws in dispersed two-phase flow. Technical report, Argonne National Lab., IL (USA), 1979.

H. A. Jakobsen, H. Lindborg, and C. A. Dorao. Modeling of bubble column reactors: progress and limitations. *Industrial & Engineering Chemistry Research*, 44(14):5107–5151, 2005.

Y.-J. Jan. *Computational studies of bubble dynamics*. PhD Thesis,University of Michigan., 1994.

T. Johnson and V. Patel. Flow past a sphere up to a reynolds number of 300. *Journal of Fluid Mechanics*, 378:19–70, 1999.

J. Joshi. Computational flow modelling and design of bubble column reactors. *Chemical Engineering Science*, 56(21):5893–5933, 2001.

J. Katz and C. Meneveau. Wake-induced relative motion of bubbles rising in line. *International Journal of Multiphase Flow*, 22(2):239–258, 1996.

G. Keshavarzi, R. S. Pawell, T. J. Barber, and G. H. Yeoh. Transient analysis of a single rising bubble used for numerical validation for multiphase flow. *Chemical*

Engineering Science, 112:25–34, 2014.

H. Kohno and T. Tanahashi. Numerical analysis of moving interfaces using a level set method coupled with adaptive mesh refinement. *International Journal for Numerical Methods in Fluids*, 45(9):921–944, 2004.

J. Kok. Dynamics of a pair of gas bubbles moving through liquid. i: Theory. *European Journal of Mechanics. B, Fluids*, 12(4):515–540, 1993a.

J. Kok. Dynamics of a pair bubbles moving through liquid. ii: Experiment. *European Journal of echanics. B, Fluids*, 12(4):541–560, 1993b.

J. B. W. Kok. Dynamics of gas bubbles moving through liquid. 1989.

V. Kolář. Vortex identification: New requirements and limitations. *International journal of heat and fluid flow*, 28(4):638–652, 2007.

M. Kubota, S. Akehata, and T. Shirai. The behavior of single air bubbles in liquids of small viscosity. *Kagaku Kogaku*, 31(11):1074–1080, 1967.

A. A. Kulkarni. Lift force on bubbles in a bubble column reactor: experimental analysis. *Chemical Engineering Science*, 63(6):1710–1723, 2008.

V. Kumaran and D. L. Koch. The effect of hydrodynamic interactions on the average properties of a bidisperse suspension of high reynolds number, low weber number bubbles. *Physics of Fluids A: Fluid Dynamics (1989-1993)*, 5(5):1123–1134, 1993a.

V. Kumaran and D. L. Koch. The rate of coalescence in a suspension of high reynolds number, low weber number bubbles. *Physics of Fluids A: Fluid Dynamics (1989-1993)*, 5(5):1135–1140, 1993b.

H. Kusuno and T. Sanada. Experimental investigation of the motion of a pair of bubbles at intermediate reynolds numbers. *Multiphase Science and Technology*, 27(1), 2015a.

H. Kusuno and T. Sanada. Influence of surfactants on the motion of a pair of bubbles

in quiescent liquids. *Japanese Journal of Multiphase Flow*, 29(5):515–522, 2015b.

H. Lamb. *Hydrodynamics*. Cambridge University Press, 1932.

M. Lance and M. L. de Bertodano. Phase distribution phenomena and wall effects in bubbly two-phase flows. *Multiphase science and technology*, 8(1-4), 1994.

Y. Lau, W. Bai, N. Deen, and J. Kuipers. Numerical study of bubble break-up in bubbly flows using a deterministic euler–lagrange framework. *Chemical Engineering Science*, 108:9–22, 2014.

D. Legendre and J. Magnaudet. The lift force on a spherical bubble in a viscous linear shear flow. *Journal of Fluid Mechanics*, 368:81–126, 1998.

D. Legendre, J. Magnaudet, and G. Mougin. Hydrodynamic interactions between two spherical bubbles rising side by side in a viscous liquid. *Journal of Fluid Mechanics*, 497:133–166, 2003.

D. Legendre, R. Zenit, and J. R. Velez-Cordero. On the deformation of gas bubbles in liquids. *Physics of Fluids (1994-present)*, 24(4):043303, 2012.

F. Lehr, M. Millies, and D. Mewes. Bubble-size distributions and flow fields in bubble columns. *AIChE Journal*, 48(11):2426–2443, 2002.

V. G. Levich, S. Technica, et al. *Physicochemical hydrodynamics*, volume 69. Prentice-hall Englewood Cliffs, NJ, 1962.

S. Levy. *Two-phase flow in complex systems*. John Wiley & Sons, 1999.

F. Losasso, R. Fedkiw, and S. Osher. Spatially adaptive techniques for level set methods and incompressible flow. *Computers & Fluids*, 35(10):995–1010, 2006.

K. Lunde and R. J. Perkins. Shape oscillations of rising bubbles. In *Fascination of Fluid Dynamics*, pages 387–408. Springer, 1998.

H. Luo. *Coalescence, breakup and liquid circulation in bubble column reactors*. PhD

thesis, Trondheim, NTH., 1993.

K. Maeda, M. Date, K. Sugiyama, S. Takagi, and Y. Matsumoto. On the motion of a pair of bubbles rising near wall in a vertical channel bubbly flow. *International Conference of Mutiphase sflow (ICMF-2013)*, Proc. 8th, 2013.

J. Magnaudet and I. Eames. The motion of high-reynolds-number bubbles in inhomogeneous flows. *Annual Review of Fluid Mechanics*, 32(1):659–708, 2000.

G. Magnus. Ueber die abweichung der geschosse, und: Ueber eine auffallende erscheinung bei rotirenden körpern. *Annalen der physik*, 164(1):1–29, 1853.

M. Manga and H. Stone. Buoyancy-driven interactions between two deformable viscous drops. *Journal of Fluid Mechanics*, 256:647–683, 1993.

M. Manga and H. Stone. Collective hydrodynamics of deformable drops and bubbles in dilute low reynolds number suspensions. *Journal of Fluid Mechanics*, 300(1):231, 1995.

M. Mathworks. Mathworks, [online]. available: http://. *mathworks.com/help/vision/ug/camera-calibration.html*, 2014.

R. Mei, J. F. Klausner, and C. J. Lawrence. A note on the history force on a spherical bubble at finite reynolds number. *Physics of fluids*, 6(1):418–420, 1994.

D. Meiron. On the stability of gas bubbles rising in an inviscid fluid. *Journal of Fluid Mechanics*, 198:101–114, 1989.

D. Mikaelian, A. Larcy, S. Dehaeck, et al. A new experimental method to analyze the dynamics and the morphology of bubbles in liquids: Application to single ellipsoidal bubbles. *Chemical Engineering Science*, 100:529–538, 2013.

D. Moore. The rise of a gas bubble in a viscous liquid. *Journal of Fluid Mechanics*, 6 (01):113–130, 1959.

D. Moore. The boundary layer on a spherical gas bubble. *Journal of Fluid Mechanics*, 16(02):161–176, 1963.

D. Moore. The velocity of rise of distorted gas bubbles in a liquid of small viscosity. *Journal of Fluid Mechanics*, 23(04):749–766, 1965.

G. Mougin and J. Magnaudet. Path instability of a rising bubble. *Physical review letters*, 88(1):014502, 2001.

F. Odar and W. S. Hamilton. Forces on a sphere accelerating in a viscous fluid. *Journal of Fluid Mechanics*, 18(02):302–314, 1964.

C. Ohl, A. Tijink, and A. Prosperetti. The added mass of an expanding bubble. *Journal of Fluid Mechanics*, 482:271–290, 2003.

N. Otsu. A threshold selection method from gray-level histograms. *Automatica*, 11 (285-296):23–27, 1979.

Y. Pan, M. Dudukovic, and M. Chang. Numerical investigation of gas-driven flow in 2-d bubble columns. *AIChE journal*, 46(3):434–449, 2000.

M. J. Pang and J. J. Wei. Analysis of drag and lift coefficient expressions of bubbly flow system for low to medium reynolds number. *Nuclear Engineering and Design*, 241(6):2204–2213, 2011.

J. Plateau. *Statique expérimentale et théorique des liquides soumis aux seules forces moléculaires*, volume 2. Gauthier-Villars, 1873.

S. Popinet. An accurate adaptive solver for surface-tension-driven interfacial flows. *Journal of Computational Physics*, 228(16):5838–5866, 2009.

M. Pourtousi, J. Sahu, and P. Ganesan. Effect of interfacial forces and turbulence models on predicting flow pattern inside the bubble column. *Chemical Engineering and Processing: Process Intensification*, 75:38–47, 2014.

M. J. Prince and H. W. Blanch. Bubble coalescence and break-up in air-sparged bubble columns. *AIChE Journal*, 36(10):1485–1499, 1990.

L. Rayleigh. On the capillary phenomena of jets. In *Proc. R. Soc. London*, volume 29, pages 71–97, 1879.

P. J. Roache. *Verification and validation in computational science and engineering*. Hermosa Albuquerque, NM, 1998.

M. Ruzicka. On bubbles rising in line. *International Journal of Multiphase Flow*, 26 (7):1141–1181, 2000.

G. Ryskin and L. Leal. Numerical solution of free-boundary problems in fluid mechanics. part 1. The finite-difference technique. *Journal of Fluid Mechanics*, 148:1–17, 1984.

P. Saffman. On the rise of small air bubbles in water. *Journal of Fluid Mechanics*, 1 (03):249–275, 1956.

P. Saffman. The lift on a small sphere in a slow shear flow. *Journal of Fluid Mechanics*, 22(02):385–400, 1965.

T. Sanada, A. Sato, M. Shirota, and M. Watanabe. Motion and coalescence of a pair of bubbles rising side by side. *Chemical Engineering Science*, 64(11):2659–2671, 2009.

F. Savart. Mémoire sur la constitution des veines liquides lancées par des orifices circulaires en mince paroi. *Ann. Chim. Phys*, 53(337):1833, 1833.

L. Schiller and Z. Naumann. A drag coefficient correlation. *Z. Ver. Deutsch. Ing*, 77 (1):318–320, 1935.

E. Schmidt. Ähnlichkeitstheorie der bewegung von flüssigkeitsgasgemischen (similarity theory of motion in fluid-gas mixtures). *Forschungsheft*, 365:1–3, 1934.

V. Sochnikov and S. Efrima. Level set calculations of the evolution of boundaries

on a dynamically adaptive grid. *International Journal for Numerical Methods in Engineering*, 56(13):1913–1929, 2003.

M. Sussman. A parallelized, adaptive algorithm for multiphase flows in general geometries. *Computers & structures*, 83(6):435–444, 2005.

M. Sussman, A. S. Almgren, J. B. Bell, P. Colella, L. H. Howell, and M. L. Welcome. An adaptive level set approach for incompressible two-phase flows. *Journal of Computational Physics*, 148(1):81–124, 1999.

S. Takagi and Y. Matsumoto. Force acting on a spherical bubble rising through a quiescent liquid. *Konsoryu*, 10(3):264–273, 1996.

S. Takagi, T. Uda, Y. Watanabe, and Y. Matsumoto. Behavior of a rising bubble in water with surfactant dissolution (1st report, steady behavior). *Trans. JSME B*, 69: 2192–99, 2003.

A. Theodorakakos and G. Bergeles. Simulation of sharp gas-liquid interface using vof method and adaptive grid local refinement around the interface. *International Journal for Numerical Methods in Fluids*, 45(4):421–439, 2004.

A. Tomiyama. Drag, lift and virtual mass force acting on a single bubble. In *3rd International Symposium on Two-Phase Flow Modelling and Experimentation*, 2004.

A. Tomiyama, I. Zun, A. Sou, and T. Sakaguchi. Numerical analysis of bubble motion with the vof method. *Nuclear Engineering and Design*, 141(1):69–82, 1993.

A. Tomiyama, A. Sou, I. Zun, N. Kanami, and T. Sakaguchi. *Effects of Eotvos number and dimensionless liquid volumetric flux on lateral motion of a bubble in a laminar duct flow.* 1995.

A. Tomiyama, I. Kataoka, Z. Iztok, and T. Sakaguchi. Drag coefficients of single bubbles under normal and micro gravity conditions. *JSME International Journal Series B*

Fluids and Thermal Engineering, 41(2):472–479, 1998.

A. Tomiyama, G. Celata, S. Hosokawa, and S. Yoshida. Terminal velocity of single bubbles in surface tension force dominant regime. *International Journal of Multiphase Flow*, 28(9):1497–1519, 2002a.

A. Tomiyama, H. Tamai, I. Zun, and S. Hosokawa. Transverse migration of single bubbles in simple shear flows. *Chemical Engineering Science*, 57(11):1849–1858, 2002b.

M. K. Tripathi, K. C. Sahu, and R. Govindarajan. Dynamics of an initially spherical bubble rising in quiescent liquid. *Nature communications*, 6, 2015.

J. A. Tsamopoulos and R. A. Brown. Nonlinear oscillations of inviscid drops and bubbles. *Journal of Fluid Mechanics*, 127:519–537, 1983.

H.-K. Tsao and D. L. Koch. Collisions of slightly deformable, high reynolds number bubbles with short-range repulsive forces. *Physics of Fluids*, 6(8):2591–2605, 1994.

H. Tsuge and S. Hibino. The onset conditions of oscillatory motion of single gas bubbles rising in various liquids. *Journal of Chemical Engineering of Japan*, 10(1):66–68, 1977.

T. Tsuge and S. Hibino. The motion of single gas bubbles rising in various liquids. *Kagaku Kogaku*, 35(1):65–71, 1971.

L. Van Wijngaarden. The mean rise velocity of pairwise-interacting bubbles in liquid. *Journal of Fluid Mechanics*, 251:55–78, 1993.

L. Van Wijngaarden. Bubble velocities induced by trailing vortices behind neighbours. *Journal of Fluid Mechanics*, 541:203–230, 2005.

C. Veldhuis, A. Biesheuvel, and L. Van Wijngaarden. Shape oscillations on bubbles rising in clean and in tap water. *Physics of Fluids (1994-present)*, 20(4):040705,

2008.

H. K. Versteeg and W. Malalasekera. *An Introduction to Computational Fluid Dynamics: the finite volume method*. Pearson Education, 2007.

M. Watanabe and T. Sanada. In-line motion of a pair of bubbles in a viscous liquid. *JSME International Journal Series B Fluids and Thermal Engineering*, 49(2):410–418, 2006.

J. Weng, P. Cohen, M. Herniou, et al. Camera calibration with distortion models and accuracy evaluation. *IEEE Transactions on pattern analysis and machine intelligence*, 14(10):965–980, 1992.

J.-Z. Wu, H.-Y. Ma, and M.-D. Zhou. *Vorticity and vortex dynamics*. Springer Science & Business Media, 2007.

M. Wu and M. Gharib. Experimental studies on the shape and path of small air bubbles rising in clean water. *Physics of Fluids*, 14(7):L49–L52, 2002.

Z. Xie, D. Pavlidis, J. R. Percival, J. L. Gomes, C. C. Pain, and O. K. Matar. Adaptive unstructured mesh modelling of multiphase flows. *International Journal of Multiphase Flow*, 67:104–110, 2014.

B. Yang, A. Prosperetti, and S. Takagi. The transient rise of a bubble subject to shape or volume changes. *Physics of Fluids*, 15(9):2640–2648, 2003.

S.-M. Yang and L. Leal. A note on memory-integral contributions to the force on an accelerating spherical drop at low reynolds number. *Physics of Fluids A: Fluid Dynamics*, 3(7):1822–1824, 1991.

H. Yuan and A. Prosperetti. On the in-line motion of two spherical bubbles in a viscous fluid. *Journal of Fluid Mechanics*, 278:325–349, 1994.

X. Zhang and R. H. Davis. The rate of collisions due to brownian or gravitational

motion of small drops. *Journal of Fluid Mechanics*, 230:479–504, 1991.

Z. Zhang. A flexible new technique for camera calibration. *IEEE Transactions on pattern analysis and machine intelligence*, 22(11):1330–1334, 2000.

X. Zheng, J. Lowengrub, A. Anderson, and V. Cristini. Adaptive unstructured volume remeshing–ii: Application to two-and three-dimensional level-set simulations of multiphase flow. *Journal of Computational Physics*, 208(2):626–650, 2005.

I. Zun. The transverse migration of bubbles influenced by walls in vertical bubbly flow. *International Journal of Multiphase Flow*, 6(6):583–588, 1980.

A

UNCERTAINTY ANALYSES

The uncertainty of directly measured quantities is determined by the accuracy of the instrument used. However, the uncertainty of indirectly measured quantities is calculated as a function of the variables that they depend on. For example, if a quantity F is a function of X and Y, then its uncertainty, δ can be written as

$$\delta F = \sqrt{\left(\frac{\delta F}{\delta X}.\delta X\right)^2 + \left(\frac{\delta F}{\delta Y}.\delta Y\right)^2 + ...} \tag{A.1}$$

where δX and δY are the uncertainties of X and Y respectively. In this work the major quantities measured are bubble radius, area and aspect ratio. The distortion effect on bubble shape due the exposure time when a bubble moves with its terminal velocity is also calculated.

The most important parameters used to calculate the uncertainties of measurements are:

- One pixel length = 0.142 mm
- Frame rate = 1/500; time difference between two frames = 0.002 s
- Shutter speed = 1/4000 s
- Maximum bubble rise velocity $\simeq$ 258 mm/s

Uncertainties in the experimental measurements

The error in physical properties due to room temperature variation is less than 0.5% and hence it can be neglected.

The maximum uncertainty in bubble radius due to image resolution:

$\delta_r = \pm 0.071$ mm,

The uncertainty in bubble area, δ_A, due to image uncertainty is:

$\delta_A = \pi \delta_r^2$

For $8.05 < A < 20.75\,\text{mm}^2$, $0.25\% < \delta_A/A < 0.097\%\,\text{mm}^2$

The uncertainty in bubble aspect ratio is negligible since the uncertainty, one pixel length, will appear in the numerator and denominator so that they cancel each other:

$\delta_{Ar} = \frac{\delta_a}{\delta_b}$

The effect of exposure time on the moving bubble, effect of distortion on the bubble shape, is evaluated by:

Bubble rise velocity $\times$ Shutter speed= 258 $\times$ 1/4000= 0.064 mm

The result shows that this factor is too small and hence it is negligible.

B

CFD MODELLING PROCESS

Computational fluid dynamics (CFD) is a computer-based technique in which all systems that involve fluid flow can be analysed and resolved. Recently, CFD has largely been applied in a wide range of industrial applications as it reduces cost compared with the same experimental system (Versteeg and Malalasekera, 2007). According to Versteeg and Malalasekera (2007) solving of a CFD case has to follow three main steps:

Pre-processing: defining a computational domain, generate a grid, selecting the physical models, fluid properties and setting the boundary conditions.

Solver: integrating transport equations, discretising the resulting integral equations to algebraic equations, and solving the algebraic equations iteratively.

Post-processing: interfaces used to visualise the output or the solution such as grid display, scalar and vector scenes, and 2D and 3D plots.

Since the scope of this report is limited, some of elements will be covered below such as mesh generation and finite volume method.

B.1 Grid generation

The computational domain has to be discretised into small cells prior to a numerical solution of the governing equations. This results in generating control volumes inside the computational domain (Blazek, 2001). Generating an adequate grid may take a half of time allocated for numerical simulation (Versteeg and Malalasekera, 2007). The control volumes or the grid cells are different for two dimensional and three domains. In general, triangular or quadrilateral are most used in 2D domain, while tetrahedral, polyhedral, prisms, pyramids or hexahedra are used in 3D flow domain. The grid points have to fully cover the discretised domain. The grid cells are sometimes arranged to fit the boundaries of the computational domain particularly in curved geometries sot that an accurate solution at the boundaries can generated. This type of grids is known as body-fitted grids. In essence, spatial discretisation of Navier-stokes equations by the finite volume method, the finite difference method or the finite element method is basically based on two types of grids (Blazek, 2001; Versteeg and Malalasekera, 2007).

B.1.0.1 Structured grid

In this type, vertices or nodes (grid points) are evenly ordered. This property is the main advantage of this kind of grids as the neighbouring grid points are accessed very easily; i.e., integer value is added or subtracted from the computational indices (i, j, k). Quadrilaterals and hexahedra are frequently used in this type of grid for 2D and 3D, respectively. An example of a structured grid can be

shown in Figure B.1. However, a drawback of the structured grid is that it fails in case of complex geometries (Blazek, 2001).

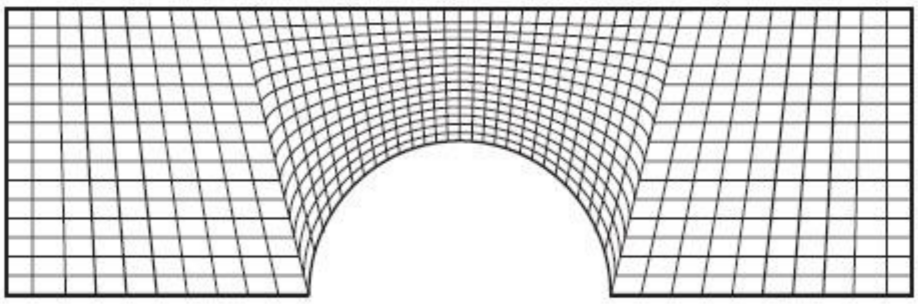


Figure B.1: Structured grid for flow over a cylinder (Versteeg and Malalasekera, 2007).

B.1.1 Unstructured grid

The cell and points of the grid are not arranged in a uniform way. This implies that the distribution of the cell or the grid points is not governed by indices ordering. Thus, a complexity in solving the computational domain is expected. Recently, to resolve the boundary layer in a proper way, tetrahedral and triangular cells are mixed in 2D and a mix of prisms, polyhedra, hexhedra and pyramids is used in case of 3D. This kind of unstructured grid are called hybrid or mixed grids. Figure B.2 shows mixed grids in unstructured mesh (Versteeg and Malalasekera, 2007; Blazek, 2001). Unstructured grids are straightforward for complex geometries so that time is reduced in generating mesh as compared to the same time wasted for meshing and mapping in structured grid. In addition, refinement of regions with large gradients can be easily achievable (Versteeg and Malalasekera, 2007).

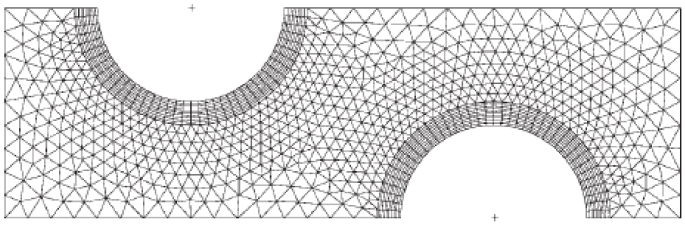


Figure B.2: Mixed cells with unstructured grid (Versteeg and Malalasekera, 2007).

B.2 Finite volume method

The finite volume method (FVM) is a method in which governing equations are discretised. CFD codes frequently uses this method as a primary solving scheme. Unlike other discretisation schemes (finite difference method or finite element method), it allows for the integration of transport equations over small control volumes and therefore in such a case the principle of conservation is applied. In addition, this method can be used in for both structured and unstructured meshes (Blazek, 2001; Versteeg and Malalasekera, 2007). FVM offers two basic approaches in identifying, with respect to the grid, the position of the control volume (ibid).

Cell-centred scheme: In this approach, integrating and storing of the flow quantities are done at the centre of the cell. Then, various methods of interpolations can be applied to approximately compute the flow quantities at the faces of the cells. Numerical stability is affected by the interpolation method chosen (Blazek, 2001).

Cell-vertex scheme: In this approach, mesh nodes are surrounded by the control volume where the governing equations are solved and the variables are stored. Further complexity can be distinguished in this method as cell face are overlapped

and therefore the vertices share the same control volume. Therefore, it is assumed for second-order scheme, instead of computing the flow variables at each point, these variables are constant at each edge of grouped faces. Hence, Evaluation of the flow variables is done at the mid points of those edges depending on both nodes (Blazek, 2001).

B.3 Temporal discretisation

In transient modelling, the solution of Navier-Stokes equations is done for all of the variables over time. The subdivision of time domain into is carried out into a number of small discrete elements. A number of differencing schemes are available to compute the time derivative for a variable ϕ. These schemes are, for example, first-order backward differencing which is given by:

$$\frac{\phi^{n+1} - \phi^n}{\triangle t} = F(\phi), \tag{B.1}$$

another scheme that is second-order backward is given by:

$$\frac{3\phi^{n+1} - 4\phi^n + \phi^{n-1}}{2\triangle t} = F(\phi), \tag{B.2}$$

ϕ^{n+1}, ϕ^n and ϕ^{n-1} are the value at the next, the current, and the previous time step, respectively. Now, $F(\phi)$ can be calculated by applying one of the time integration schemes Explicit or Implicit.

Explicit time integration scheme: For the Explicit scheme, the evaluation of $F(\phi)$ is done depending the known values of ϕ^n at the current time step. For

first-order backward scheme, this can be expressed by:

$$\phi^{n+1} = \phi^n + \triangle t F(\phi^n) \tag{B.3}$$

This scheme has a condition associated with it that is the Courant-Friedrich-Lewy (CFL) number. The selectio of time step $\triangle t$ must be consistent with this condition. For one dimensional problem, CFL is given by

$$\text{CFL} = \frac{u \triangle t}{\triangle x} \leq 1 \tag{B.4}$$

Thus, this impose that the time step must always be small enough to meet the CFL condition in the domain.

Implicit time integration scheme: It is referred to as Implicit because ϕ^{n+1}, at which $F(\phi)$ is estimated, is not explicitly expressed in terms of the current solution, ϕ^n.

This scheme does not require small time stepping and therefore it is unconditionally stable. However, reasonable small time step size is still needed in case of solving the smallest timescales within the flow.

B.4 Vortex identification

A decomposition of a second order velocity gradient tensor, D_{ij}, can be written as:

$$D_{ij} = S_{ij} + \Omega_{ij} \tag{B.5}$$

S_{ij} is shear strain rate tensor, and Ω_{ij} is the vorticity tensor. The characteristic equation of the velocity gradient, $\nabla \mathbf{u}$ is expressed by

$$\lambda^3 + O\lambda^2 + Q\lambda + G = 0 \tag{B.6}$$

where O, Q and G are the three invariant of ∇u. The second invariant, Q or the Q-criterion, which was developed by Hunt et al. (1988), considers the vorticity as "connected fluid region". The Q-criterion is defined as the balance between the strain rate and the vorticity magnitude. Here, we have an area (vortex) at which the vorticity magnitude is greater than strain rate (Kolář, 2007).

$$Q = \frac{1}{2}(\mid \Omega \mid^2 - \mid S \mid^2) \tag{B.7}$$

C

UDF SOURCE CODE

```
/*****************************************************************
    UDF for identifying the region around a bubble for adaption
*****************************************************************/
    #include "udf.h"
    #define FACTOR   0.25 /* How close to the bubble to adapt in */
    #define ZSURF   0.2 /* Location of the water surface */
    #define UDM_MARKER   0 /* Index for UDM used as marker for adaption
*/
    #define UDS_LAPLACE   0 /* Index for UDS for the Laplacian */
    #define DOMAIN_ID_AIR   3 /* ID for the (secondary) air phase */
    #define PHASE_ID_AIR   1 /* Phase ID for the air phase */
    static int lastTimestep = -1 /* Global variable to keep track of the previous
time step number */
    DEFINE_ADJUST(adaptiveRegion, mixDomain)
    {
    #if   !RP_HOST /* Not required by the host */
```



```
    Thread *ctMix, *ctAir;
    cell_t c;
    #endif
    #if  !RP_NODE
    FILE *file;
    #endif
    real udsMax;
    real xCen, yCen, zCen, bVol;
    int currentTimestep = N_TIME;
    /* Only execute the remainder of the function at the first iteration of each
timestep */
    if  ( lastTimestep != currentTimestep )
    {
    lastTimestep = currentTimestep;
    /* Initialise the bubble centre of mass and volume */
    xCen = 0.0;
    yCen = 0.0;
    zCen = 0.0;
    bVol = 0.0;
    #if  !RP_HOST /* Initialise the UDM and calculate the centre of mass of
the bubble */
    thread_loop_c(ctMix, mixDomain)
    { ctAir = THREAD_SUB_THREAD(ctMix, PHASE_ID_AIR);
```

```
begin_c_loop(c,ctMix)
{
real xCentroid[ND_ND];
C_CENTROID(xCentroid,c,ctMix);
C_UDMI(c,ctMix,UDM_MARKER) = 0.0;
if   ( C_VOF(c,ctAir) > 0.1 & & xCentroid[2] < ZSURF )
{ xCen += xCentroid[0]*C_VOF(c,ctAir)*C_VOLUME(c,ctMix);
yCen += xCentroid[1]*C_VOF(c,ctAir)*C_VOLUME(c,ctMix);
zCen += xCentroid[2]*C_VOF(c,ctAir)*C_VOLUME(c,ctMix);
bVol += C_VOF(c,ctAir)*C_VOLUME(c,ctMix);
}
}
end_c_loop(c,ctMix);
}
/* Find the maximum of the UDS */
udsMax = 0.0;
thread_loop_c(ctMix, mixDomain)
{ begin_c_loop(c,ctMix)
{
if ( C_UDSI(c,ctMix,UDS_LAPLACE) > udsMax )
udsMax = C_UDSI(c,ctMix,UDS_LAPLACE);
}
end_c_loop(c,ctMix);
```



```
}
/* Sum the centroids and volume across compute nodes */
xCen = PRF_GRSUM1(xCen);
yCen = PRF_GRSUM1(yCen);
zCen = PRF_GRSUM1(zCen);
bVol = PRF_GRSUM1(bVol);
/* Find the maximum amoung the compute nodes */
udsMax = PRF_GRHIGH1(udsMax);
#endif
/* Pass the summations back to the host */
node_to_host_real_4(xCen,yCen,zCen,bVol);
/* Pass the maximum back to the host */
node_to_host_real_1(udsMax);
#if !RP_NODE /* Normalise the volume weighted centre of mass */
xCen /= bVol; yCen /= bVol; zCen /= bVol;
/* Write the centre of mass and volume to file */
file = fopen("bubble.dat","a");
fprintf(file,"%15.6e%15.6e%15.6e%15.6e%15.6e", CURRENT_TIME, xCen, yCen,
zCen, bVol);
fclose(file);
#endif
#if !RP_HOST /* Set the UDM to 1 wherever the UDS is greater than
FACTOR*udsMax. */
```

```
thread_loop_c(ctMix, mixDomain)
{
begin_c_loop(c,ctMix)
{
if  ( C_UDSI(c,ctMix,UDS_LAPLACE) > FACTOR*udsMax )
C_UDMI(c,ctMix,UDM_MARKER) = 1.0;
}
end_c_loop(c,ctMix);
}
#endif
}
}
DEFINE_SOURCE(udsSource, c, ctMix, dS, eqn) { real source = 0.0;
#if  !RP_HOST /* Get the air domain thread */
Thread *ctAir = THREAD_SUB_THREAD(ctMix, PHASE_ID_AIR);
real xCentroid[ND_ND];
C_CENTROID(xCentroid, c, ctMix);
if ( C_VOF(c,ctAir) > 0.9 && xCentroid[2] < ZSURF ) source = 1.0;
dS[eqn] = 0.0;
#endif
return source;
}
```